Measurement of the Temperature Dependence of the Casimir-Polder Force

by

John Michael Obrecht

B.S., Physics, University of Maryland at College Park, 2001

M.S., Physics, University of Colorado at Boulder, 2005

A thesis submitted to the

Faculty of the Graduate School of the

University of Colorado in partial fulfillment

of the requirements for the degree of

Doctor of Philosophy

Department of Physics

2007

This thesis entitled:
Measurement of the Temperature Dependence of the Casimir-Polder Force
written by John Michael Obrecht
has been approved for the Department of Physics

Eric A. Cornell

Dana Z. Anderson

Date

The final copy of this thesis has been examined by the signatories, and we find that both the content and the form meet acceptable presentation standards of scholarly work in the above mentioned discipline.

Obrecht, John Michael (Ph.D. Physics)

Measurement of the Temperature Dependence of the Casimir-Polder Force

Thesis directed by Dr. Eric A. Cornell

A measurement of the temperature dependence of the Casimir-Polder force is presented along with subsequent measurements of electric fields near surfaces. These measurements were obtained by studying the effects of surface forces on the collective oscillations of a magnetically trapped ^{87}Rb Bose-Einstein condensate (BEC).

In the first part of this thesis, the measurement of the Casimir-Polder force is described. In this experiment, the BEC was placed a few microns from a dielectric substrate and excited into its dipole oscillation. Changes in the collective oscillation frequency resulted from spatial variations in the surface-atom force. The temperature dependence of this force was observed as a threefold increase in its strength as the substrate was heated from 300 K to 600 K, in agreement with theory.

The second part of this thesis deals with measurements that were made of electric fields emanating from surface adsorbates. An alternating external electric field was applied that adds to (or subtracts from) the adsorbate's field in such a way as to resonantly drive the BEC into a mechanical dipole oscillation. The growth rate of the oscillation's amplitude provides information about the magnitude and sign of the adsorbate's field gradient. Using this technique, we were able to reconstruct vectorially the electric field produced by surface contaminants and account for their systematic effects. Lastly, we show that baking the substrate can reduce the electric fields emanating from adsorbates, and that the mechanism for reduction is likely surface diffusion, not desorption.

Acknowledgements

I look at the completion of my Ph.D. thesis not as an end to a five-year odyssey, but as a mere step along an endless, lifelong quest. While it represents the culmination of years of education and ends with an award, I feel that learning doesn't end upon receiving a piece of paper and a square hat; it only ends with death, so far as I know, and Dr. John Obrecht isn't any smarter than Mr. John Obrecht was, he only changed one letter in his name. A suitable goal, I feel, would be to learn some fun fact on the day I die and truly be a lifelong learner. But as far as 'thank-you's go, I ought to take this opportunity to thank those people to whom I owe a great deal in teaching, shaping and inspiring me along the way.

My journey as a scientist started as a young boy, eager to ask questions about our world. I was blessed as a child, not only to be born with a strong capacity to learn, but also to be born into a family so nurturing of an active, young mind. I grew up with the illusion that it was cool to be one of the smarter students in the class– an illusion I've tried hard to promote, sometimes at the expense of a popular reputation. Nonetheless, my parents and my family never let me succumb to peer pressure and even if I wasn't the coolest guy in school, I was always a cool guy at home. That support meant a lot to me through the tough, adolescent years– for that I'm extremely grateful and I extend a tearful 'thank you' to my mother Paulette, my father John, my brother Peter and the rest of my family, all of whom I love and have loved very much.

My passion for Science would never have developed along the way were it not for

a few high school teachers: Mr. Robert Esch, Mr. Bruce Sauders, Mr. Gary Scott and Ms. Louise Shive. I apologize for the fact that recognition for their devotion to high school sciences comes merely in the form of a thesis acknowledgement. Hard work like theirs' should not go unrewarded, but sometimes does. I doubt they know how much they influenced my early life and how much I owe to them for going above and beyond the public-school call of duty– perhaps a knock on a door or flowers on a grave are in order.

In college I grew particularly fond of Physics and my interest in the subject vastly deepened having attended classes taught by Dr. Chris Lobb and Dr. Adil Hassam. There was rarely a class that ended without me hanging around to ask them a few questions. They always gave full, lengthy answers to all of them, and if they couldn't answer a question, they would direct me to someone who would. I often stopped by their offices to ask even more questions or to pick their brains about an upcoming exam. I must have been a bug, but I never felt like one. To them I am very grateful also.

One year is a short time when compared with my education in high school, college or graduate school, yet in one year I learned a great deal about how to become a world-class scientist from the Laser-Cooling and Trapping group at NIST-Gaithersburg. They are terrific scientific role models, for one, but they are all great people also. I was very fortunate to work with their group and many of them remain friends. Thank you for taking a chance on a nervous college graduate.

Working with Eric Cornell in graduate school was a wonderful time for me. I feel very privileged to have had an opportunity to work with such a unique scientist with such interesting approaches to problem solving. I don't know how I would have fared under anyone else's supervision. Eric gave me the scientific freedom to make my own decisions on very difficult problems, from which I believe I have developed a great confidence scientifically. I never felt like someone was holding my hand, and when I needed help and guidance, Eric was never further than a call away or two flights of

stairs. He has a unique way of boiling very complex problems down to very simple pictures, an approach I hope I have slightly inherited from his tutelage. Criticism and scolding never came in the form of a temper, raised voice or harsh tones, but rather through direct, to-the-point conversations. For all that he has done for me, I'm very grateful.

I've also had the pleasure of working very closely with Dave Harber, Rob Wild, Jeff McGuirk and Heather Lewandowski. These four were not only colleagues, but were also very close friends of mine. I often spent several hours a day in their company and would go to lunch with them nearly every day. I would not have done this if I didn't enjoy their company greatly. They all seemed to share my political opinions, sense of humor and my taste in restaurants. Working with them was also a pleasure; I learned a great deal from each of them and the scientific methods they imparted upon me I shall use the rest of my life. I'm very lucky to have worked with such a great bunch over the years.

Additionally, scientific experiments are very rarely the result of a single person's work, but rather they're collaborations that result from numerous discussions and countless suggestions. It may be a single person making decisions on an experiment, but it is greatly shaped by colleagues. Working closely with Debbie Jin, Carl Wieman and the entire tri-group cast often resulted in side-stepping experimental pitfalls and dark scientific alleys. I'm very fortunate to be surrounded with talent like theirs'. Also, I wouldn't have had much of an experiment to work with if it weren't for the extraordinary capabilities that the JILA facility offers. It is nice to work in a temperature-stabilized room, working with state-of-the-art electronics, and brilliantly-crafted experimental structures. A special thanks goes to the JILA staff– if I named one of them I would need to name them all. They *never* turned away a question, even if it meant halting a project they were working on to come to my aid. I've also been lucky to work closely (if electronically) with a group of brilliant Italy-based theorists from the University of Trento: Lev

Pitaevskii, Sandro Stringari and Mauro Antezza.

Last, but certainly not least, I owe to my girlfriend Liz a very special 'thank you' for often being my emotional support through tough times. She frequently reminds me that no matter what the problem is that I face at work, it's never a problem that should truly matter in life. She's the cheerful and exciting yin to my sometimes stressed-out and worrisome yang.

Finally, I would like to *m*ake some personal comments on Life and how I have viewed it these years *a*t JILA. As scientists we often feel proud of our ability *t*o solve complex problems and explain extraordinary *t*hings. We can predict the existence of exotic particles before they *h*ave ever been measured. We can explain complex physical *e*vents billions of lightyears away by manipulating a few equations. We even have theories describing the beginning and the end of the Universe. Ho*w*ever, it's the time between the beginning and the end that we all share together and it's during this time that Physics *f*ails to predict or explain much at all about our l*i*ves. For as beautiful as the Laws of Physics are, we could ne*v*er predict from them an object as b*e*autiful and fragrant as a flower, a process as complex as a heartbeat or feeli*n*gs of love, pain and friendship– I don't think Physics *i*s meant to. It just shows us that there's much more to Life than just Physics; some things we'll *n*ever be able to measure and quantify, and it's these things that really int*e*rest me.

Contents

Chapter

Tables

Table

Figures

Figure

Chapter 1

Introduction

The advent of ultracold technology has made it possible to study atomic interactions for long periods of time. The incredibly low temperatures achieved in such systems have also made it possible to trap atomic ensembles in a relatively small volume of space. Probing such a small collection of atoms in close proximity to bulk objects for long periods of time has led to great advances in the study of atom-surface interactions.

The Casimir-Polder force (the quantum-electrodynamic (QED) interaction between an atom and a surface) has been of particular interest since its prediction sixty years ago [1]. The force, Casimir and Polder theorized, is due to an atom's interaction with enhanced quantum electromagnetic field fluctuations near a surface. The enhancement of field fluctuations comes about from the boundary conditions placed on the field by the surface, and leads to a spatial variation in the field's energy density and hence a net force. This force is dominated by fluctuations of the vacuum field for atom-surface separations larger than wavelengths associated with atomic transitions. However, for larger atom-surface separations (size scales on the order of thermal radiation wavelengths) vacuum-field fluctuations play a much less significant role and thermal fluctuations of the field become the main contribution to the Casimir-Polder force.

Subsequent theories to the Casimir-Polder theory have added corrections to account for both the dielectric properties of the substrate [2, 3] and the presence of thermal radiation [4]. The latter of the two corrections has been of great interest recently with

regards to experimental measurements of the Casimir force (the QED interaction between two electrically-neutral, bulk ob*j*ects) [5]. The thermal correction to the Casimir force in these experiments is small (on the order of 1%), yet is of vital importance as experimental precisions approach those necessary to measure exotic forces beyond the Standard Model [6, 7, 8, 9].

The results described in this thesis shed a great deal of light on such corrections to Casimir-type forces and help us better understand the intricate interplay between light and matter at material interfaces.

1.1 Overview

My vision for the experiment was to continue with and add to the atom-surface interaction measurements that had been made and documented in a previous thesis [10]. The first such experiment we set out to perform was one in which we measured the temperature dependence of the Casimir-Polder force between a rubidium BEC and a fused silica substrate, whose temperature was varied between room temperature (300 K) and 600 K. Our intention was to make measurements which would allow us to differentiate forces that were due to thermal radiation from the substrate from forces that were due to radiation from the surrounding environment. Variability in the temperature of the substrate was critical to this work. By increasing the temperature of the substrate, while keeping the environment temperature relatively unchanged, we were able to see a large increase in the attractive nature of the Casimir-Polder force. This increased attraction was specifically caused by an increase in the thermal near-field radiation from the substrate. These measurements confirmed earlier theoretical predictions by Antezza, *et al*. [11].

A secondary goal of the experiment was to make similar measurements over metal surfaces (as opposed to those measurements that had been made over dielectric materials). This investigation led to a deeper examination of electric fields caused by rubidium

surface adsorbates. Proper accounting of electric field strengths from surface adsorbates was found to be necessary when making precision measurements with atoms near surfaces. Our investigation led to the development of a new technique to map out the vector electric field from the surface adsorbates. In addition, measurements were made confirming our analysis of the systematic effects of electric fields on rubidium atoms. In the end, it was found that measurements made over metal-coated dielectrics are plagued by a number of systematic effects, which are detailed in this thesis.

1.2 Thesis Organization

This thesis is organized as follows. The first chapter of this thesis describes the methods and procedures performed in the experiments discussed in Chapters 3 a*n*d 4, and Appendix A, as well as the improvements to techniques described in the two previous theses which utilized this apparatus [10, 12].

The remainder of the thesis (Chapters 3–4) details the experiments that were performed that focused on the study of atom-surface interactions. Chapter 3 describes the work that was done in which a temperature dependence of the Casimir-Polder force was measured. This experiment was the first measurement of a temperature dependence of any Casimir-type force. The last chapter of this thesis (Chapter 4) details the measurements that were made of electric fields emanating from rubidium surface adsorbates.

Chapter 2

Experiment Methods, Procedures and Improvements

As the third-generation Ph.D. student working on this apparatus, I find it redundant to dedicate a chapter of this thesis to describing the main features and techniques previously discussed in other theses [10, 12]. Instead, I intend to provide a brief overview of the apparatus and to focus more time on describing its upgrades and improvements. In addition, many of the procedures in this thesis are progressions of past procedures and experiments and utilize very similar techniques. In this sense, this chapter details several second-generation improvements to these techniques and procedures, which were necessary for making accurate measurements.

The experiments presented in this thesis which measure temperature-dependent forces are completely unique to this thesis and are therefore discussed in much more detail in subsequent chapters. The techniques, procedures and methods of analysis developed for these experiments are quite new and require a great deal of discussion further along in this chapter.

2.1 Overview of the Apparatus

The apparatus used in this thesis has been described in detail in earlier work [10, 12, 13] and will only briefly be reviewed in this thesis. The apparatus can be divided into two main processes for producing BEC: (1) Producing dense, high-number, ultracold clouds of rubidium in a magneto-optical trap (MOT) and (2) working with magnetically-

trapped atoms in an ultrahigh-vacuum (UHV) region suitable for performing forced rf-evaporation to Bose-Einstein condensation (BEC). Delivery of atoms between these two chambers is done by spin-polarizing the atoms and magnetically transferring them to a separate, ultra-stable magnetic trap. This transfer is done by physically moving two electromagnetic coils, which carry 24 turns of $\sim$ 220 A of current to provide the magnetic trapping fields, a distance of $\sim$ 40 cm to the ultra-stable magnetic trap. The current in the transfer coils is slowly ramped down as the currents in the magnetic trap are slowly ramped up to smoothly transfer the atoms between traps. Once off, the transfer coils are returned back to the MOT region for the next experiment.

The MOT setup is shown schematically in Fig. 2.1. Rubidium gas is dispensed into the (bottle-shaped) MOT chamber via a rubidium dispenser that contains a salt which releases, among other things, rubidium gas when heated. The heat is provided via electrical resistance by running a continuous electrical current ($\sim$ 3.8 A) through the getter. This current remains on 24 hours a day and no ill effects have been seen from its continual use. Getters often require some delicacy in handling, but we have found a very successful recipe for activating and using them over the years. These issues will be discussed in detail in Sec. 2.1.1.

The MOT cooling beams, which provide the trapping forces to the atoms, are created by a two-stage amplification system in which approximately 3 mW of locked laser light is amplified one-hundred fold and directed at the atoms from six orthogonal directions. This laser is locked via standard saturated absorption spectroscopy (SAS) and has a resultant frequency detuned approximately -3Γ of the $F = 2 \rightarrow F' = 3$ transition of the D2 line in ^{87}Rb[1] .

Overlapped with three of the six MOT cooling beams is light referred to as repump light. This light acts to repopulate the $F = 2$ ground state by repumping atoms which have decayed into the $F = 1$ state back to the $F' = 2$ state. Electrons in this state

[1] where Γ is the natural linewidth of the transition ($\sim$6 MHz)

may decay either to the $F = 1$ or the $F = 2$ state with similar probability, closing the cooling transitions and making the MOT possible.

The repump light is then turned off abruptly, followed ∼1 ms later by the MOT cooling light. The delay in shutting off the cooling light acts as an optical pumping scheme which leaves the atoms in the $F = 1$ manifold of the ground state. Atoms which are not specifically in the $|F = 1, m_F = -1\rangle$ hyperfine state are lost at this point due to their lack of trapping ability. The trapped atoms are then transferred to the final magnetic trap for evaporative cooling towards BEC. The stability and reproducibility of the number of atoms produced in a BEC is very dependent upon the MOT cooling and repump beams and will be discussed in great detail in Sec. 2.2.1

Our magnetic trap is referred to as a hybrid Ioffe-Pritchard magnetic trap due to the fact that the trap consists of both permanent magnets and electromagnets. The permanent magnets provide the radial trapping confinement for the atoms ($\sim$ 510 G/cm field gradients in the x and y-directions), while the electromagnets provide both an axial confinement for the atoms ($\sim$50 G/cm^2 in the z-direction) and a bias magnetic field which can be varied between -100 G and 100 G without affecting the trapping frequency in z. Much care is placed in stabilizing the temperature of the permanent magnets, as fluctuations in their temperature directly correlate with fluctuations in the radial trapping frequencies. Care is also taken in stabilizing the currents which pass through the electromagnetic coils, as this also directly affects the radial trapping frequencies. This will be discussed in more detail in Sec. 2.2.2.

The final chamber of the experiment is known as the science cell (shown in Fig. 2.2). This cell is composed of a $40 \times 12 \times 12$ mm^3 pyrex glass cell which connects to the steel vacuum chamber. Inside our science cell sits a monolithic pyrex glass piece which holds four glass substrates in place in order to perform BEC work below (see inset in Fig. 2.17). The materials shown in Fig. 2.2 have since been replaced with other materials since this photo was taken. The magnetic trap surrounds the science

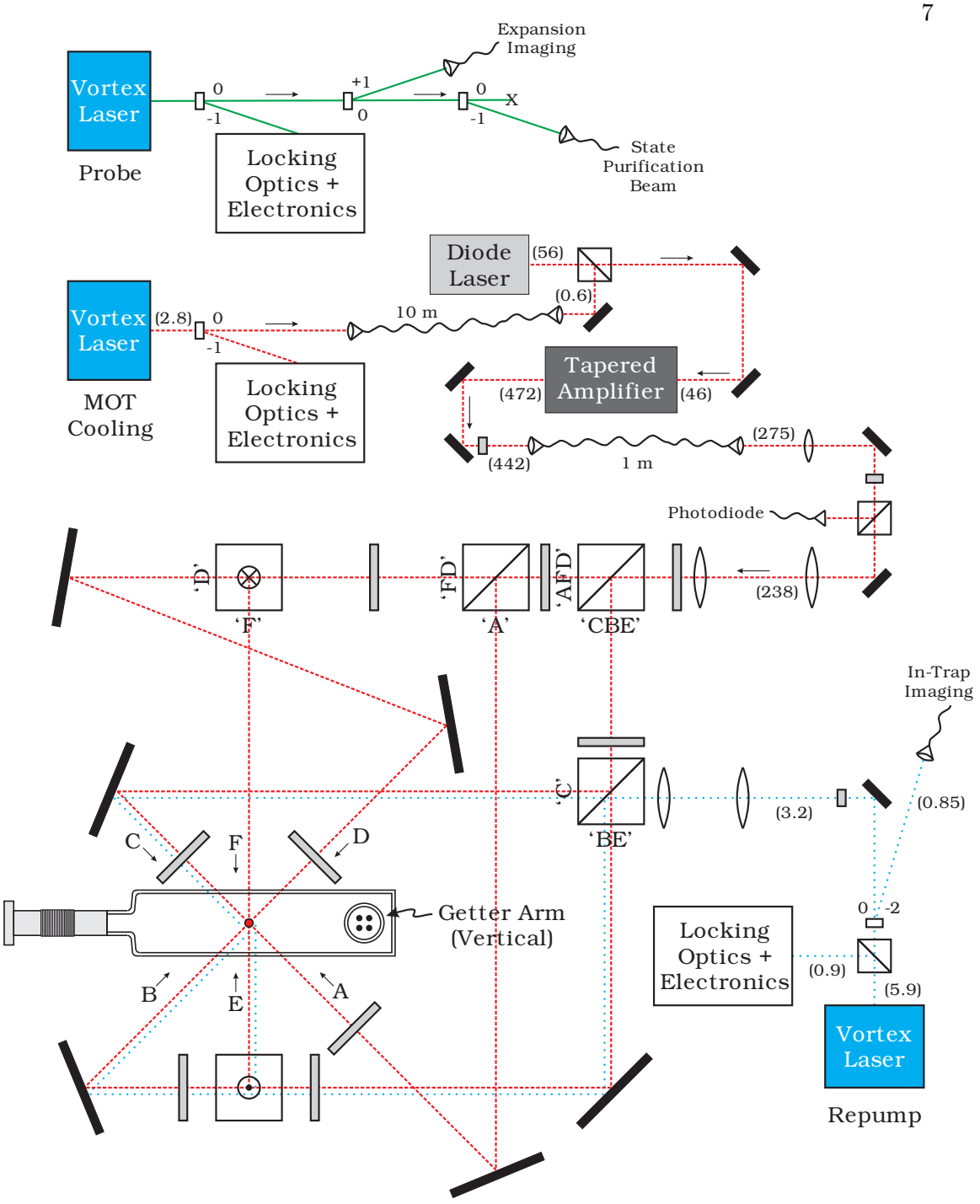

Figure 2.1: The laser and optics setup. Waveplates (gray-filled optics) directly preceding polarizing beam-splitting cubes along the beampath are half-waveplates, designed to rotate linear polarizations. Waveplates directly preceding beam entrance to the MOT chamber are quarter waveplates, which convert the linear polarizations to circular polarizations. The solid green lines correspond to light used in imaging the atoms (probe), the dotted blue lines correspond to repump light, while the dashed red lines correspond to the MOT cooling light. Beams 'E' and 'F' enter the MOT cell along vertical paths, shown schematically as horizontal beams in this diagram. Beam powers are given in parentheses in mW.

cell and is able to be translated from substrate to substrate. The photograph also shows a small rounded piece of glass sitting on the chamber floor. This piece of glass is used as a spacer to keep the holder piece and substrates from moving too close to the end of the chamber.

2.1.1 Rubidium Getter Source

During the high-temperature bake-out procedure (performed to attain UHV conditions) the getters are slightly activated by running a few amps of current through them while the chamber is hot. This prevents the getters from absorbing much contamination. Once the vacuum system has cooled down one can begin to look for rubidium gas in the chamber following getter activation.

The activation of the getters is often the most difficult part in making them work properly and is required due to the fact that a significant number of contaminants must have entered the getter salt during the bake-out procedure. We have found that courage and patience are the key qualities in making a successful activation. By 'activation' we mean a brief increase in the getter current, designed to clean the getter and to get the rubidium emission process going. First, the getter current was increased to $\sim$6 A for several minutes. With such a large current the getter salt is seen to glow brightly from heating and the pressure of vacuum chamber increases from $\sim 10^{-9}$ torr to $\sim 10^{-5}$ torr.

At this point one can begin looking for rubidium in the chamber by one of two methods, each having equal probability of success. First, one can look for an absorption signal of the rubidium by passing a laser beam through the chamber and scanning the frequency of the laser back and forth across an atomic transition to look for the transition lines to appear on an oscilloscope. Second, one can also set up the MOT optics and turn on the magnetic coils to look for a cloud of trapped atoms. The latter was our usual choice for detection because it is easy to see the trapped atoms on a security camera and television screen. It usually takes several days for the background

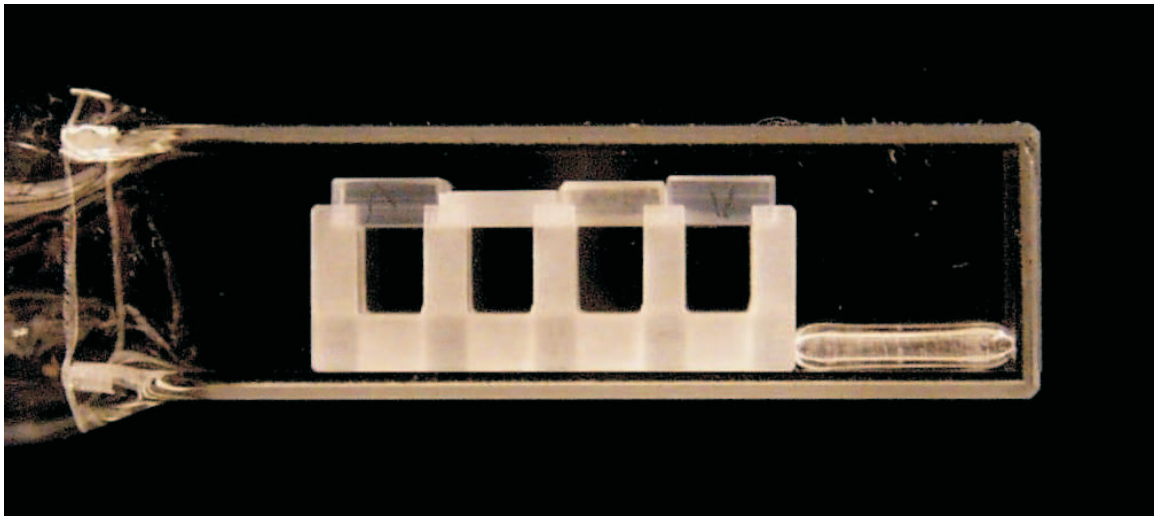

Figure 2.2: Picture of the science cell. Inside the science cell four glass substrates rest on a monolithic pyrex glass piece. The substrates could, for instance, represent four different materials or surface preparations. The BEC may be translated between substrates with little difficulty. The rounded glass piece sitting at the right end of the chamber is a spacer which prevents the holder and substrates from accidentally sliding too close to the chamber wall during chamber assembly.

pressure to settle down to steady-state conditions.

We also found that special care should be taken with the getters when breaking vacuum. We were careful to back-fill the chamber with an inert nitrogen gas rather than atmosphere due to the lack of water in the nearly-pure nitrogen gas. This ensured that the getters were able to be re-activated for further use. In fact, one getter was used for the past three years and survived two separate vacuum breaks and re-activations.

2.1.2 Vacuum Chamber Discussion

The decision to break vacuum with BEC experiments is never easy because it usually requires a great deal of effort to restore the vacuum quality to UHV conditions. Using similar bake-out procedures as before [10, 12] we have been able to produce BEC one week following a vacuum break. The bake-out procedure is difficult and time consuming, but the end result is not quite as risky as once thought.

A thorough investigation of the background pressure in the vacuum chamber was performed using the magnetically-trapped atoms as a probe. The position of the magnetic trap along the axis of the chamber was varied from the center position of the MOT (0 cm) to the middle of the science cell (41 cm). Fig. 2.3 shows data in which the lifetime of the atoms in the magnetic trap was measured, a quantity inversely scaled to the residual local pressure in the chamber. The figure also provides a guide at the top showing the corresponding position along the axis of the vacuum chamber. Collisions due to high background pressures limit the lifetime of the atoms in the magnetic trap (i.e. short lifetimes correspond to relatively high pressures and vice versa).

The data shows a magnetic trap lifetime of $\sim$4 seconds at the position of the MOT (a). The lifetime seems to degrade somewhat as the track position is increased to $\sim$7 cm (b). This position corresponds to the end of the MOT cell and the beginning of the transfer tube. Two 5 mm diameter apertures are placed along the transfer tube, one at (c) and one at (d). These apertures act as conductance limiters between the vacuum

chamber and the ion pumps. The aperture at (c) ensures a relatively high MOT cell pressure (to capture large numbers of rubidium atoms), while the aperture at (d) acts to prevent high pressures of gas from entering the science cell. In essence, one may think of ion pump #1 as pumping solely on the MOT cell, while ion pump #2 pumps entirely on the science cell. One can see from the data that the lifetime in the magnetic trap increases from ∼3 seconds in the MOT cell to nearly 200 seconds near the science cell. This allows us to determine the differential pressure ratio of 200/3 or a factor of nearly 70.

An interesting feature of the data that we will return to in Sec. 2.3.1 is that the trap lifetime abruptly decreases at the junction (e) between the steel chamber walls (gray) and the pyrex chamber walls of the science cell (clear). The decr*e*ase in lifetime, we believe, is due to the fact that the pyrex walls are semi-permeable to small atoms like hydrogen and helium, and even get worse as the pyrex cell walls are heated.

2.2 Improvements to Apparatus Stability and Reproducibility

The precise nature of the temperature-dependent Casimir-Polder force measurement demanded a great deal of stability of experimental parameters for long periods of time (parameters such as magnet temperatures, laser detunings, etc.) and required a high-degree of reproducibility (for such parameters as atom-surface distance, BEC size dimensions, BEC number fraction (N_0/N), oscillation amplitude, etc.). This section of Chapter 2 deals with these necessary improvements and details the procedures and diagnostics that were performed in order to produce a very stable, working experiment.

2.2.1 MOT Stability Issues

A great deal of the shot-to-shot stability and reproducibility of the BEC atom number and BEC size come from the painstaking detail that was placed in the stability and reproducibility of the magneto-optical trap (MOT) and the compressed MOT

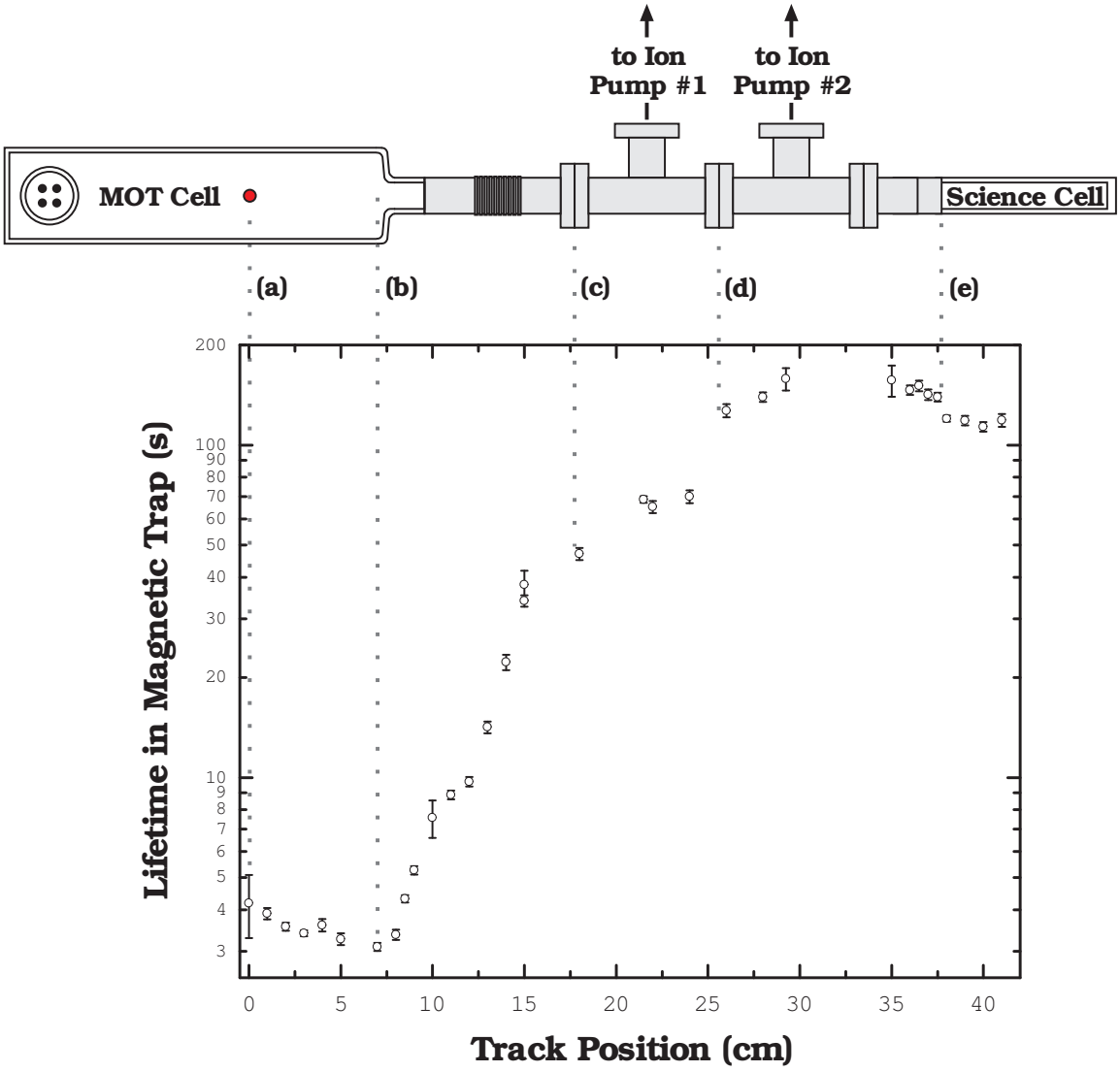

Figure 2.3: Magnetic trap lifetime vs. track distance. Shown in this figure is the lifetime of the atoms in the magnetic trap at various distances along our transfer tube (shown above). The graph is configured such that the x-axis of the graph corresponds to that position along the transfer tube shown in the image directly above. The data shows that the lifetime gets unexpectedly worse from the MOT center (a) to the end of the MOT chamber (b). The data also shows the effect the apertures at (c) and (d) have on the differential pumping ratio. The lifetime gets significantly better past these apertures and reaches a maximum near the second ion pump port. An interesting effect is seen at (e) in which the lifetime is slightly worse within the pyrex science cell. This may be due to the porous nature of the pyrex and is discussed further in Sec. 2.3.2.

(CMOT) conditions. We noticed a direct correlation between the number of atoms condensed in the BEC and the performance of the MOT and CMOT stages. This meant that shot-to-shot reproducibility in the MOT and CMOT parameters were critical in creating a stable BEC to probe atom-surface interactions.

A good diagnostic indicator of an ailing MOT is the time needed to load a given number of atoms into the trap. This load time, we found, is very dependent on a number of experimental factors. First, it depends heavily on the condition of the vacuum chamber, namely the partial pressure of rubidium and also on the partial pressure of all other non-rubidium gases. An ideal MOT chamber would consist of a small enough partial pressure of rubidium to allow for significant MOT lifetimes, but large enough partial pressures to accumulate a significant number of atoms in the MOT. The balance of these two effects, we found, leads to ideal MOT lifetimes (and load times) of 4-5 seconds.[2] If we noticed the load time get significantly long, we would need to adjust either the partial pressure of rubidium, which is set by the current sent through the getter source, or the balance of power in the MOT's trapping beams. It should be noted here that the background lifetime measured in the MOT chamber was a *steep* function of the getter current. Under ideal conditions we found the optimum getter current to be *3*.8 ± 0.1 A. The uncertainty here represents an estimate of the current needed to change the background lifetime by $\sim 25\%$.

The stability in the balance of laser power between the six MOT cooling beams comes from properly and accurately adjusting the polarization of the incoming laser beam. The polarization of this primary beam directly determines how much power is split into each secondary beam path. Fig. 2.1 shows the beam paths for the MOT. The laser light is generated by a commercial external cavity diode laser (ECDL), labelled 'MOT Cooling'. This light is sent through a 10 meter single-mode polarization-

[2] The number of atoms trapped in the MOT rises to a constant background value like (1-e$^{-t/\tau}$). Under ideal conditions, loading 1-$\frac{1}{e}$ of the atoms would result in a loading time exactly equal to the background lifetime.

maintaining (PM) fiber to the main optical table and amplified, first by a high-power diode laser and then by a tapered amplifier. The output of the tapered amplifier is nearly 500 mW of power, linearly polarized and locked to the MOT cooling transition. This light is then sent through a meter-long, single-mode PM fiber, the output of which is split into the six MOT cooling beams. The advantage of using an optical fiber in this setup is twofold: first, the output of the fiber is spatially filtered to be in the TEM_{00} mode. Second, because the fiber output is firmly locked in space, the pointing stability of the beams is much greater and the spatial drift of the MOT is minimized in this sense.

We found the most critical part of the MOT setup, aside from background pressures, was maintaining proper polarization of the laser beam upon output from optical fibers. The optical fibers have an inherent polarization-maintaining axis to them. When the polarization of the tapered amplifier output is aligned with the axis of the fiber, the resultant polarization should have a minimal dependence on temperature fluctuations. However, when the polarization is off-axis, the birefringence of the fiber tends to create a small fraction of elliptically polarized light. This results in an imbalance of power between the six MOT beams, which is highly dependent upon the fiber's temperature and internal stresses. A great deal of care was put into minimizing the effects of stress and temperature.

The way we went about minimizing these effects was to first carefully inspect the fiber for deformities along its length. Deformities in the fiber usually come from improper storage and handling and can be seen as a permanent curvature of the fiber. The fibers in our experiment were all carefully chosen to be short, defect-free fibers and, when secured in large fiber-mounting hardware, let to rest in relaxed positions on thermally insulating foam. The result of this work was that the effects from internal stresses of the fiber were minimized. Minimizing the effects of temperature fluctuations, however, is more difficult.

Fig. 2.1 shows that following the output of the meter-long fiber, the beam polarization is forced to be maximally horizontally polarized by being sent through an adjustable half-wave plate and a polarizing beam-splitter cube. The beam deflected by the polarizing beam splitter cube is vertically polarized and is analyzed with a photodiode. The PM axis of the fiber is then found by heating the fiber and watching fringes appear on the photodiode as the fiber temperature increases. The fringe contrast should be minimized when the laser's polarization is aligned along the PM axis of the fiber.

In addition to finding the PM axis of the fiber, one must also investigate the balance of power between the six MOT cooling beams. One can see from Fig. 2.1 that each of the six MOT cooling beams (labelled A-F) can be traced back along the optical path to several polarizing beam splitter (PBS) cubes and eventually back to the output of the optical fiber. In this sense, we can identify which PBS cube is splitting which beams– for example A, F, and D are split from C, B and E on a single PBS cube (labelled 'AFD' and 'CBE'). By measuring the power incident on the MOT cell from each beam we are able to adjust each respective half-waveplate to make a correct balance of power.

The logical way to make these corrections is by starting at the MOT cell and working one's way backward along the optical path, optimizing each PBS cube encountered. This meant balancing the power 50-50 between beams 'B' and 'E' and then balancing the power $1/3 - 2/3$ between beams 'C' and 'EB'. A similar procedure would be done balancing 'F' and 'D', followed by 'A' and 'FD'. Lastly, the sum power of 'AFD' and 'CBE' should be balanced 50-50 to ensure all beams are of equal intensity when entering the MOT cell. One should also notice that the repump beam (dotted blue line) is only sent to the MOT cell along three of the six beam paths. This is due to the fact that the repump light must only be *present* and need not be *directional*.

The results of the entire optimization process are shown in Fig. 2.4. First, the most notable improvement to the MOT is the condition of the optical molasses phase, in which the atoms are held quasi-trapped solely by optical forces. Graph (a) shows

the ∼2 second time the atoms spend in this phase, while graph (b) shows a small, but discernable, optical molasses being loaded from the background rubidium vapor. Graph (c) shows the shot-to-shot reproducibility of the size of the trapped cloud following a short time-of-flight expansion over a thirty minute time period. The size of the cloud is indicative of its temperature. The closed circles represent data taken before optimization, while the open circles represent data taken after all of the optimization had been done. One can see that the optimization had a beneficial effect on the temperature of the transferred cloud. As a result, the stability of the BEC was found to be much greater also.

2.2.2 Temperature Acquisition and Stability

Due to the sensitive nature of the experiment, a few key experimental parameters were temperature stabilized by standard JILA temperature servo electronic circuits. These parameters were (1) the temperature of the cooling air that continuously blew over the magnetic trap and (2) the permanent magnet temperatures (each independently temperature servoed). The cooling air also served to regulate the temperature of the entire apparatus, due to the fact that it was the only air that entered the enclosing box. This meant that we were able to work with a magnetic trap whose temperature varied by only ~ 0.2 K over the course of a day, and a trap frequency which varied by less than 0.01% in an entire day of data taking (shown in Fig. 2.5). The temperature of the permanent magnets and the magnetic trapping frequency were recorded during the entire data-taking procedure for the data which appears in Ref. [14]. Data points connected by solid black lines correspond to data taken in a single day.

The atom-surface distance (discussed in greater detail in Chapter 3) may very well be the most critical parameter of an experiment which directly deals with atom-surface interactions. Many interactions have power-law spatial dependencies which makes the stability and reproducibility of the atom-surface distance extremely critical. What com-

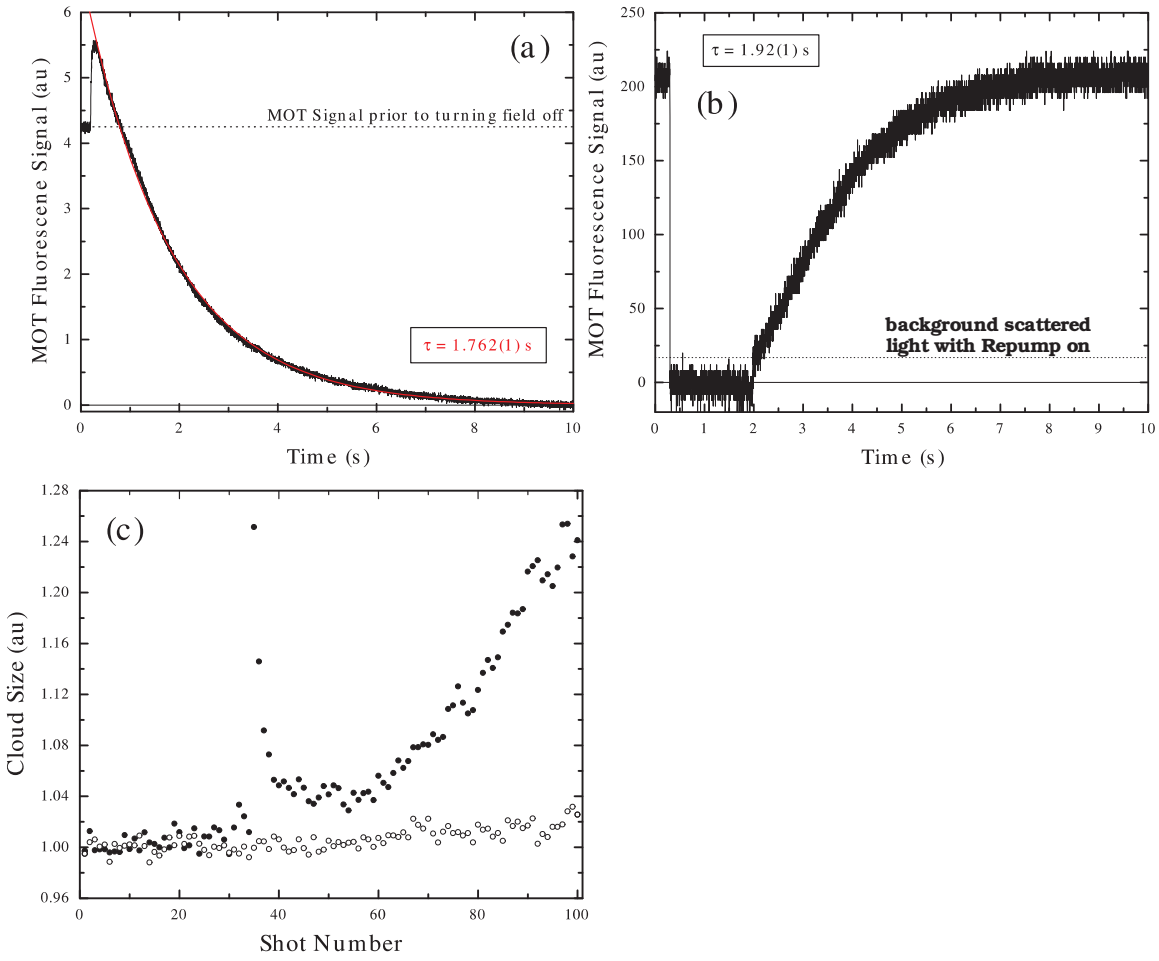

Figure 2.4: MOT stability issues. The data in (a) and (b) are photodiode currents which measure the fluorescence of atoms from a MOT. Both graphs show data taken after a significant amount of work was done to create a healthy, power-balanced MOT (discussed in Sec. 2.2.1). The data in (a) shows the MOT fluorescence after the magnetic field was turned off. The long lifetime of the signal indicates a very good optical molasses, in which the atoms remain semi-trapped due purely to optical forces. *D*ata in (b) show a weak, but discernable, loading of an optical molasses in which no magnetic-trapping fields were present. Graph (c) shows the measured size of a cloud of atoms following the CMOT stage and a short time-of-flight expansion. Here the cloud size is proportional to the square root of the temperature of the atoms in the magnetic trap. This data demonstrates the typical behavior of an ailing MOT immediately before stabilizing conditions (closed circles) versus data taken after stabilizing (open circles). It takes about one minute to take four shots.

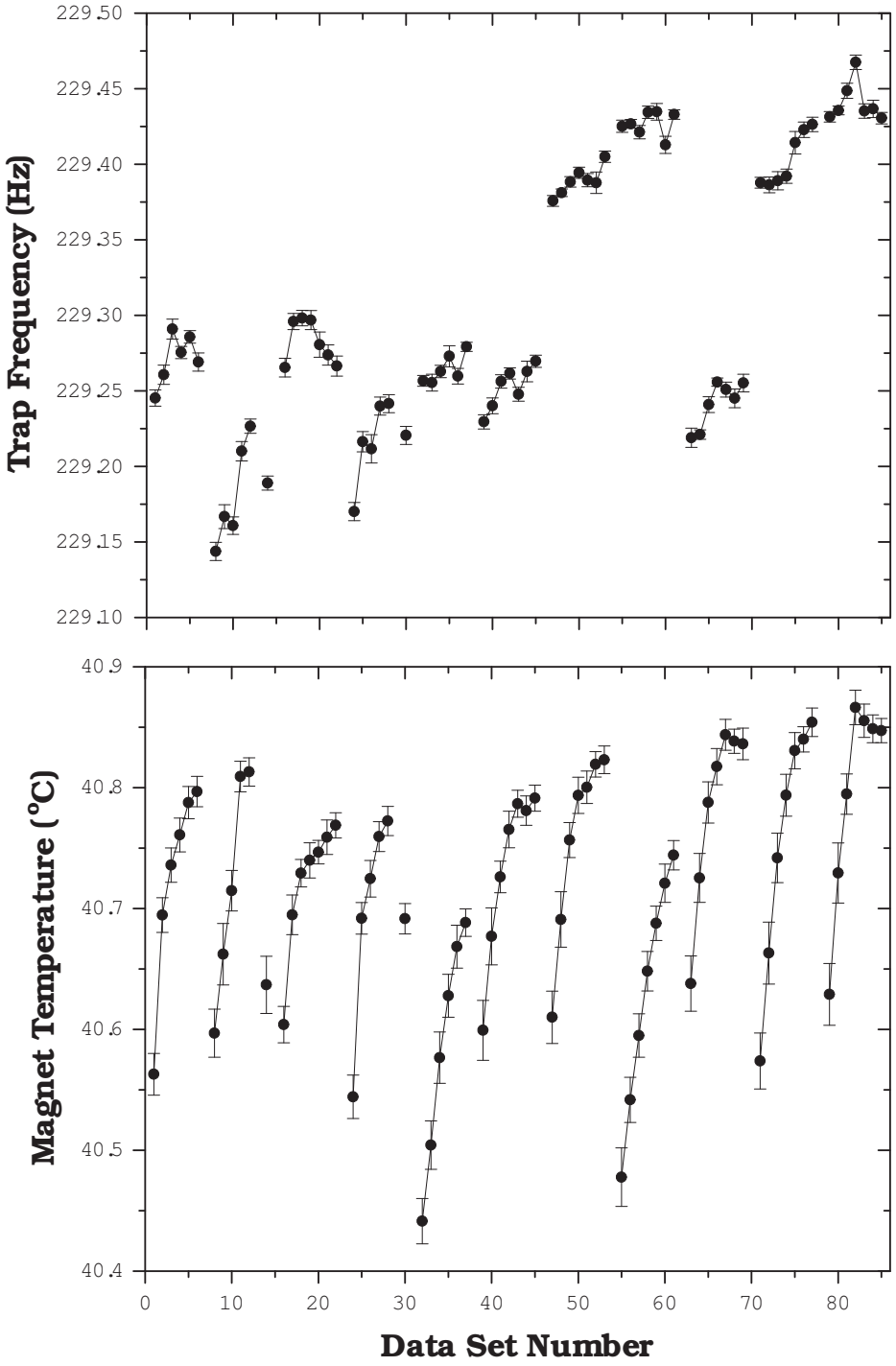

Figure 2.5: Stability of the magnetic trap. This figure shows data demonstrating the stability of our magnetic trap during ideal operating conditions. The data shown in (a) corresponds to the normalizing trap frequency $\omega_o/2\pi$ which appears in [14]. This data spans several weeks and illustrates the reproducibility and stability of our magnetic-trap conditions. The data in (b) shows the measured temperature of our permanent magnets over the same time period. The magnets heat by less than 0.3^oC in an entire day and are much more stable over a one-hour data set (the mean error bar for one set is equal to 16 mK). Data points connected by solid black lines correspond to data taken in a single day.

plicates this is the fact that the substrate position and the BEC position are independent of one another; one is determined mainly by the box temperature (the substrate is held in place by the vacuum chamber, which is held firmly by aluminum mounting blocks), while the other is determined by the magnet temperature (the BEC's equilibrium position is determined by the strength of the magnets, which varies with temperature, and current servos, which do not have much variation in temperature). Fig. 2.6 shows the relative position of the substrate's surface during a typical day of data taking. By stabilizing the box temperature and the magnet temperatures we are able to limit the drift of the surface position to less than 3 microns over the course of a day. Most of this drift is due to the warmup of the apparatus, and settles to less than a micron drift during actual data taking. Because of the level of control in our experiment, we are able to accurately determine the atom-surface distance to less than 150 nm typically, which is reflected in the error bars in Fig. 2.6.

We also found it was necessary to have a great deal of stability of the room temperature of the laboratory. The room air is controlled by pneumatically regulating the flow of hot and cold air into the room. The electronics which control various aspects of the experiment are often large and powerful enough to be considered 'heat generators' as well. In order to achieve an equilibrium room temperature by the start of the working day, most of the heat generating equipment was turned on by a timer in the early hours of the morning. Fig. 2.7 shows the measured room temperature over the course of a data-taking day for four different days over the course of one month (The data is purposely offset by 1^{o}C between sets). This data highlights the stability of the room temperature over the course of a day and also illustrates the day-to-day reproducibility. The roughness in the daytime data is due to the presence of rf-interference in the thermometer circuitry and does not reflect real temperature variations.

The temperatures of various elements around the room and in the experiment were measured continuously daily, recorded with data acquisition (DAQ) hardware and saved

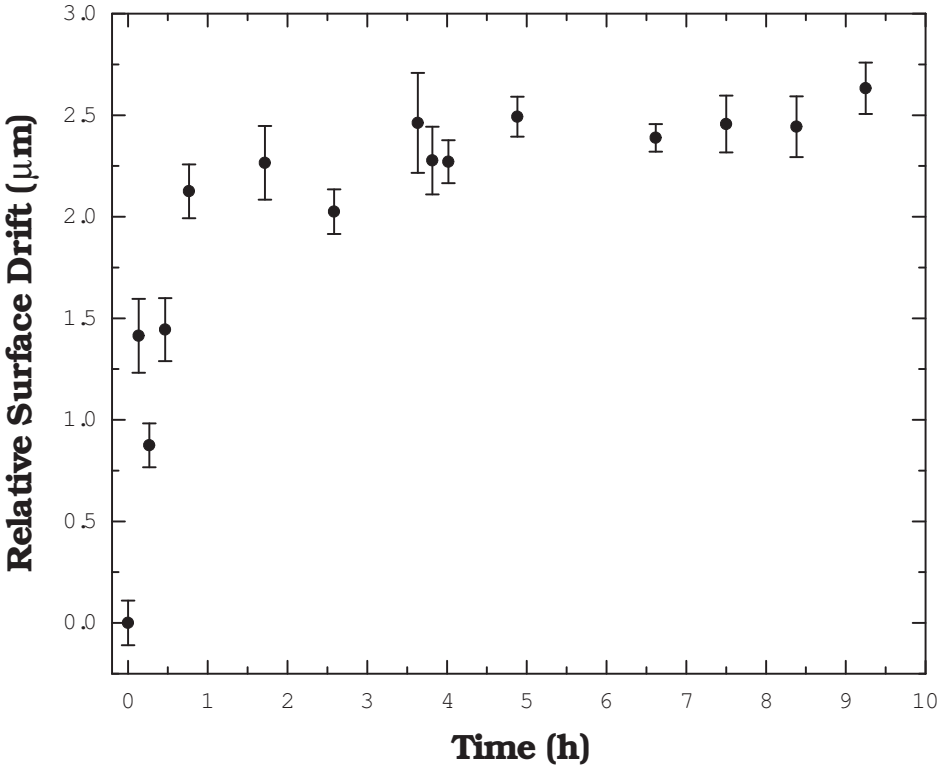

Figure 2.6: Stability of the surface position. This figure shows measurements of the relative position of the fused silica surface (relative to the CCD camera) over the course of a day (∼10 hours). Following a one-hour warm-up period, the surface drift is less than ∼ 50 nm/hr over several hours (the error bar, representing the standard deviation about the mean, is equal to ∼140 nm).

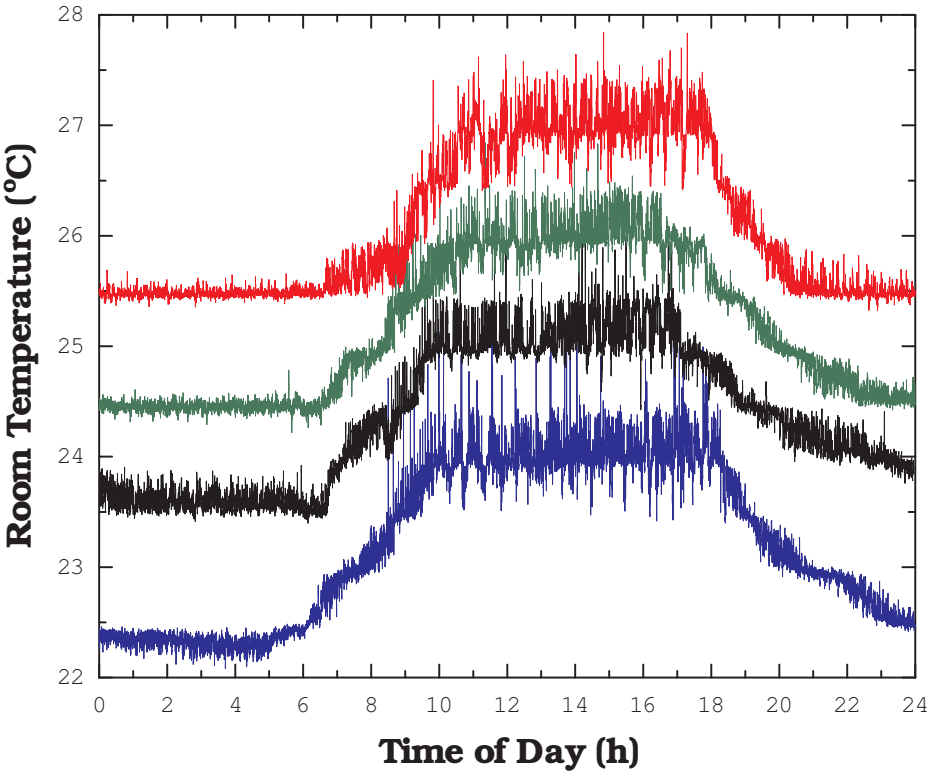

Figure 2.7: Room temperature stability. This figure shows the temperature of our laboratory over the course of the day. Electronics in the room were either left on continuously or were turned on with a timer (set to 6 AM). During data taking operations the room temperature did not vary by more than 1^oC. The scatter in the data between 9 AM and 6 PM is due to interference from rf radiation in the room and does not represent real temperature fluctuations. The data sets are offset 1^oC from one another to illustrate the room-temperature reproducibility.

into a computer. The temperature measurements were made using K-type thermocouple junctions, which were fed into a custom electronic circuit to produce a signal with a 10 mV/^{o}C calibration, shown in Fig. 2.8. The data acquisition was done with a National Instruments DAQ board (NI-6025E), which could take as many as 16 analog input channels, and data was analyzed using *LabView* software. We found, in the course of acquiring temperature measurements, a certain level of 'cross-talk' between analog input channels on this board, which we eliminated by placing a 10 kΩ resistor between in the input channel and ground. Fig. 2.8 shows a schematic diagram of the temperature acquisition hardware for two temperature inputs, which can be scaled up to incorporate 16 input channels, if needed.

2.2.3 Adiabatic Rapid Passage in a Large Magnetic Field

In order to perform expansion imaging on the atoms in the presence of a permanent magnetic field, we found it necessary to perform an adiabatic rapid passage (ARP) of the atoms into an anti-trapped state and image the atoms in a high magnetic field (bias field of $\sim$ 90G) after approximately 3 ms of anti-trapped expansion. This was done by applying fixed microwave frequency radiation ($\nu = 6653.5$ MHz) to the atoms, jumping the bias field very rapidly to a given magnetic field B_i and ramping the field through the $|F = 1, m_F = -1\rangle \rightarrow |2, -2\rangle$ transition to the final magnetic field B_f.

In order to find the exact center of the resonance, data was taken in which the magnitude of the magnetic field was varied while a number of variables were recorded– variables such as the radial position and width of the expanded BEC, and the number of ARPed atoms. The magnitude of the magnetic field was varied in this experiment, as opposed to varying the frequency of the microwave radiation, for ease in data taking. Let us define ΔB as the width of the magnetic field ramp and B_c as the ramp center,

$$\Delta B = B_f - B_i \tag{2.1}$$

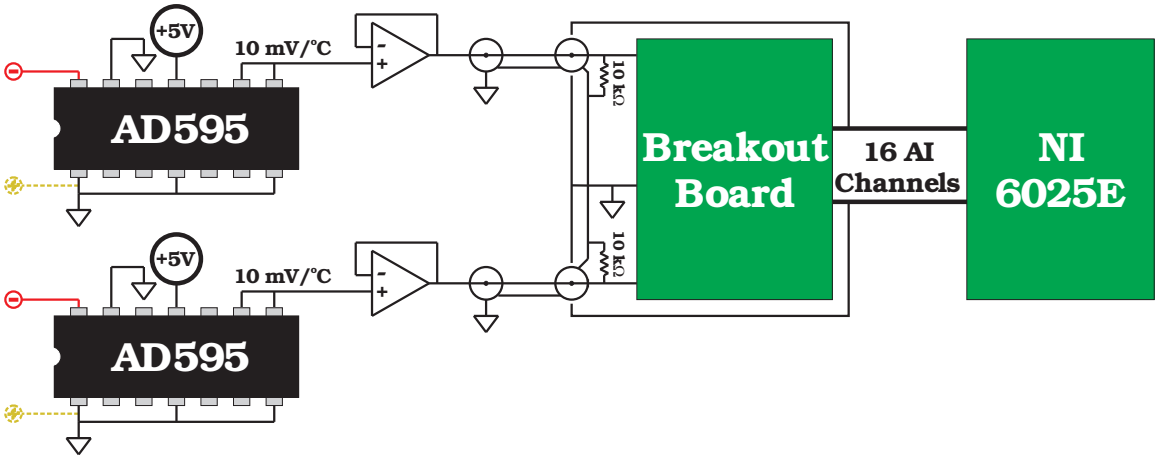

Figure 2.8: Temperature acquisition circuitry. Schematic diagram showing the electronics and computer acquisition used to record various temperatures over the course of a day. The plus and minus (yellow and red) leads represent the connections to a K-type thermocouple junction. 10 kΩ resistors are placed between the input voltage and the chassis ground surrounding the breakout board in order to avoid cross-talk between input channels. Only two of a possible sixteen input channels are shown.

$$B_c = (B_f + B_i)/2. \tag{2.2}$$

An important detail of the ARPing process is that the equilibrium position of the BEC is dependent upon the spring constant (or trapping frequency) of the magnetic trap, due to the presence of gravity. As the magnitude of the magnetic field is increased, the spring constant is lessened and the equilibrium position of the BEC is shifted down in space, farther from the substrate's surface. Therefore the BEC will gain an initial velocity following the rapid jump of the bias field to B_i.

Fig. 2.9(a)-(c) shows data taken scanning the magnetic field B_c with a fixed ramp width $\Delta B = 1.1$ G. Fig. 2.9(a) shows the final position of the BEC cloud following a 3 ms ARP sequence and subsequent 2.5 ms expansion. By carefully analyzing the exact final position of the ARPed atoms, we can determine exactly how the atoms have been ARPed. The data shows a clear sign of an ARP resonance. Atoms that have been ARPed late in the process (configuration (1) for example) show up as having travelled the least amount of distance, whereas atoms that have been ARPed very early in the process ((7) for example) appear to fall much farther. The variation in the final position of the BEC indicates exactly when in the sequence the atoms have been ARPed (if at all) and allows us to reconstruct the ARPing process.

The solid line in (a) represents results from a zero-parameter simulation of the process, which shows seven unique features, corresponding to the seven diagrams in Fig. 2.9.

Because the microwave coupling is fixed in frequency, we may think of the ARP transition as being a large elliptical shell enclosing the BEC which converges upon the magnetic field minimum as the magnetic field is being ramped up. The presence of gravity ensures that the bottom surface of the ARP 'shell' will reach the atoms before the top surface does. Therefore, this shell is represented by a solid black line in Fig. 2.9 and the ramping area is indicated by the gray fill. If the atoms cross the shell, either

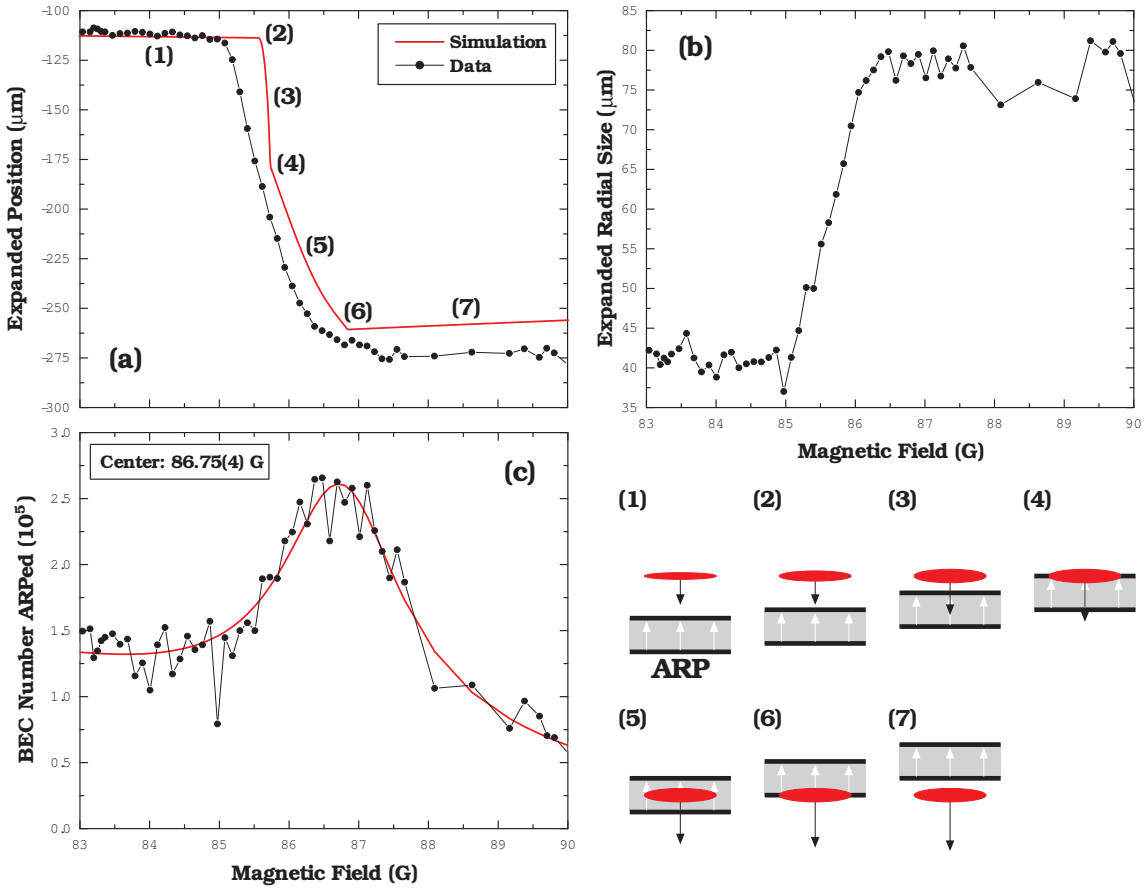

Figure 2.9: ARP data. The data in (a) shows the position of atoms following a 3 ms ARP sequence and subsequent time-of-flight expansion. The atoms obtain an initial downward velocity, indicated by the arrows in the illustration, following a magnetic field 'jump'. The various features in the graph are illustrated on the bottom right with the heavy black lines representing the beginning and end of the ARP resonance. The zero-parameter simulation (solid red line) shows good agreement with the data and allows us to identify the various features (described in Table 2.2.3). Graph (b) shows the expanded radial size of the BEC. BECs that have been ARPed have a much larger radial size than BECs that have not. The data in (c) shows the number of atoms that have been ARPed as a function of the center magnetic field. The solid red line shows a fit of this data to a Lorentzian profile. The peak number of ARPed atoms corresponds to the center magnetic-field configuration (5) in the simulation.

through field ramping or by falling, they will be transferred to the anti-trapped $|2,-2\rangle$ state, fly away rapidly and be destructively imaged.

The timing of the ARP sequence is very sensitive. Performing an ARP ramp too early or too late results in a poor transfer of atoms to the anti-trapped state. Table 2.2.3 outlines 7 various ARP transitions that may be performed, corresponding to (1)-(7) in Fig. 2.9, which depend on the timing of the ARP sequence. The simulation qualitatively agrees very well with the data, where discrepancies can be due to the fact that the simulation has the capability to switch magnetic fields infinitely fast, while in practice the magnetic-field switching time is limited by inductance and servo bandwidths. Other discrepancies may simply come from magnetic-field calibration errors. One can see from the diagram the various ARPing features. The ideal ARP would correspond to number (5), in which the resonant magnetic field is jumped to just below where the atoms are in space and slowly ramped up through resonance as the atoms fall down. This would provide a very controlled method in which the ramping parameters could be adjusted to maximize the number of ARPed atoms, rather than simply have the atoms fall uncontrollably through resonance (3), or have resonance race past them (7). A rapidly passing resonance does not fulfill the ARPing requirement that the time rate of change of the resonance be smaller than the square of the Rabi frequency.[3] .

We can verify that indeed the ARP center is configuration (5), first by analyzing the modelling program, and also by looking at the number of BEC atoms which are ARPed and imaged, shown in Fig. 2.9(c). The center of a Lorentzian fit directly corresponds to the ARP center, configuration (5) of the data (which lies below configuration (6) of the model). Additionally, one would expect a BEC cloud that has been properly ARPed into the anti-trapped state to have a radial width much larger than a BEC cloud that has not. This is demonstrated in (b), in which atoms that are not fully ARPed ($B_c < 85$ G) never quite expand as much radially.

[3] By varying the parameters of the ARP, we estimate the bare Rabi frequency to be $\sim$2 kHz

Feature	B_c G	Comment	$\sim \Omega_{min}/2\pi$ Hz
(1)	84.00	never fully reaches resonance	n/a
(2)	85.55	just reaches resonance by falling	500
(3)	85.68	ARPs through resonance by falling	300
(4)	85.74	just misses ARP ramp	250
(5)	86.20	ARP ramp centered on BEC	800
(6)	86.85	field jumps to resonance	>10000
(7)	88.00	resonance races by too quickly	>10000

Table 2.1: Distinct ARP features. This table provides a description of the various ARP transitions shown in Fig. 2.9. Here Ω_{min} represents an estimate of the minimum Rabi frequency needed for the ARP procedure to work properly. Features (6) and (7) correspond to the ARP resonance speeding through the BEC. A very large Rabi frequency would be needed for this process to be truly adiabatic.

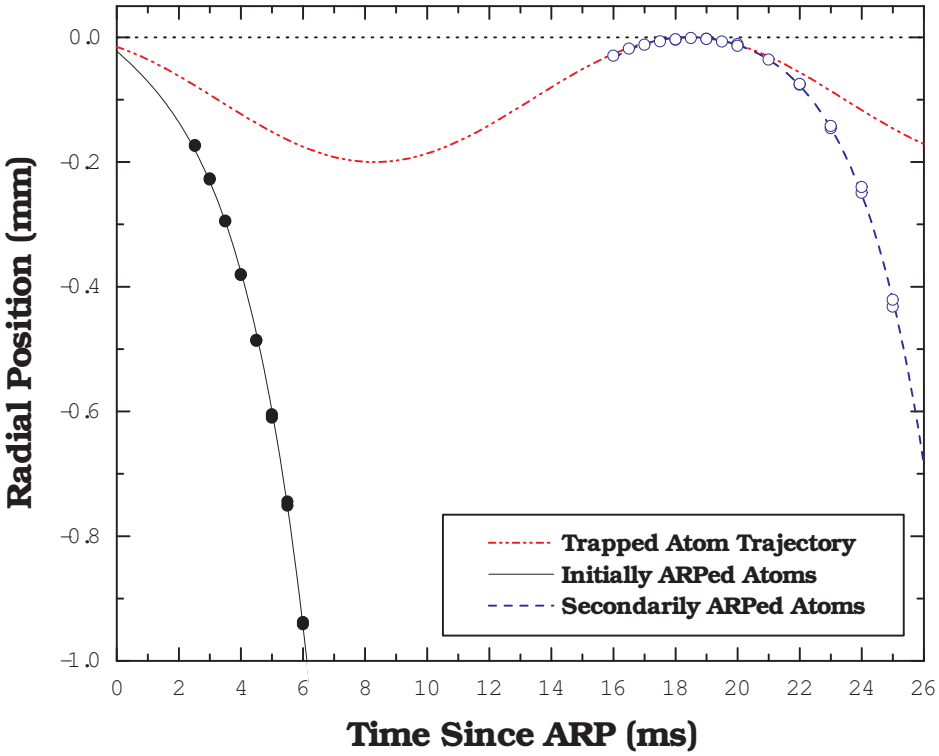

Figure 2.10: Testing ARP efficiency. The ARPing procedure begins by rapidly increasing the bias magnetic field. This has the effect of shifting the equilibrium position of the atoms down from the dotted black line (y=0) to a position ∼0.1 mm lower. Atoms are ramped through an ARP resonance and fly rapidly away (solid black line) from the equilibrium position. Atoms which have not been ARPed properly remain trapped and oscillate down and back along the dash-dotted red line. Upon returning the atoms will once again see the ARP resonance and fly rapidly away from the equilibrium position (dashed blue line). By measuring the number of atoms which have and have not been ARPed, one may estimate the efficiency of the ARPing procedure.

We performed an additional measurement to test the ARP efficiency (N_{ARPed}/N_{Total}). In this experiment we allowed the ARP to remain on as usual, while atoms which were not ARPed passed by the equilibrium position (modified by the presence of the larger magnetic field B_f), came to a stop at the classical turning point, and returned back towards the ARP 'shell'. A similar fraction of these atoms are then ARPed upon this return trip. These atoms, in the trapped $|1,-1\rangle$ state, oscillate with a very well known frequency, and return after roughly one trap period. Fig. 2.10 shows data for atoms that are initially ARPed and fall in anti-trapped expansion (solid black line). Atoms which are not initially ARPed oscillate along the trapped trajectory[4] (dash-dotted red line), are ARPed upon returning to resonance and also fall in anti-trapped expansion (dashed blue line). By counting the number of atoms which have returned and are secondarily ARPed, we can estimate the efficiency of a single pass through the ARP. We found our microwave-loop antennas to provide an ARP efficiency between 80-95%, while a microwave waveguide provides nearly 100% efficiency.

Fig. 2.11 shows an image of the two microwave sou*r*ces used in the course of the experiments, relative to the science cell (substrates not pictured). The loop antenna was designed to be forward-broadcasting by attaching a ground plane (copper backplate) to restrict radiation in the backward direction. A hole is cut in the center of the back plane which is designed to provide access for imaging (red horizontal beam). The hole is much smaller than the wavelength of the microwave radiation (λ= 4.5 cm) and therefore does not pose a problem with back-directed radiation. Also pictured in Fig. 2.11 is a rectangular microwave waveguide, which provides the best source of microwave radiation. However, the positioning of the waveguide restricts optical access down the axis of the science cell. Images taken along this axis provide information about the x and y-position of the BEC, which is needed when performing systematic

[4] Note: the equilibrium position of atoms following the trapped trajectory is roughly 100 μm lower than that of atoms trapped prior to the ARP sequence, whose equilibrium position is zero.

tests. For these experiments (detailed in Chapter 4) the waveguide is removed and the loop antenna provides the sole source of microwave radiation to the atoms.

2.2.4 Imaging in a Large Magnetic Field Gradient

Once the atoms have been ARPed into the $|2,-2\rangle$ state and have fallen in anti-trapped expansion, they are destructively imaged onto a CCD camera with a 20 μs pulse of collimated probe laser light, resonant with the $F = 2 \rightarrow \ F' = 3$ cycling transition. This transition is sensitive to magnetic fields ($d\nu/dB \ \simeq 1.4$ MHz/G) and the transition frequency must be found and optimized with an AOM. Fig. 2.12(a) shows the peak optical depth of the imaged atoms plotted versus the relative detuning of the transition. The open (blue) circles represent data taken with a BEC, whose peak optical density is large when compared with that of a non-condensed thermal cloud (closed black circles). Analysis of the fits to the data in (a) shows a larger width of the transition for the thermal cloud due to the fact that the thermal cloud is spatially larger than a BEC. When imaged in a magnetic field gradient ($\sim$510 G/cm), the transition will naturally be detuned due to the field sensitivity (the Zeeman effect) of the transition. The width of these two transitions agrees well with calculations of the transition widths in the presence of a field gradient.

The detuning referred to in Fig. 2.12 is relative to the resonance of the atomic transition in a $\sim$ 90 G magnetic field, which is shifted $\sim$130 MHz from the zero-field resonance. By locking the -1 order of the first AOM in the probe laser path (see Fig. 2.1) to the $F = 2 \rightarrow F' = 2 - 3$ crossover, the zero-order beam is effectively detuned from the crossover transition by the AOM frequency ($\Delta\nu \approx 275$ MHz). This beam then passes through another AOM which has the effect of detuning its $+1$ order back to the crossover transition. What makes this up-and-down setup nice is that the second AOM frequency can be varied very carefully in order to find the resonance. The laser frequency is detuned from the $2 \rightarrow 3'$ transition by almost the exact amount the

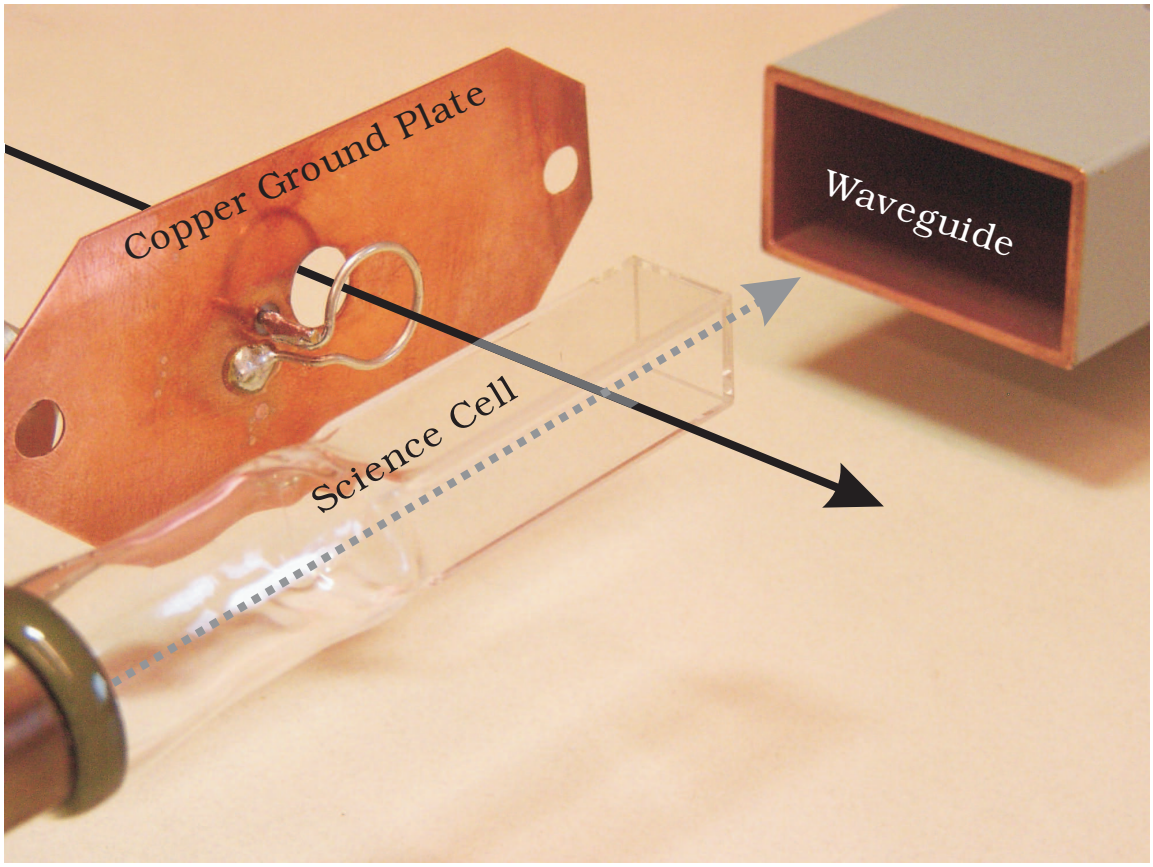

Figure 2.11: Microwave loop antenna. Photograph of the loop antenna used to broadcast microwave radiation to the atoms in the science cell (table and substrates not shown). The antenna uses a copper ground plate to direct the radiation towards the atoms, rather than to broadcast in all directions. The hole in the center of the copper plate provides optical access to the atoms in order to image them (solid black arrow). Shown also is the microwave waveguide which provides very powerful, direct radiation to the atoms. The waveguide, however, prevents us from imaging the atoms along the axis of the science cell (dashed gray arrow). The diameter of the loop is ∼12 mm. For most measurements, the waveguide was removed.

atoms are detuned by the magnetic field. The result is that the atoms see the laser light as being on resonance with the $2 \rightarrow 3'$ transition.

In addition to observing the detuning effects when imaging in a strong magnetic-field gradient, we also observed an apparent shift of the center-of-mass of the clouds. Fig. 2.12(b) shows the center position of both the BEC (open blue circles) and thermal cloud (closed black circles) shift with the laser detuning. This is an artifact of imaging in a field gradient. When the laser frequency is detuned to the red (blue) side of the transition, atoms in a slightly larger (smaller) magnetic field will be resonant with the transition and will appear to have a greater density than the atoms in the center of the cloud. The lines in (b) are single-parameter fits of the data to the derivative of the Lorentzian fit-function in (a), where the width and center of the transitions are fixed, varying only the amplitude of the apparent center-position movement.

A good analogy of this effect is to picture the imaging laser as a spotlight. Detuning the laser moves the spotlight in space, such that resonance occurs when the spotlight is centered on the atoms. The spatial extent of the spotlight in a magnetic-field gradient is analogous to the atomic linewidth. If the cloud covers a magnetic field gradient large enough (like the thermal cloud), the spotlight only shines on a fraction of the atoms and the apparent center of the cloud shifts greatly. However, if the cloud is very small spatially (like the BEC), the apparent shift of the center is also small.

2.2.5 Ground State Purification of BEC

In our experiment we desire the entire BEC population to be in the $|1, -1\rangle$ state. However, it sometimes happens that atoms can be trapped in multiple states, like for instance the $|2, 1\rangle$ and $|2, 2\rangle$ states (perhaps due to a faulty optical pumping scheme during the CMOT process). We occasionally found the conditions right (or wrong, depending on your point of view) to accidentally condense atoms in more than one state. This was problematic to our experiment due to the fact that these impurities

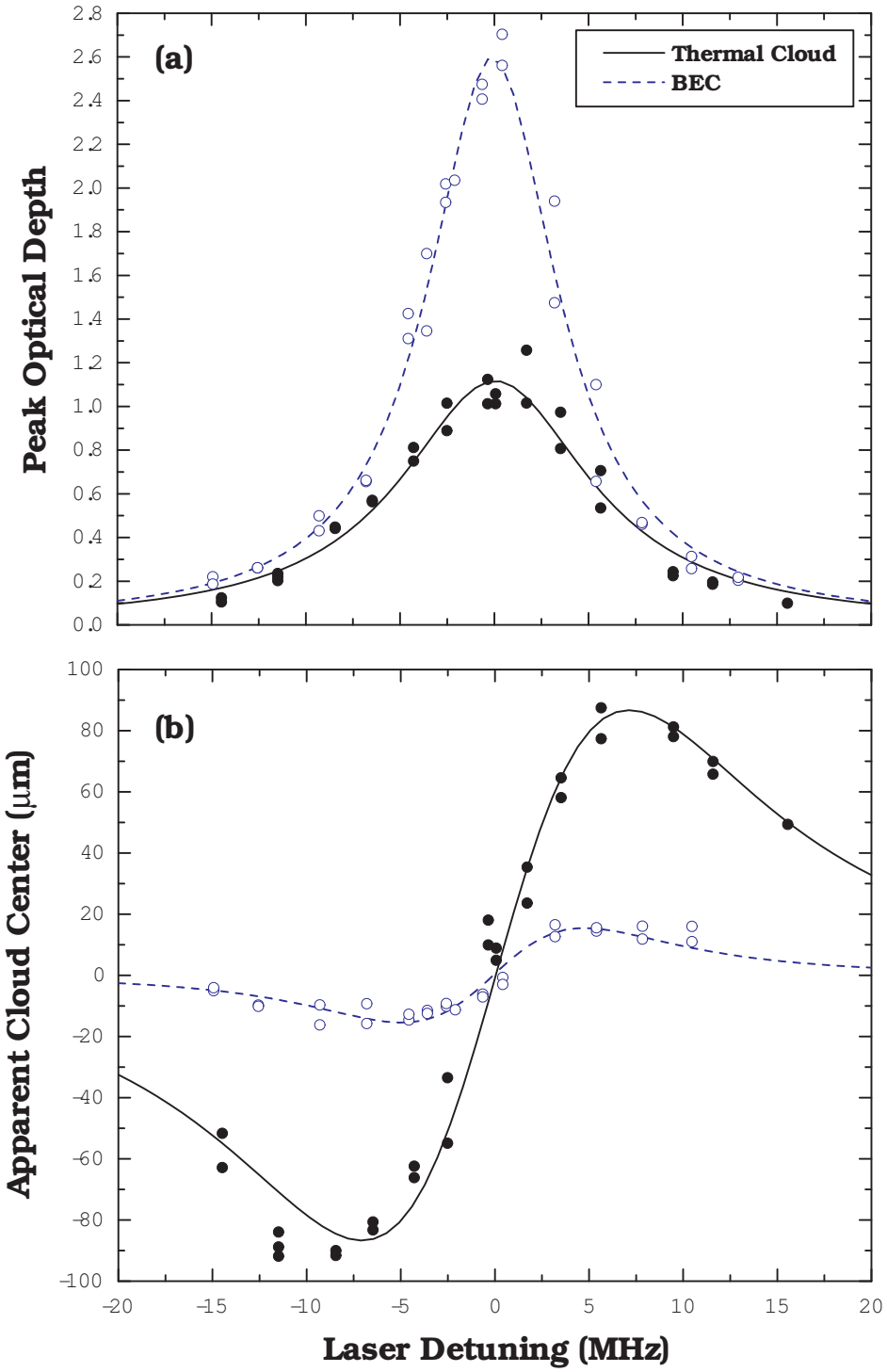

Figure 2.12: Imaging in a large magnetic field. The data in (a) shows the peak optical depth of a BEC (open circles) and a thermal cloud (closed circles) for various detunings of the probe laser. The presence of a large magnetic-field gradient during the image widens the transition due to the finite size of the clouds. The presence of the magnetic-field gradient also adds to an apparent shift of the center position of the atom cloud, shown in (b). The detuning from resonance of the laser frequency compensates the detuning of the atomic transition from the field gradient, which results in an apparent shift in the center position of the atom cloud. The large size of the expanded thermal cloud leads to very noticeable shift, while this effect is suppressed greatly for a BEC.

could produce unwanted collisions. The problem could sometimes be resolved by slightly adjusting parameters in the CMOT setup, or by adding light resonant only with the impurity state, thus selectively removing the impurity. In the past, this method of removing impurity states with light was implemented in order to be absolutely certain of the BEC state-purity. However, the light used in this setup was slightly detrimental to the BEC due to the fact that the chosen purification light was resonant with the $F = 2 \rightarrow F' = 2$ transition. Atoms in the impurity states ($|2, 1\rangle$ and $|2, 2\rangle$) could absorb and emit photons, which could lead to the atoms decaying back into the $|1, -1\rangle$ state with a great deal of energy, thus heating the cloud. The atoms could also simply collide with other atoms upon recoiling from the absorption of a photon, which could also heat the cloud or lead to a significant loss of atoms.

The solution, we found, was to apply light resonant with the $F = 2 \rightarrow F' = 3$ transition, and blowing the impurity state atoms out of the trap. This transition is a closed cycling transition, which means that an atom absorbing a photon up to the $|F' = 3\rangle$ state may only decay to the $|F = 2\rangle$ state. This method ensures that atoms have no possibility of decaying back into the $|1, -1\rangle$ state and no chance of heating the cloud in this way. This light was produced by applying an AOM to the unused zero-order beam of the probe laser (as shown in Fig. 2.1). This light had no adverse effects on atoms in the $|1, -1\rangle$ state.

2.2.6 Shielding an Oscillating BEC

In order to perform experiments which depend on measuring very small changes in the BEC-trapping frequency, we found it necessary to address the problem of background gas collisions heating the BEC. This heating becomes a problem in these types of experiments due to the fact that a nearly pure condensate ($N_{BEC}/N > 0.8$) will oscillate at a slightly different frequency than a lower fraction condensate. Fig. 2.13 shows the effect of the BEC number fraction on the measured trap frequency. In order

to perform high-precision work, the number fraction of the BEC should remain as close to constant as possible.

Applying constant radio-frequency radiation just above the final evaporation frequency has the effect of shielding the BEC from stray background atoms which are trapped in other states, known as 'Oort-cloud' atoms. The rf-shield used in this experiment is a bit more complicated, due to the fact that the BEC is oscillating in space. The finite size of the oscillation requires the shield frequency to be increased slightly (a few kHz) in order to prevent the atoms from becoming untrapped by oscillating through the shield. In addition, the presence of near-resonant rf-radiation leads to an AC Stark shift of the potential near the shield position, which can shift the trap oscillation period. This means a careful examination of the applied power of the shield is necessary as well.

The data in Fig. 2.14(a)-(c) shows the adverse effects of shield power on an oscillating BEC after 500 ms. The data in (a) shows the effect the additional AC Stark shift adds to the potential. The radial trapping frequency is perturbed greatly with a strong shield power (0 dBm), while it tends to be unaffected with smaller shield powers (-12 to -18 dBm). Additionally, one can see in (b) the effect the shield has on the size (and number) of the oscillating BEC. The illustration below (b) demonstrates how higher shield powers have the effect of biting into the BEC a bit more than weaker shield powers. The data in Fig. 2.14(c) demonstrates how the presence of the shield affects the BEC number fraction. Higher shield powers tend to have a detrimental effect on the BEC number fraction, heating the BEC, while lower powers tend to have the effect of preserving the number fraction, or even cooling the BEC a bit, creating a higher number fraction. The solid line represents the mean number fraction at the beginning of the oscillation (the dashed lines showing the standard deviation in the mean). Other data (not plotted) show that when the condensate starts with a number fraction > 0.8, shield powers in the range of -10 to -18 dBm would do a good job preserving that state of the BEC for the entirety of the oscillation.

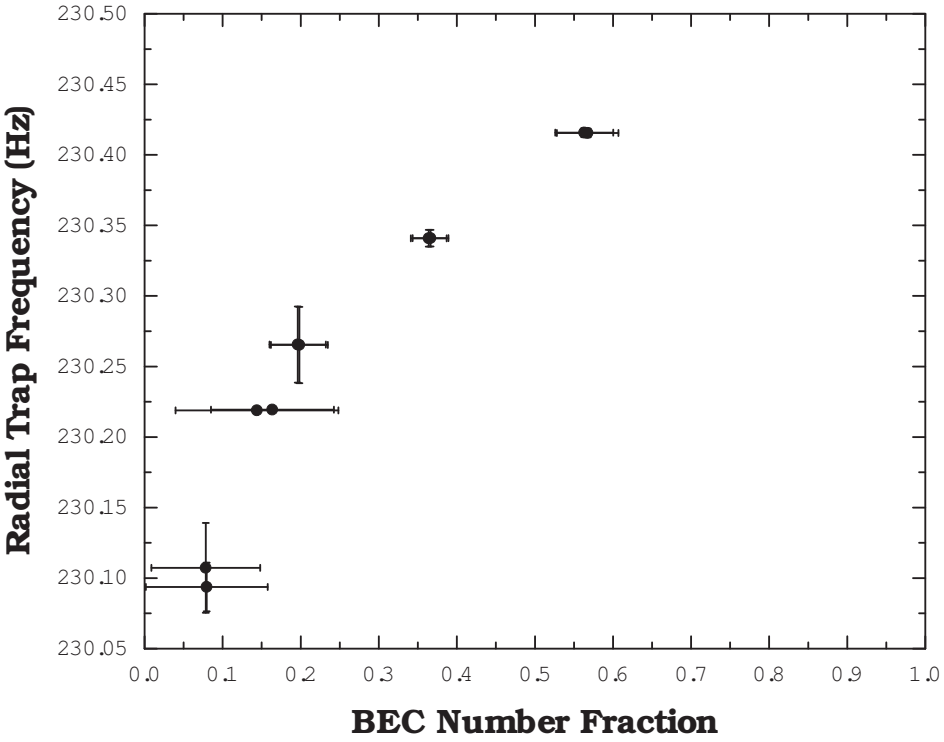

Figure 2.13: Trap frequency vs. BEC number fraction. The finite size of a BEC and thermal cloud in an anharmonic trap leads to a slight change in the trap frequency at the 0.1% level for various BEC number fractions (N_{BEC}/N). The presence of this effect requires a constant number fraction be maintained for the duration of an experiment (>1 s). Sec. 2.2.6 deals with the shielding issues used to suppress heating of the condensate.

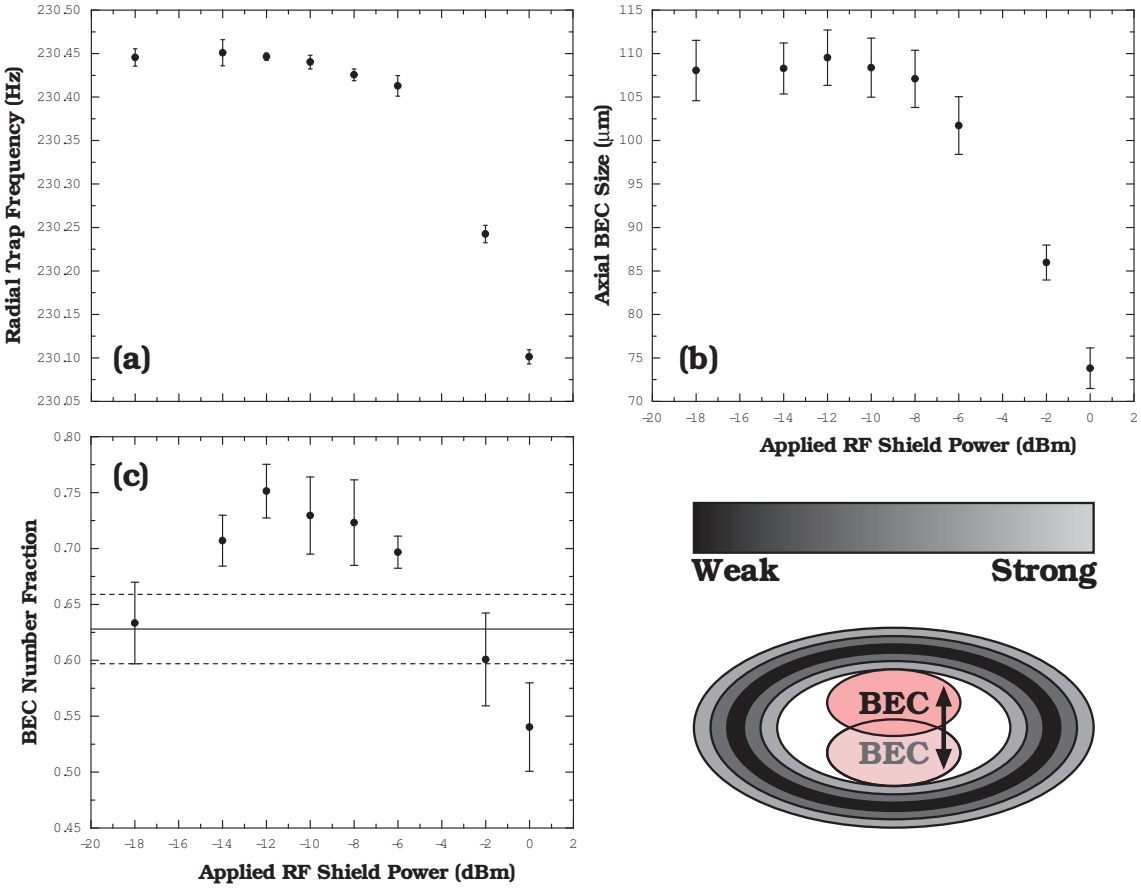

Figure 2.14: Effect of shield power. Shown in (a) is data taken varying the power of rf radiation applied to a BEC for shielding purposes (discussed in Sec. 2.2.6). The additional shield power adds to an AC Stark shift of the potential, which contributes to a change in the trap frequency. The data in (b) shows the effect the radiation has on the number of BEC atoms after 500 ms (indicated by the BEC size). Plotted in (c) is the BEC number fraction after 500 ms of oscillation time. The solid line corresponds to the initial number fraction (with error bounds). One can see a heating effect from high-*p*ower radiation, where the number fraction is reduced, and a cooling effect from lower-power radiation (higher number fraction). One can see the effect the shield has on the oscillating BEC graphically in the illustration. The stronger the rf power of the surrounding shield becomes, the wider its spatial extent becomes. The rf knife was held at 24 kHz above the final evaporation frequency for these measurements.

2.3 Science Cell Heating Techniques, Procedures and Concerns

This section of Chapter 2 details the various components of the apparatus used to uniformly heat our substrates and science cell. Resistive heaters, insulating fiber glass wraps and thermocouple junctions were used to create a temperature-servoed oven localized around the cell. Also included in this section is a discussion regarding the degradation of the UHV quality as the oven temperature was raised. The poor vacuum quality significantly inhibited our progress to make a measurement of a temperature dependence to the Casimir-Polder force with uniform heating. However, the analysis performed on the vacuum quality may be of use to others and is documented in this section.

2.3.1 Uniform Heating Circuitry

Our first attempt at measuring a temperature dependence to the Casimir-Polder force was done by a uniform heating method in which we raised the temperature of our science cell by placing resistive heaters in contact with the top and bottom of the cell (see the illustration in Fig. 2.16).[5] The temperature of the science cell was monitored by two thermocouple junctions. Each thermocouple was glued to a 5 mm $\times$ 5 mm piece of ceramic boron nitride, in order to avoid measuring point-contact 'hot spots' on the pyrex cell walls. The ceramic acts as a good 'averager' of the cell-wall temperature.

The circuit used to heat the chamber is shown in Fig. 2.15, in which the thermocouple leads are shown as a plus and minus on the left-hand side. The output of this circuit is meant to be fed into the voltage control of the power supply in order to servo the cell temperature. The graph in Fig. 2.15 shows the performance of the system over several hours. Analysis of the data taken from 3:15 AM to 6:00 AM shows a standard deviation of 76 mK over 165 minutes, which is largely, if not entirely, due to noise in

[5] The resistive heaters were powered by a Kepco power supply (model BOP10-10M).

the temperature acquisition (see Sec. 2.2.2 of this chapter).

2.3.2 Vacuum Degradation While Heating

During the heating experiments described in Sec. 3.3, we encountered a few problems with the vacuum quality as we heated the chamber. This difficulty had to do with the fact that we began to see a dramatic decrease in the number of atoms in our magnetic trap as we heated our vacuum chamber. This loss was attributed to the increase in the background pressure inside the chamber. Fig. 2.16(a) shows the effect heating the pyrex walls has on the magnetically-trapped cloud of atoms. This was, however, expected and we were able to achieve BEC with a surrounding environment temperature of $\sim 190^{o}$C.

As the pyrex temperature is increased, a dramatic decrease in the trap lifetime can be seen. At first we had assumed that the increase in the background pressure was due to an increase in the outgassing rate of the steel chamber walls, which were inadvertently heated as the pyrex heated. Fig. 2.16(b) shows that this is, in fact, not the case. By independently varying the temperature of the steel (by placing it in contact with a water-cooled copper coil), we could see that the increase in the background gas pressure was due to the heating of the pyrex walls and not the steel! This is indicated in Fig. 2.16(b) with two red arrows. The two outlying data points disagree significantly with the rest of the data (with the red-dotted line providing a guide to the eye).

The solid (red) lines in (a) and (b) are fits of the data. The two outlying points in (b) were masked during the fitting to illustrate the point that was made. The fit function that was used was obtained by assuming that there exists a background gas pressure that depends on the rest of the vacuum chamber and does not depend on the pyrex cell wall temperature or the temperature of the adjacent steel (as illustrated in the figure). This background (BG) pressure gives us a steady-state lifetime of atoms in the magnetic trap of τ_{BG} at room temperature, whose loss rate is given by $\gamma_{BG} = 1/\tau_{BG}$.

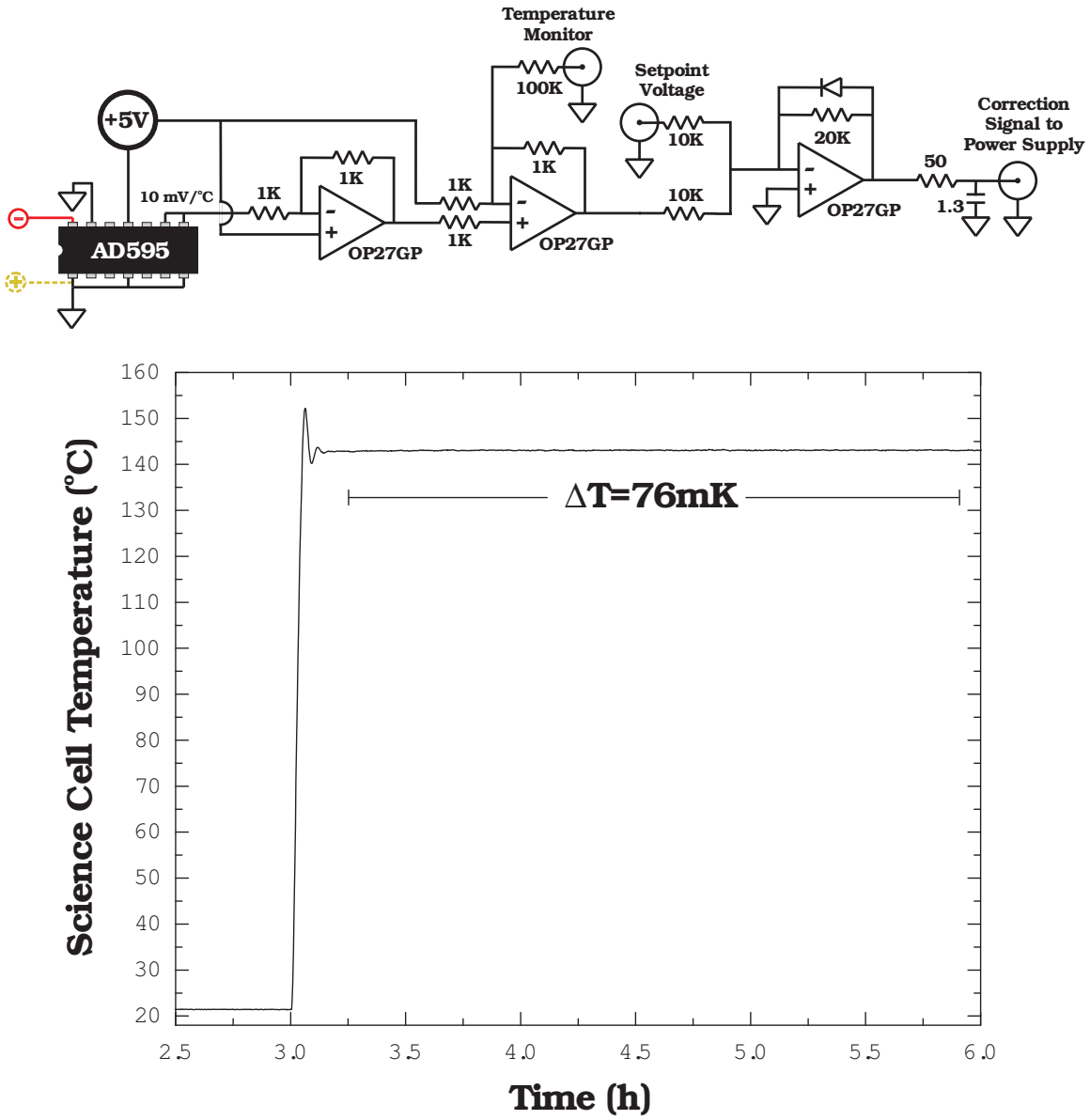

Figure 2.15: Uniform-heating circuit. Shown is a schematic diagram of the circuit used to provide uniform heating to the science cell. Resistance values are in Ω, while the capacitance value is in μF. Shown in the graph is the temperature of the science cell over several hours. The cell temperature was programmed to heat to 140°C at 3 AM. One can see a short 'rise-time', slight overshoot and damped oscillation of the temperature on the several-minute time scale. From 3:15 AM to 6 AM the temperature was maintained to a steady value with a 76 mK variation (most likely due electrical noise in the temperature acquisition).

The increase in pressure due to heating (H) would then come from an additional term $\gamma_H = 1/\tau_H$, which is exponentially dependent on temperature. The two loss rates would add together to produce a functional form of the lifetime that behaves like

$$\tau_{total}(T) = \frac{1}{\gamma_{BG} + \gamma_H e^{-T_o/T}}. \tag{2.3}$$

where T_o is a characteristic temperature associated with the 'turn-on' of the temperature-dependent loss. By fitting the data in (a) we find that the background lifetime $\tau_{BG} =$ 121.3(9)s, $\tau_H = 0.53(49)$ms, and $T_o = 5830(420)$K. The dashed (blue) horizontal line at 40 seconds in (a) is an estimate of the minimum lifetime needed in the magnetic trap to produce a BEC. This means that we would be limited to a science cell temperature of roughly 225^oC to make a *s*mall BEC, and an even smaller temperature to make a healthy, robust BEC.

The permeability of the glass vessel walls has been documented in a number of other sources, many of them dealing with light-bulb technology. The idea behind this loss mechanism is that the pyrex walls become more porous as they are heated and, in fact, become fairly permeable to helium gas. We can estimate the flux of atoms that make their way into the cell through the pyrex walls by analyzing the results of the fit earlier.

Since we believe the majority of the pumping of the gas in the science cell is done by ion pump #2 (a 40 L/s pump, see Fig. 2.3) and since we can estimate the background gas pressure ($\sim 10^{-11}$ torr), we can obtain a value for the throughput for the ion pump $Q_P = P_{BG}\ S_P$, where Q_P is the throughput of the pump, S_P is the pumping speed, and P_{BG} is the background pressure. The throughput is a quantity in vacuum science, analogous to current in electronics, which is a conserved quantity everywhere along the vacuum chamber. In steady-state, therefore, we can assume that the throughput being pumped is equal to the throughput created by the chamber walls, getters, etc. We estimate this quantity to be $Q_{BG} = (40\text{ L/s})\times(10^{-11}\text{ torr}) = 4\times10^{-10}$ L torr s^{-1}. This

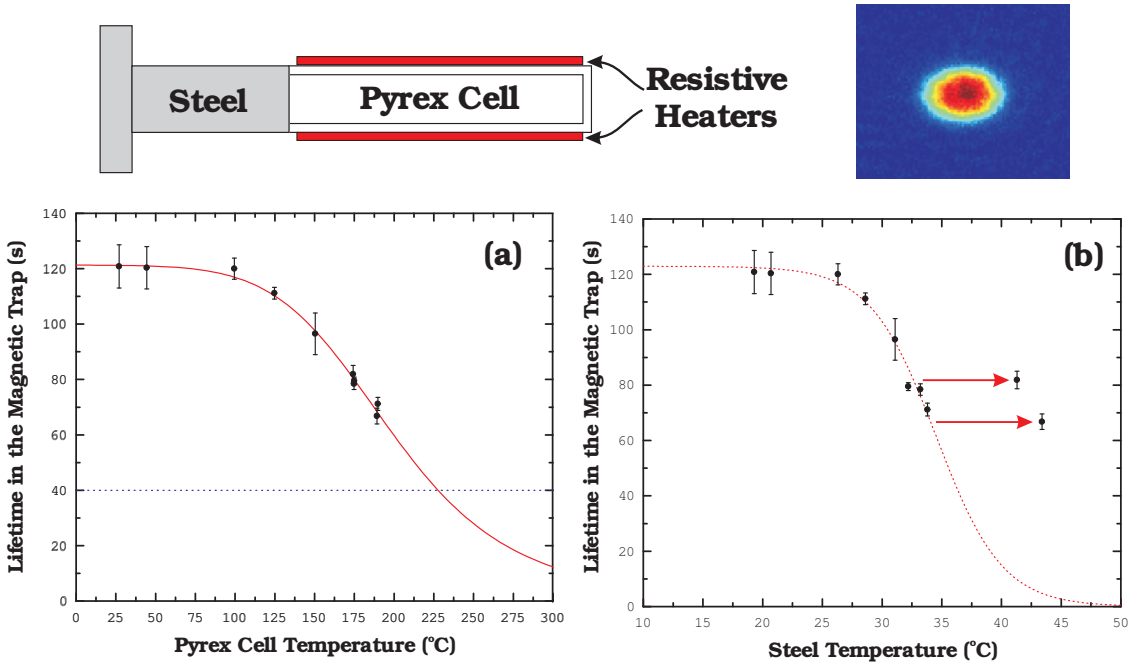

Figure 2.16: Vacuum issues while heating. Graphs (a) and (b) show the lifetime of magnetically trapped atoms taken inside the pyrex science cell. The lifetime of the atoms is a good indicator of the background gas pressure inside the chamber. Data was taken varying the temperature of the pyrex chamber walls with resistive heaters placed above and below the science cell. The temperature of the steel walls were found to increase due to thermal conduction and were varied with water cooling contacts. The data in (a) shows a very strong dependence of the lifetime on the temperature of the pyrex chamber walls (described in the text), while the data in (b) shows the same data plotted versus the steel temperature. Two red arrows point to two measurements that were made with the water cooling off. The change in the temperature of the steel led to no distinguishable change in the lifetime of the trapped atoms. The conclusion drawn from this is that the pyrex walls seem to be more permeable at hotter temperatures and led to a significant vacuum degradation. The dashed line in (a) represents the minimum lifetime needed to create a BEC and puts an upper limit on the hottest possible pyrex temperature. The image is of a BEC created while the science cell was heated to 190^{o}C.

quantity should be proportional to the background loss rate γ_{BG} and therefore inversely proportional to τ_{BG}. I'll call this proportionality constant a and write it as,

$$Q_{BG} = \frac{a}{\tau_{BG}}, \tag{2.4}$$

and $a = 5.1 \times 10^{-8}$ L torr.

We can then estimate the throughput through the pyrex wall Q_H by analogously associating it with the additional loss mechanism. The constant of proportionality should be roughly the same and we can say that,

$$Q_H(T) = \frac{a}{\tau_H} e^{-T_o/T}, \tag{2.5}$$

which gives a value of $Q_H(T) = 9.7(90) \times 10^{-5}$ Exp(-T_o/T) L torr s^{-1}, where T_o = 5800(420)K. Additionally, we can estimate the atomic flux Φ through the 1 mm thick pyrex walls at room temperature by dividing the throughput by the surface area of the pyrex chamber ($\sim$35.2 cm^2),

$$\Phi_H \approx 2.4(21) \times 10^{10} m^{-2} s^{-1}. \tag{2.6}$$

In order to minimize the effects caused by heating the pyrex walls, one could imagine using thicker pyrex, limiting the surface area of the pyrex, or eliminating the helium gas surrounding the cell. The latter would take a fair bit of effort, but one could imagine having a constant flow of an ultrapure, inert gas pass over the cell as it heats.

2.4 Laser-Heating Techniques, Procedures and Simulations

This section of Chapter 2 details the technique of heating our substrate with a high-power laser. The substrate is painted black with a graphite paint, which absorbs a significant fraction of the incident laser power, and heated to several hundred Kelvin. This section also outlines the finite-element analysis of the temperature profile across the substrate's surface and describes the calibration of the surface temperature to the

heating-laser power. This calibration uses a non-invasive, interferometric measurement to determine the substrate temperature.

2.4.1 Substrate Laser Heating

In this section, I discuss the methods used in heating a glass substrate with a high-power laser for the purpose of measuring a temperature dependence to the Casimir-Polder force.

The top side of the glass substrate was painted black with a colloidal graphite paint (Aquadag E) in order to absorb the light from the heating laser. This paint is composed of solid graphite particles (roughly 0.5–2 μm in size), NH_3OH, H_2O and a polysaccharide cellulose material (sugar). The sugar, we are told, acts as a glue to hold the graphite particles to the substrate and breaks down into solid carbon following a high-temperature bake. The company that develops the paint, Acheson Industries, recommends the following baking procedure, which we amended to meet our needs. This procedure worked very well and allowed us to heat our substrate to temperatures of 600 K while maintaining UHV conditions.

First, an unpainted substrate is slightly heated by placing it under a heat lamp on a glass table (a replica of the pyrex holder in Fig. 2.17) which is heated to $\sim 60^o$C and painted. The elevated temperature of the substrate helps the paint settle almost instantaneously when applied, and does not allow it to spread over the substrate's entire surface area. The substrate(s) and glass table are placed into an off-line vacuum chamber and heated to 150^oC for 1–2 hours. This stage of the bake is primarily intended to drive out all the water from the paint before a high-temperature bake. The presence of water during a high-temperature bake would have the effect of boiling the paint too rapidly and would create a cratered surface. At this point the vacuum temperature is raised slowly to 300^oC and baked for several hours. The temperature of the vacuum system is then raised once again to 450^oC for 1–2 hours. This last step in the bake-out procedure

is done primarily because we intend to heat the surface to temperatures in this range with the heating laser. It is advantageous to do this extremely hot-bake stage in an off-line vacuum chamber, rather than bake the piece at high-temperatures in the science cell. The paint was found to remain intact following a vacuum bake at 600^oC for three hours, but was found to disintegrate slightly at $\sim 700^o$C.

The bake leaves a very smooth painted graphite surface and also allows for placement of the painted substrate in a UHV chamber. The remaining solid graphite layer was found to absorb the power of the laser light with a remarkable efficiency. Ideally solid graphite will absorb $\sim$60% of 860 nm laser light, while we estimate that the graphite paint absorbs $\sim$50% of the applied light.

The heating laser used for this purpose was a high-power diode laser with a center wavelength of 860 nm, with a broad 2 nm laser linewidth. This diode, properly cooled, is capable of producing greater than 7 W of laser-light power (for our purposes, we only ever used 0-2 W of power). The laser produces an output of laser light which requires an variety of optics in order to get the beam semi-collimated. This beam was then manipulated with various optics to produce an incident beam profile whose spatial extent nearly matched that of our glass substrate.

A large laser spot was chosen in order to achieve near-uniform temperatures across the surface. Fig. 2.21 shows the results of a finite-element modelling program (described in Sec. 2.4.3) in which either a tightly-focused laser beam (a) or a broad-focus laser beam (b) are incident on the surface. The tightly focused beam produces a large temperature gradient across the surface, which would make interpreting the results of a Casimir-Polder experiment difficult. For this reason the broad-focus beam (analyzed in Fig. 2.21(b)) was used for the experiment.

Fig. 2.17 shows an illustration of our science cell apparatus with the applied heating laser. The laser is sent through the top side of the pyrex vacuum chamber walls, and strikes the graphite-painted side of the substrate. The substrates are set

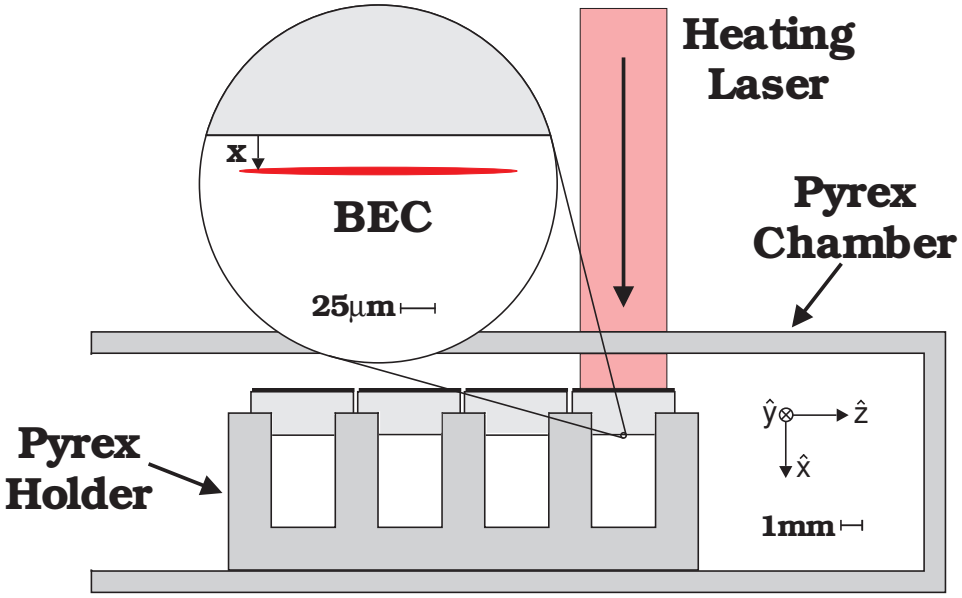

Figure 2.17: Laser heating of the substrate. Shown is a to-scale drawing of the science cell with the heating laser. The heating laser passes through the pyrex chamber wall and strikes the top-painted surface of one of the four substrates. The substrates are supported by a pyrex holder which allows the BEC to be formed beneath. Also shown in the figure is the coordinate axes referred to throughout this thesis.

in place on a pyrex table, which elevates the surfaces for BEC studies (the BEC is shown beneath the surface in the inset). The table and substrates have a small area of contact with one another, due to the surface roughness of the table. This lack of contact provides a great deal of thermal isolation to the substrate. When the heating laser is applied, the substrate's primary means of cooling is limited to radiative cooling and is not dominated by conductive cooling. This allows for substrate temperatures to exceed 600 K while the pyrex vacuum chamber remains at ∼300 K. This is important in the context of non-equilibrium Casimir-Polder forces, discussed further in Chapter 3.

When the experiment, detailed later on in this thesis, was conducted with a hot substrate (600 K) the heating laser was left on continuously, even during the imaging process, in order to avoid temperature instabilities. The presence of the high-power laser light led to a great deal of light being scattered about the apparatus. In order to accurately image the BEC onto the CCD camera without observing interference from the heating-laser light, a pair of filters were added to the camera to extinguish the high-power 860 nm light on the CCD and allow the 780 nm imaging light to remain. *A*n edge-pass filter was used for this purpose, which transmits 85% of 780 nm light, while transmitting only 0.01% of 860 nm light. The high intensity of the heating laser required us to use two filters in order to nearly extinguish the heating-laser light.

2.4.2 Interferometric Measurement of Substrate Temperature

In order to accurately determine the temperature of the substrate in the vacuum chamber, an off-line experiment was performed in which the temperature of the substrate was calibrated to the incident power of the heating-laser beam. The off-line experiment was set up to be nearly identical to the main apparatus. The only geometric detail that differed between the two setups was the addition of two reflective gold layers to the off-line substrate (see Fig. 2.18). The gold layers were patterned onto the substrate by vapor deposition, thick enough to provide a nearly 100% reflective surface.

The temperature of the substrate was determined by measuring an interferometric signal which is proportional to temperature changes. The basic idea of the interferometer is that a laser beam is split by a 50-50 beam splitter (a semi-reflective gold mirror coated to be 50% reflective at the wavelength of the laser), with one of the two beams of the interferometer passing through the glass substrate, reflecting from the back surface and returning along its path to be recombined with the other interferometer beam on a photodiode. The second interferometer beam reflects from the front surface of the substrate and acts as a reference beam to provide an interference effect. The difference in phase between the two paths determines the interferometric signal on the photodiode. Because one of the beams passes through the material and one beam does not, the interference signal is dependent on the material properties and substrate thickness, which themselves are dependent upon temperature.

More specifically, the interferometric signal recorded on the photodiode will look like a sine wave, whose phase depends upon the temperature change of the substrate. The number of fringes ΔN recorded on the photodiode is proportional to the change in temperature ΔT and depends upon the index of refraction of the material n, the thickness of the material t, the linear coefficient of thermal expansion α, and the wavelength of the interferometer laser λ.

The interferometric signal comes from the addition of two effects: (1) thermal expansion as the material is heated and (2) the change in the material's index of refraction with temperature dn/dT. It is important when calculating the interferometric signal that one accounts for both effects. For instance, the latter of these two effects is the more dominant by a factor of 15 for fused silica, due to the fact that fused silica's thermal expansion coefficient is very small, while the two effects are nearly equal for crystalline sapphire.

One can derive an equation for the number of interferometric fringes recorded as a function of the change in temperature by looking at Fig. 2.18. The path difference

between the two interferometer beams will be equal to some free-space path difference ΔL, due to the fact that one of the beam paths is longer (this does not vary with temperature), and a path difference due to the presence of the substrate $2nt$, which does vary with temperature. We can write the relation between the path length and the number of fringes,

$$N\lambda = 2nt + \Delta L. \tag{2.7}$$

To see an interference effect, the path difference must depend on temperature. Therefore, if we take the derivative of this equation with respect to temperature, we will have a relation for the number of interferometric fringes for a change in temperature dT,

$$\frac{d}{dT}(N\lambda) = \frac{d}{dT}(2nt + \Delta L). \tag{2.8}$$

The only parameters that depend upon temperature are the index of refraction n, the thickness of the substrate t and the number of fringes N,

$$\frac{dN}{dT} = \frac{2}{\lambda}\frac{d}{dT}(nt). \tag{2.9}$$

By applying the chain rule, we may write the above equation as,

$$\frac{dN}{dT} = \frac{2}{\lambda}(t\frac{dn}{dT} + n\frac{dt}{dT}). \tag{2.10}$$

Looking at this equation, we can relate the change in the thickness of the substrate with temperature to the thermal expansion coefficient, $dt/dT = \alpha t$, and write the change in index of refraction with temperature dn/dT as n', a constant of the material.[6]

We can then write the equation for the number of interferometric fringes ΔN for a change in temperature ΔT as,

$$\Delta N = \frac{2t}{\lambda}(n' + n\alpha)\Delta T, \tag{2.11}$$

where dN/dT has been written as a finite difference $\Delta N/\Delta T$.

[6] This term is not necessarily a constant, but a known value which depends upon the laser wavelength and the temperature range. It can be found by searching through volumes of optical constants.

Fig. 2.18(b) shows an interferometer signal ($\sim 30^o$C/fringe) recorded on a photodiode as the substrate was heated over 300 K above room temperature. The signal shows that the photodiode records a flat signal from 0-2 minutes, at which point the heating laser is slowly turned on. The substrate was heated slowly for the calibration and was found to maintain a very steady temperature for long periods of time (t = 10-22 minutes in (b), for example).

It should also noted that the terms dn/dT and dt/dT have been approximated as constants. This approximation is very accurate for temperature differences of a few hundred Kelvin. Second order terms were used in our estimation of the temperature, just to be safe.

Fig. 2.18(a) shows the results of our off-line calibration. The filled (blue) circles show data taken, in which the temperature of the substrate is determined interferometrically, while the power of the laser is measured with a power meter. The solid (red) line is a power-law fit to the data, while the dotted (red) lines are the error bounds of the calibration (used in estimating our uncertainty in the substrate temperature). This calibration shows a power-law dependence of the substrate temperature with laser power and allows us to accurately determine the substrate temperature in the main experiment by applying a known laser power to that substrate.

The open circles in Fig. 2.18(a) are estimates of the substrate temperature based on a finite element modelling (FEM) program, described below in Sec. 2.4.3, where the error bars represent the range between the maximum and minimum substrate temperature.

This interferometric technique provides a precise way to measure a substrate's temperature without the perturbative effect of a physical-contact thermometer which may provide an unwanted source of heating or cooling. While it is possible for other temperature measurements to be made without physical contact, our technique provides an unambiguous measurement of the substrate temperature and does not rely on

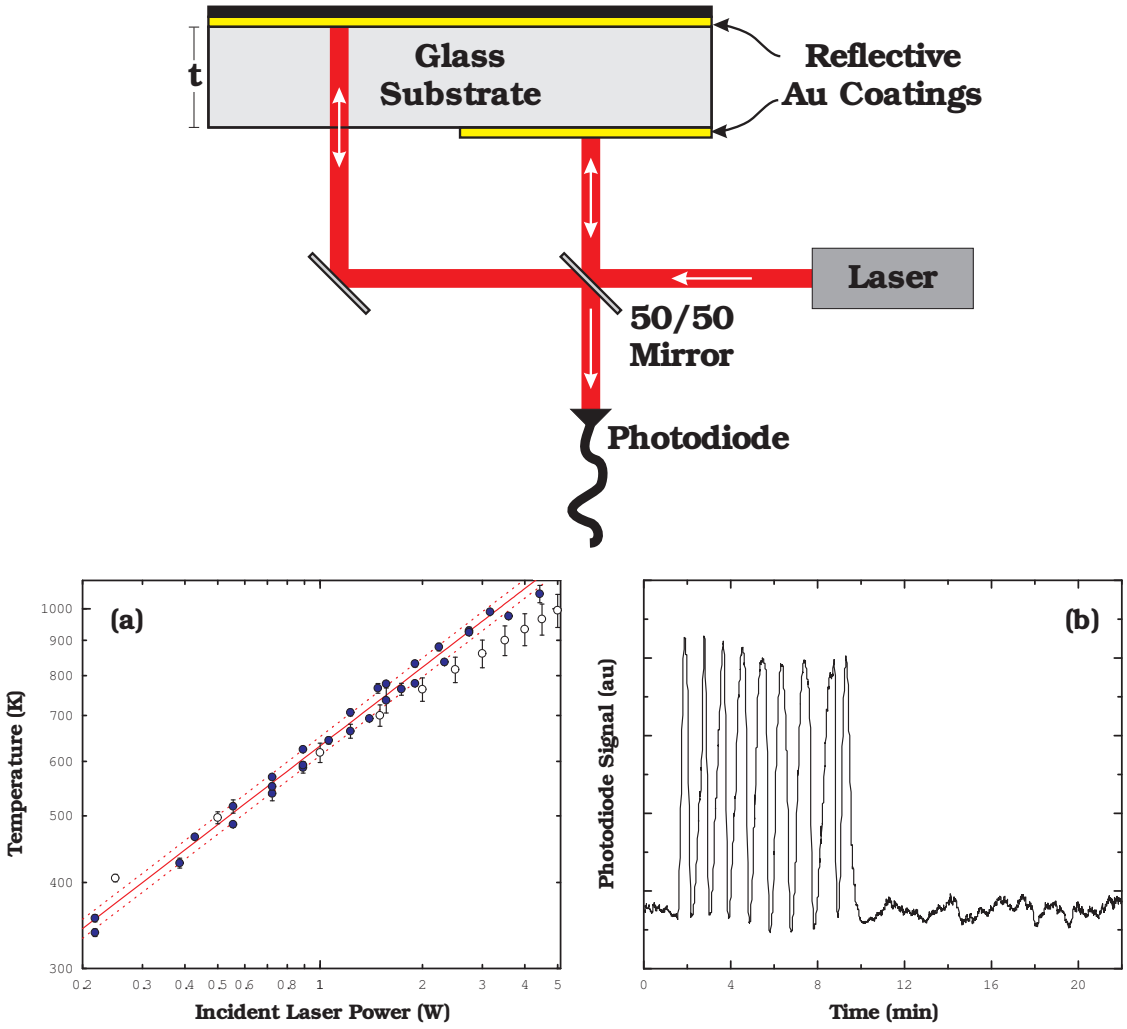

Figure 2.18: Interferometric temperature measurement. Shown in this figure is an illustration of the interferometric measurement that was made to infer the substrate temperature. The substrate is patterned on the top surface with gold and half-patterned on the bottom surface to allow one arm of the interferometer access through the material. As the material heats, it changes in length and also changes its index of refraction. The combination of the two effects leads to an interference signal proportional to the substrate temperature as it heats (shown in (b)). This procedure can be repeated, varying the power of the incident heating laser. The filled blue circles in (a) represent a calibration of the substrate temperature to the incident power of the heating laser. The open circles represent similar results from a finite-element-modelling program.

measurements of absolute blackbody radiation intensities, which could be corrupted by an intermediate material.

To test the accuracy of our interferometric method, an additional off-line experiment was conducted in which uniform heat was provided to both the substrate and the vacuum chamber. Resistive heater tape surrounded the chamber in order to ensure uniform temperatures. The temperature of the chamber was measured with a thermocouple junction and raised very slowly over a period of several hours. We raised the chamber temperature very slowly in the hope that a measurement of the chamber walls would be a good indicator of the substrate's temperature. We could then test the accuracy of our method by measuring the interferometric signal on our photodiode as a function of the known substrate temperature and compare the results.

Fig. 2.19 shows the results of this test. The interferometric signal is plotted in (a) as a function of the measured substrate temperature, and shows very nice, high-contrast fringes. The temperature of the substrate is then calculated by extracting the phase of the interference fringe from a fit to the photodiode data. A running window (shown in (a) as a red dotted-line box) fits the enclosed data to a sine wave and records the phase of the fit as a function of the substrate temperature. The phase of the fringe directly gives a measurement of the substrate temperature and is plotted in (b).

The data shows agreement between the measured and calculated substrate temperature. The dashed black line in (b) shows the expected substrate temperature. The disagreement between the two at temperatures larger than 150^{o}C is most likely due to time lags in the heating, where the substrate temperature and chamber temperature are not fully in equilibrium.

2.4.3 Finite Element Analysis of the Substrate Temperature

In order to properly understand the variation in temperature across our substrate, we designed a finite element modelling (FEM) program to analyze the surface temper-

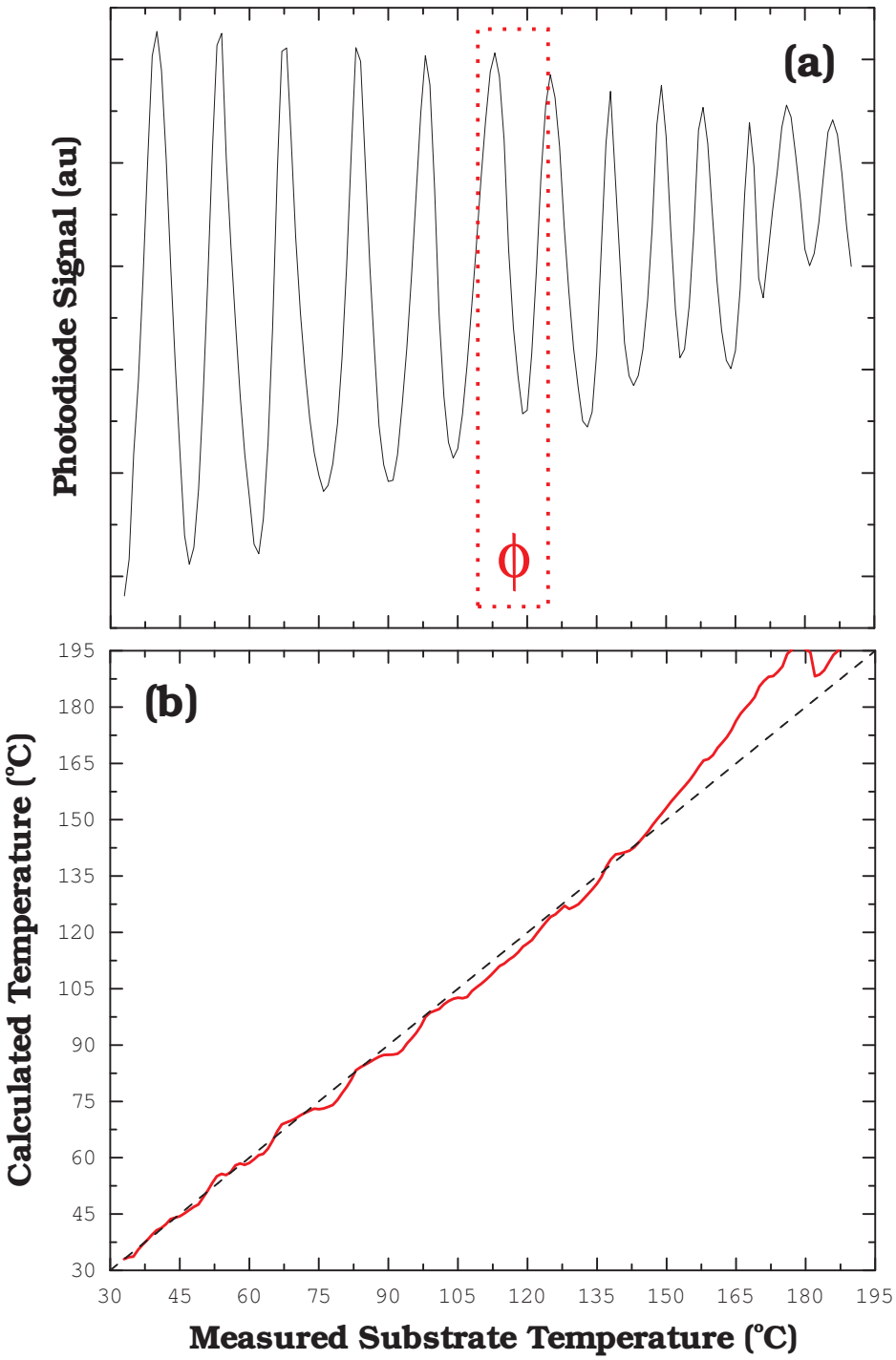

Figure 2.19: *I*nterferometer test. The data shown in (a) shows similar interference fringes to Fig. 2.18(b). This data, however, was taken with uniform heating of the entire glass cell in order to compare the temperature inferred from the interference effect to the known temperature surrounding the cell. The temperature of the substrate was calculated by fitting one period of the fringe to a sine wave and extracting its phase, which is proportional to its temperature. The fit window (dotted red box) was then run across the data, which gave a running measurement of the substrate temperature. The results, shown in (b), agree very well with the measured temperature up to $\sim 150^{o}$C. The decrease in the fringe contrast is due to a systematic drift in the position of the interference signal on the photodiode.

ature. The FEM program essentially breaks up the surface into an $N_y \times N_z$ array of tiny surfaces, where the number of 'pixels' in the k-direction N_k is equal to the size of the substrate L_k divided by the size of the pixel ds. The program then calculates the temperature of *each* pixel by analyzing its heating and cooling mechanisms with its nearest neighbors and the environment.

Illustrated in Fig. 2.20, each surface is able to (1) conduct and receive heat from its nearest neighbor, (2) radiate and absorb blackbody radiation, and also (3) absorb laser radiation. If we look at the $(i,j)^{th}$ pixel of the surface, we can write down an equation for both the power going into the substrate and also the power going out. The power absorbed through both blackbody radiation and through laser radiation is equal to

$$P_{abs} = (\epsilon_u + \epsilon_d)\ \sigma_B\ ds^2\ T_o^4 + P_{L;i,j}, \tag{2.12}$$

where each pixel, with area ds^2, absorbs power according to the Stefan-Boltzmann Law. Here T_o is the temperature of the surrounding environment, usually room temperature, σ_B is the Stefan-Boltzmann constant, and ϵ is the emissivity of the surface for the upper side u and the down side d. $P_{L;i,j}$ is the power absorbed from laser radiation and will be dependent upon i and j for a non-uniform heating-laser beam profile.

The power radiated by each surface is similar in form,

$$P_{rad} = (\epsilon_u + \epsilon_d)\ \sigma_B\ ds^2\ T_{i,j}^4, \tag{2.13}$$

where the radiated power depends upon the temperature $T_{i,j}$ of each element. Also we will abbreviate the total emissivity for the upper side and the down side to be $\epsilon = \epsilon_u + \epsilon_d$.

The heat conducted between neighboring pieces is a bit more difficult. For each surface there will be four terms coming in (one for each neighbor) and four terms going out. The heat conducted out is given by Fourier's Law of conduction,

$$P_{cond} = 4\ \kappa\ \frac{A_{xs}}{ds}\ T_{i,j}, \tag{2.14}$$

where κ is the thermal conductivity of the material, A_{xs} is the cross-sectional area of the material ($ds \times t$).

Similarly, the equation for the power received is equal to,

$$P_{rec} = \kappa \, \frac{A_{xs}}{ds} \, (T_{i+1,j} + T_{i-1,j} + T_{i,j+1} + T_{i,j-1}). \tag{2.15}$$

for the sake of brevity we will refer to the term in parenthesis as the sum over nearest neighbors and refer to it by writing Σ_{nn}.

Putting all of the powers in and out together,

$$P_{in} = \epsilon \, \sigma_B \, ds^2 \, T_o^4 + \kappa \, t \, \Sigma_{nn} \, T_{nn} + P_{L;i,j} \tag{2.16}$$

$$P_{out} = \epsilon \, \sigma_B \, ds^2 \, T_{i,j}^4 + 4 \, \kappa \, t \, T_{i,j}. \tag{2.17}$$

In order to analyze the system in equilibrium we must set the power in to be equal to the power out. Additionally, one should notice that the power in for each surface will be a constant, independent of the surface temperature $T_{i,j}$. The resultant equation will be a fourth-order polynomial in $T_{i,j}$ of the form,

$$T_{i,j}(T) = a \, T^4 + b \, T + c = 0, \tag{2.18}$$

where $a = 2 \, \epsilon \, \sigma_B \, ds^2$, $b = 4 \, \kappa \, t$ and c can be broken up into three terms: the term dependent upon the laser power $c_1 = -P_{L;i,j}$, the absorbed-power term $c_2 = -2 \, \epsilon \, \sigma_B \, ds^2 \, T_o^4 = a \, T_o^4$, and the received-power term $c_3 = -\kappa \, t \, \Sigma_{nn} \, T_{nn} = -b/4 \, \Sigma_{nn} \, T_{nn}$.

The solution to this equation is quite complicated and is solvable by a program such as *Mathematica* and will depend on a, b, c_1, and c_2. The idea of the FEM is to solve this equation for each $T_{i,j}$ on the surface for a number of iterations until convergence (equilibrium) is reached.

The results of the FEM analysis are shown graphically in Fig. 2.21, in which the temperature profile of the substrate is shown across the surface for (a) a very intense heating beam (1 W of power focused to an e^{-2} diameter of 200 μm), and (b) a less

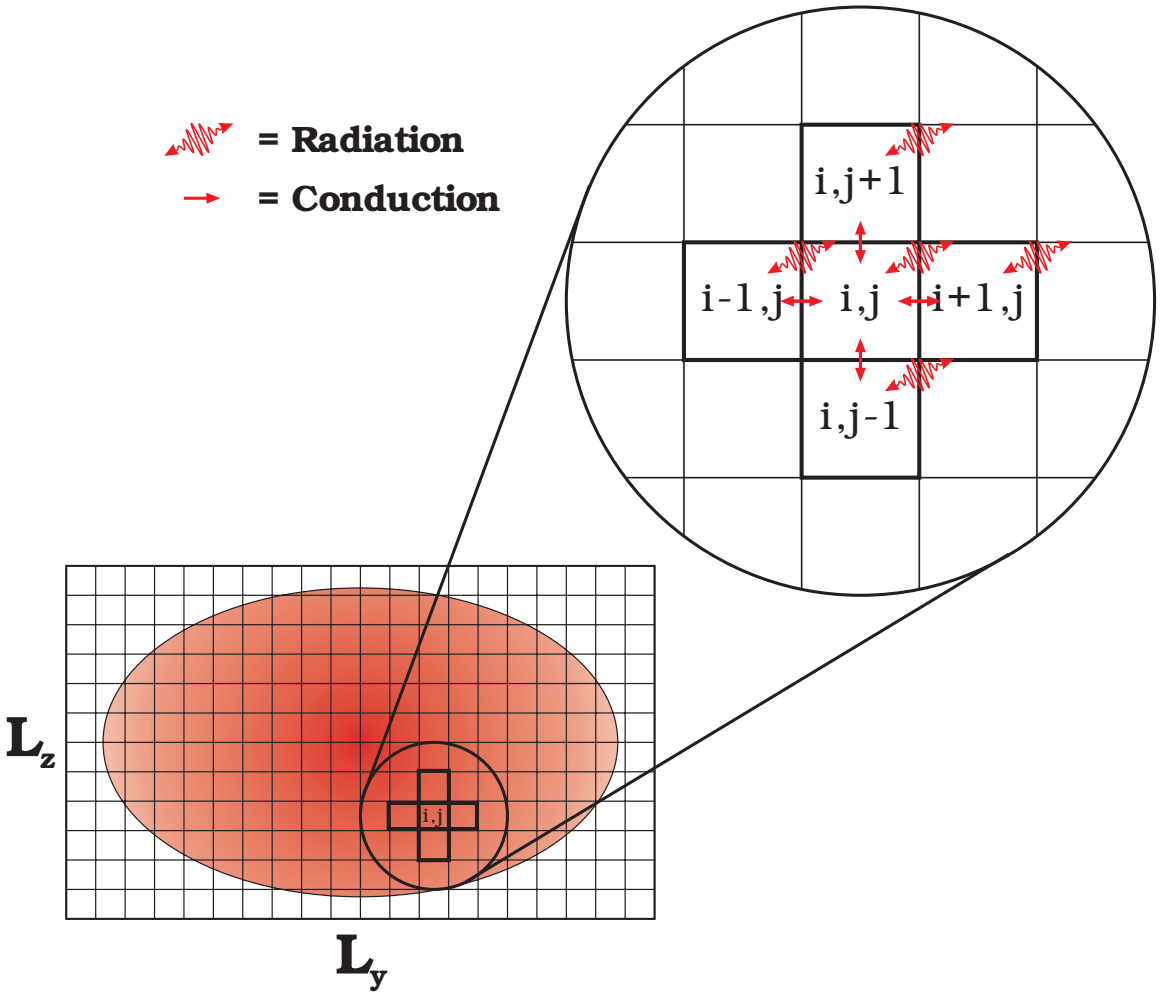

Figure 2.20: Finite element model (FEM) of the surface temperature. This figure illustrates the FEM technique of calculating the temperature at every point on the substrate's surface. The surface is divided up into an $N_y \times N_z$ array of pixels. Shown in the inset are the various heating and cooling processes that may happen to the $i \times j^{th}$ element. This element may conduct heat to and from its nearest neighbors and also absorb and emit radiation. The elliptic profile on the surface represents the profile of the heating laser. This laser profile adds a heterogeneous heating pattern to the substrate. The results of the FEM calculation are shown in Fig. 2.21.

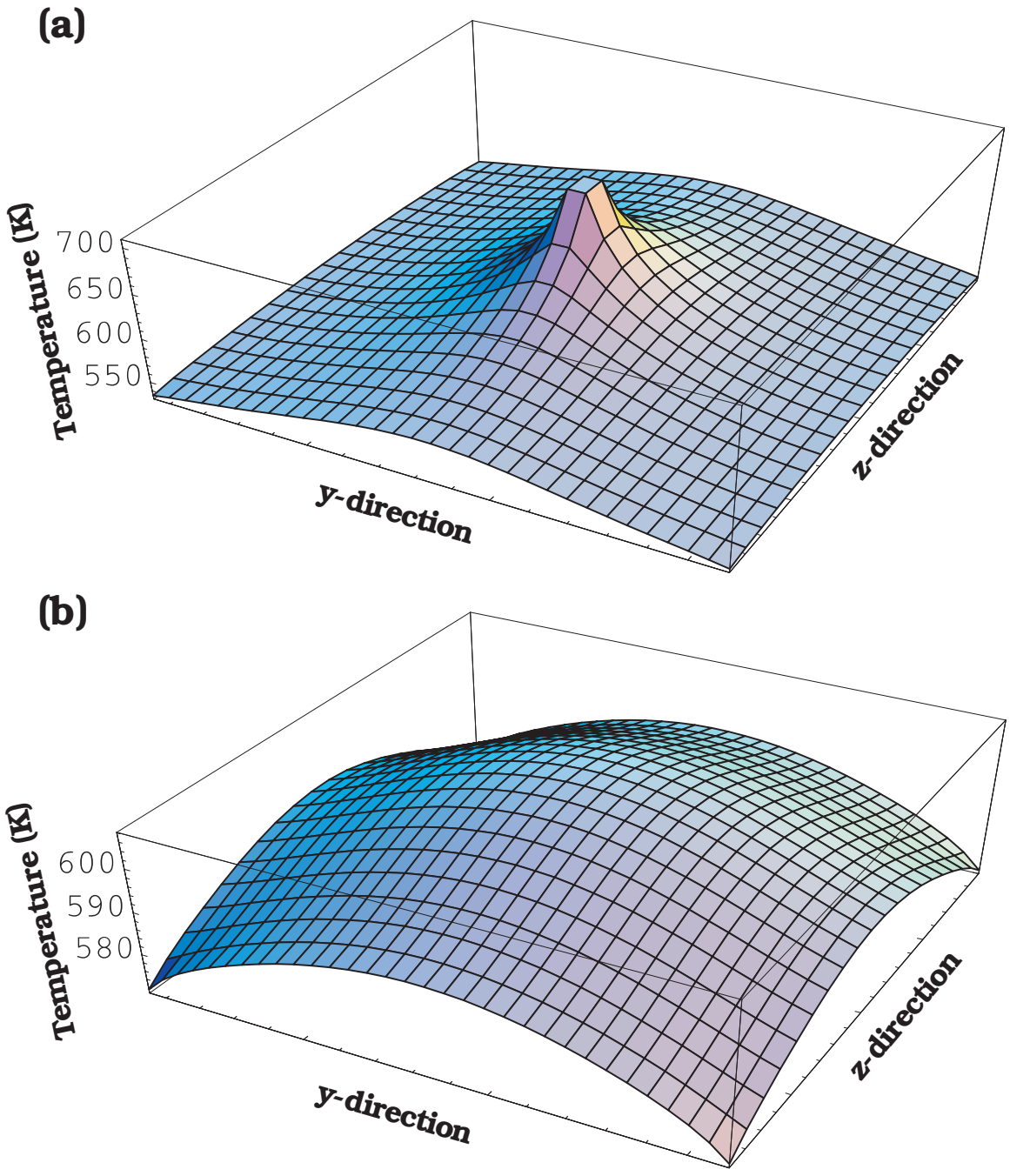

Figure 2.21: Finite element modelling result. These 3-D images show the temperature profile across the substrate for (a) a focused heating laser beam (1W of power focused to 200 μm), and (b) a broad laser beam with the same power (1W, 4 mm focus). The broad laser profile acts to heat the substrate more uniformly than a focused beam. The FEM process calculates the temperature for each surface element 5000 times in order to reach equilibrium. The profile in (b) matches the conditions used in measuring the temperature dependence of the Casimir-Polder force, discussed in Chapter. 3.

intense beam with the same total power (1 W, 4 mm focus). The dramatic difference between a focused heat source (a) and a broad, uniform heat source (b) is quite apparent. The temperature range across the surface in (a) is ∼170 K compared to a ∼35 K range in (b). The profile in (b) is our most accurate estimation of our substrate's temperature profile for the 605 K scenario in Chapter 3.

Our FEM program takes into account edge effects for elements on the sides and corners of the substrate, and conductivity effects from the substrate holder (which explains the cooler corners in Fig. 2.21).

The results of the FEM analysis agreed very well with the temperature calibration described earlier in Sec. 2.4.2 with only slight disagreements. The disagreement between the measured substrate temperature and the temperature estimate from the FEM could be attributed to an uncertainty in the heat conductance across the point contacts at the substrate corners, or the uncertainty in how much power is lost or convected away from atmospheric contact with the pyrex vacuum chamber walls.

One would expect to find an average substrate temperature that has a $P^{1/4}$ dependence on the laser power (from the Stefan-Boltzmann relation) instead of a power-law dependence of $P^{0.38}$, as measured from the calibration data. This discrepancy may be due to a poorly calibrated power meter, or may be due to a temperature dependent heat-loss mechanism, like a convective heat-loss process such as air-cooling of the chamber walls. Whatever the discrepancy, the calibration remains accurate at determining substrate temperature due to the fact that the same power meter measures both the laser power in the off-line calibration measurement and the laser power in the main chamber.

Additional analysis was performed on the variation in the substrate temperature from top to bottom. Fig. 2.22 shows the average surface temperature for the top surface of a 2 mm thick substrate (black solid line), and bottom surface (green dotted line). The difference in temperature between the two surfaces comes from the fact that heat

from laser power is absorbed by the top surface, which then conducts down through the substrate. Additionally, the bottom surface has a much higher emissivity, which means it loses more heat to radiation than does the top surface. The difference between the two surface temperatures leads to some ambiguity about the characteristic temperature of the blackbody fields affecting the atoms near the surface. Radiation coming from material further than a skin depth inside the material is absorbed and reradiated. Therefore only emission within a few skin depths of the material should contribute to Casimir-Polder forces. However, these skin depths may be large, and the temperature difference between the top and bottom surface of the substrate contributes to the error bar in our estimate of the characteristic temperature of the substrate's radiation.

2.5 Comments and Concerns on Metal Selection and Deposition

This final section of this chapter deals with the techniques and concerns regarding the patterning of metal onto our substrate's surface. Three metals were used in this experiment in an attempt to measure the temperature dependence of the Casimir-Polder force over a metal (as opposed to that already measured over glass), and also to measure the properties of adsorbed rubidium atoms on metals. The experiments performed over metals are shown in Chapter 4. Significant problems were discovered regarding the quality of the metals and are described in Sec. 2.5.2.

2.5.1 Metal Selection

Following the measurements described in Chapter 3, we decided to perform similar measurements over a metallic surface in order to learn more about the Casimir-Polder force between an atom and a metal (specifically its temperature dependence). We decided to prepare a number of substrates, each with its own unique coated metal layer. We investigated the following metals: hafnium (Hf), yttrium (Y), lutetium (Lu) and zirconium (Zr). These metals were chosen from a large number of possible metal

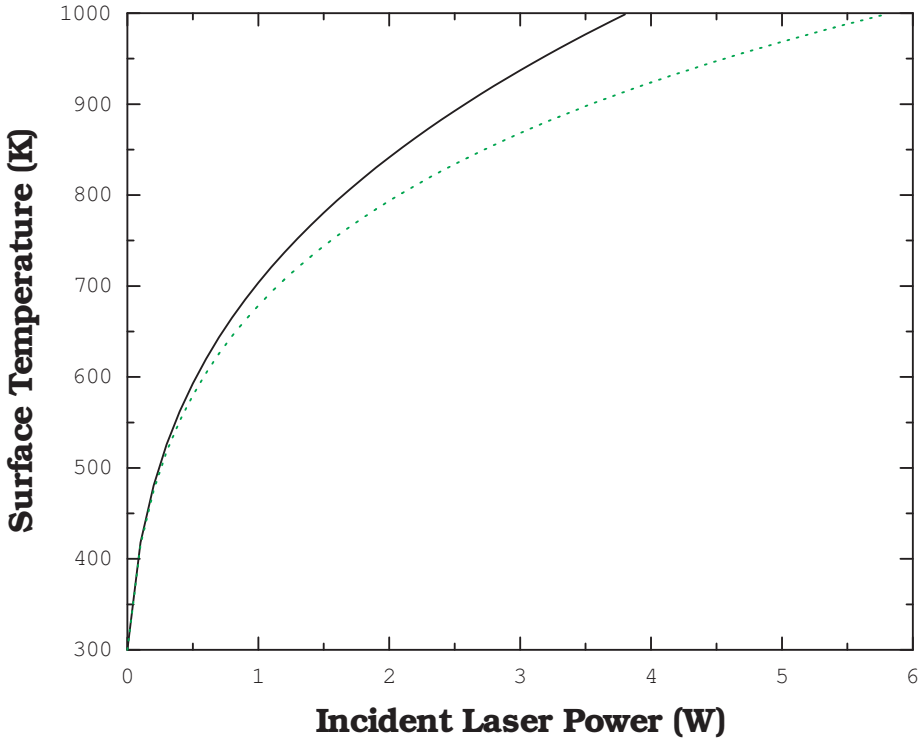

Figure 2.22: Substrate temperature gradient. This figure shows the effect laser heating the top surface (solid black line) of the substrate has on the bottom surface's temperature (dotted green line). The difference between the two temperatures is inversely related to the thermal conductivity of the material. Because it is relatively unclear from where in the material most of thermal radiation originates, the difference between the two temperatures is added to the uncertainty in the substrate temperature in Chapter 3.

Metal	WF (eV)	Magn. Susc. $(\mu/\mu_o\text{-}1)\times10^6$	Melt. Pt. (^{o}C)	Skin Depth (μm) @ 500 nm	@ 20 μm	@ 6.8 GHz
Hf	3.9	75	2230	0.012	0.08	3.62
Y	3.1	191	1530	0.016	0.10	4.71
Lu	3.3	1	1650	0.016	0.10	4.66
Zr	4.1	-122	1850	0.013	0.08	3.93

Table 2.2: Metal selection chart. This chart shows the important parameters used in selecting metals with which to study the Casimir-Polder force. These parameters include the material's work function WF, magnetic susceptibility μ, melting point, and skin depths for various radiation, all of which can be found in the CRC Handbook. In the end, the three metals with the lowest work functions were selected (Hf, Y, and Lu).

candidates for a number of reasons (see Table 2.2).

First, the metals listed in the table all have properties conducive to UHV environments, in that they all have vapor pressures orders of magnitude lower than our background pressure in the science cell ($\sim 10^{-11}$ torr), and they all have melting points much higher temperatures than our experiment could possibly attain.

Second, each of the four metals listed has a work function (WF) which is slightly lower in energy than the ionization energy of rubidium (IE = 4.177 eV). This is important when probing atom-surface interactions with alkali metal BECs– the low ionization energy of the gas-phase alkali atom implies that its valence electron finds it energetically favorable to reside in the solid metal, supposing the work function of the material is the larger of the two quantities. It is therefore conducive to atom-surface interaction measurements that a low-work function material be chosen to reduce these problems. This is discussed further in Chapter 4.

Another criteria in the search for metals to study is the requirement that the metal be 'invisible' to microwave and radio-frequency radiation. This requirement comes from the fact that atoms near the metal surface will need to be uniformly shielded with rf-radiation to maintain a stable BEC for $\sim$1 second (see Sec. 2.2.6). Additionally, atoms near the surface will need to be ARPed with microwave radiation in order to be imaged

(see Sec. 2.2.3). The parameter that determines whether or not an object is 'visible' or 'invisible' to radiation is the ratio of the skin depth of the material to the material's thickness– a parameter which varies from material to material and has a functional dependence on radiation frequency. The skin depth δ of a material is given by the following equation,

$$\delta = \sqrt{\frac{2\varepsilon_o c^2 \rho}{\omega}}, \tag{2.19}$$

where ρ is the resistivity of the material, and ω is the frequency of the radiation. If the material is thicker than the skin depth, we would say that the material is 'visible' because the radiation can be absorbed or scattered by the material. Likewise, if the material is thinner than the skin depth, the material is virtually invisible to that radiation.

Table 2.2 shows the skin depth of the four materials for 500 nm radiation (corresponding to visible light), 20 μm radiation (corresponding to infrared (IR) light or thermal radiation), and 6.8 GHz microwave radiation (for ARPing). A material thickness must be chosen to be thinner than the skin depth for the microwave radiation,[7] but greater than the skin depth for IR radiation. The reason we require the material to be greater than the IR skin depth is that measurements of the Casimir-Polder force depend greatly on the interaction of visible and IR radiation with the surface and atoms. If the material were transparent to visible and IR radiation, the material would behave like the vacuum and the Casimir-Polder force would have no contribution from the metal at these wavelengths.

One can see from this table that by choosing a material thickness much greater than 0.1 μm and much less than 3.6 μm one may eliminate any ill effects on the microwave and radio-frequency radiation, yet still maintain a 'proper' surface to visible and IR radiation. Similarly by choosing thicknesses smaller than a few μm, we may eliminate any ill effects from Johnson-noise on magnetically trapped atoms that have

[7] The skin depth for radio-frequency radiation is much higher than that of the microwave and therefore does not pose a constraint.

been seen before with this apparatus [15].

In addition, the fact that we work with magnetically trapped atoms means that we are sensitive to magnetic-field distortions. Listed in the table are values for the magnetic susceptibility of the four materials. It is preferable that the chosen materials have a relatively small magnetic susceptibility and thus a small sensitivity to magnetic fields. All four of these values are relatively small and did not pose a problem.

All four elements in Table 2.2 lie adjacent to one another as Group III and IV elements. The final three materials chosen were Hf, Y and Lu. Their preparation and characterization are discussed below.

2.5.2 Metallic Vapor Deposition Concerns

We investigated the quality of the two metal deposition processes used to create the metallic layers studied in Chapters 3 and 4. Each metal individually coated a 5×8 mm^2 fused silica substrate (1 mm thickness) with a ~ 1 μm thick metal layer, with the opposite face of the substrate coated with a painted graphite layer as described in Sec. 2.4.1. A concern arose that dealt with whether or not the deposited metal had the same properties as bulk metal. The metal layers studied in our experiment were yttrium (Y), lutetium (Lu) and hafnium (Hf) (see Sec. 2.5.1 for the selection criteria). The lutetium was patterned onto the fused silica substrate with a vapor deposition technique in which the metal was oven-heated to temperatures hot enough for the metal to sublimate to a vaporous state. The hot metallic vapor then condensed onto the glass substrate, which thus created an appreciable lutetium layer. The yttrium metal was patterned onto the glass substrate with a electron-beam providing the required energy to vaporize an yttrium target, allowing it to condense onto the substrate, while the hafnium substrate was produced by sputtering. It was unclear whether these techniques produce a homogeneous crystalline metallic structure on the substrate or if they produce a heterogeneous metallic layer in which the vapor condenses into tiny metallic clusters

on the surface.

We measured the resistivity of the metal layers to test the properties of deposited metal. If the resistivity measurements disagreed significantly with the known value for the bulk metal resistivity, we would know the metal sample was not homogeneous and could not be used to perform a quantitative test of an atom-surface-interaction theory.

The resistivity of a hafnium sample (prepared in an identical fashion to the piece in our UHV vacuum chamber) was deduced by performing a four-wire measurement with the device shown in Fig. 2.23(c). The device was machined to small tolerances ($\sim 2 \times 4$ inches) in order to have it fit into a small vacuum chamber. The vacuum chamber was necessary in this off-line experiment in order to be certain that the resistivity of the sample was not the resistivity of an oxide layer, which might accumulate on the sample when heated in atmosphere.

The device was constructed with two copper-beryllium electrodes providing a small current to be passed through the material. The combination of the material resistance and the reference current provides a measurable voltage proportional to the material resistance. By measuring the applied current and the resultant voltage, one may deduce the material's resistance. The voltage V between these two points should be proportional to the distance between the two probes L and the reference current I, and will be inversely proportional to the cross-sectional area of the sample (thickness$\times$width). Putting this all together the resistivity ρ looks like,

$$\rho = \frac{V}{I}\frac{t}{L}\frac{w}{}. \tag{2.20}$$

where t and w are the material thickness and width of the sample, respectively, while V is the voltage measured between the probe wires.

Fig. 2.23(a) shows the results of a test experiment with a piece of aluminum foil. The resistivity measurement for the foil agrees very well with the known resistivity of bulk aluminum (solid black line). The temperature of the device is also heated

while making resistivity measurements, with a well-placed thermocouple providing a measurement of the temperature. The data at hotter temperatures also agree very well with the known temperature dependence of the resistivity for aluminum, giving us confidence that the resistivity measurements are quite accurate.

Fig. 2.23(b), however, shows the same measurement performed with the metallic hafnium layer, showing a gross disagreement with the known value of the resistivity of hafnium (solid black line). The thickness of the hafnium layer was measured with an atomic force microscope (AFM) and was found to be ~ 1.4 μm thick. This thickness corresponds to thousands of monolayers of hafnium, which is thick enough to constitute a bulk metal layer. The disagreement with the known resistivity values suggests that, indeed, the metallic hafnium layer is quite heterogeneous and was most likely formed irregularly during the deposition process. The uncertainty in the material composition of the metal layers led to our departure from making a Casimir-Polder force measurement with deposited metals.

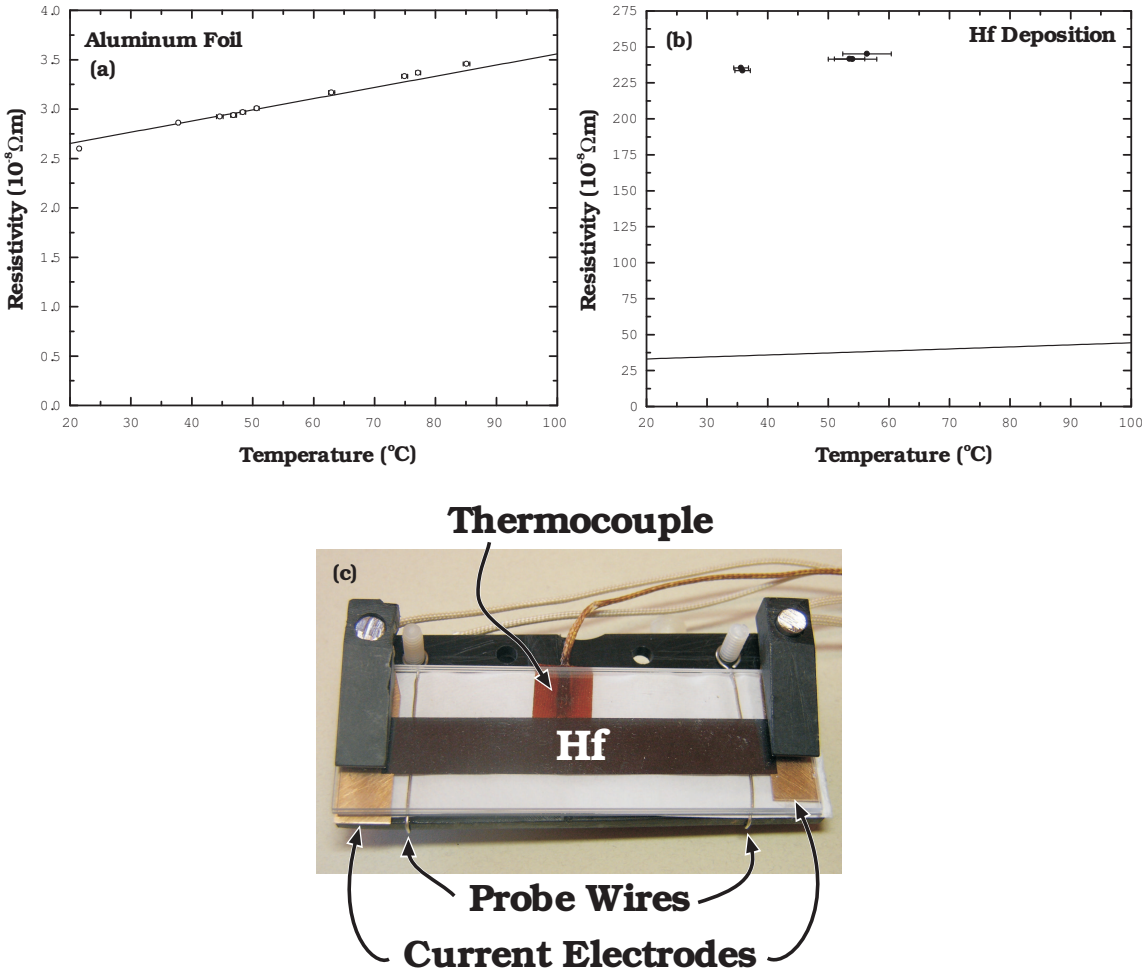

Figure 2.23: Resistivity measurements of Hf and Al. This figure shows the 4-wire resistivity measurements made with the pictured apparatus. This apparatus was constructed to be operated in a vacuum chamber whose temperature could be varied with heater tape and measured with a well-placed thermocouple. Electrical feedthroughs were used to provide current through the sample and to measure the voltage between the probe wires. Graph (a) shows the results of the experiment performed with aluminum foil. The agreement between the measured resistivity and the known value is very good and provides confidence in the performance of the apparatus. The data in (b) shows the result of the experiment performed with a deposited hafnium layer (1.4 μm thick). The disagreement between the measured value and the known value for this metal led us to conclude that the deposited hafnium does not behave like bulk hafnium.

Chapter 3

Temperature-Dependent Casimir-Polder Force Measurement [16]

In this chapter of the thesis we report on the first measurement of a temperature dependence of the Casimir-Polder force. This measurement was obtained by positioning a nearly pure ^{87}Rb Bose-Einstein condensate a few microns from a dielectric substrate and exciting its dipole oscillation. Changes in the collective oscillation frequency of the magnetically trapped atoms result from spatial variations in the surface-atom force. In our experiment, the dielectric substrate is heated up to 605 K, while the surrounding environment is kept near room temperature (310 K). The effect of the Casimir-Polder force is measured to be nearly 3 times larger for a 605 K substrate than for a room-temperature substrate, showing a clear temperature dependence in agreement with theory.

3.1 Introduction

The Casimir force and its molecular cousin, the van der Waals force, are not only fascinating scientifically but also important technologically, for example in atomic force microscopy and microelectromechanical (MEMS) systems. Like the tension in *a* rubber band, the Casimir force is a conservative force arising from microscopic fluctuations. The Casimir force is also the dominant background effect confounding attempts [6, 7, 8, 9] to set improved limits on exotic forces at the 10^{-8} m to 10^{-5} m length scale; progress towards a deeper understanding is valuable in that context. Typically one uses "Casimir" [17] to refer to the force between two bulk objects, such as metallic spheres

or dielectric plates, and "Casimir-Polder" (CP) [1] to describe the force between a bulk object and a gas-phase atom. The underlying physics [18] is largely the same, however, and, particularly in the limit of separations exceeding one micron, it can be more convenient to study the latter system due to ease in rejecting systematic errors such as electrostatic patch potentials [19, 20].

The Casimir force arises from fluctuations of the electromagnetic field and is usually thought of as being purely quantum mechanical. However, at nonzero temperatures, the fluctuations also have a thermal contribution, which was investigated by Lifshitz [4]. Precise theoretical modelling of Casimir forces takes into account effects such as surface roughness, finite conductivity, substrate geometry, and nonzero temperature, but the latter term has never before been unambiguously observed experimentally (see [5] and references therein). In earlier Casimir [6, 21, 22, 23, 24, 25] and Casimir-Polder [20, 26, 27, 28, 29, 30, 31, 32] experiments, thermal effects were predicted to be on the order of experimental uncertainties or less because (a) the temperature of the apparatus could not be varied over a large range and (b) the experiments worked over small separations compared to the wavelength of thermal radiation, where thermal corrections are small.

To review the main regimes in surface-atom forces: For a surface-atom separation x much less than the wavelength of the dominant resonances in the atom and substrate, the potential U scales as $1/x^3$ (van der Waals-London regime). At longer distances, retardation effects cause a crossover to $U \sim 1/x^4$ (Casimir-Polder). At still longer distances when x is comparable to the blackbody peak at temperature T, temperature effects become important, and in thermal equilibrium ($T = T_S = T_E$, as defined below), there is a second crossover, back to $U \sim T/x^3$ (Lifshitz).

3.2 Non-Equilibrium Thermal Casimir-Polder Force

In this chapter of the thesis, I describe the first measurement of a temperature dependence of the Casimir-Polder force, indeed the first conclusive temperature dependence of any Casimir-like system. A key feature of this work is that the apparatus temperature is spatially nonuniform. This allows for an experimental confirmation of an appealing theoretical insight: The thermal electromagnetic-field fluctuations that drive the CP force can be separated into two categories — those that undergo internal and those that undergo external reflection at the surface (see Fig. 3.1). These two categories of fluctuations contribute to the total force with opposite sign; in thermal equilibrium, they very nearly cancel, masking the underlying scale of thermal effects. Working outside thermal equilibrium, we observe thermal contributions to the CP force that are 3 times as large as the zero-temperature force.

Recent theoretical work [11] has shown that thermal corrections to the Casimir-Polder force are separable into those arising from thermal fluctuations within the substrate at temperature T_S [33] and those arising from radiation impinging from presumed distant walls at an environmental temperature T_E. At $T_S \neq 0$, electromagnetic fluctuations from within the surface have an evanescent component that extends into the vacuum with maximum intensity at the surface, giving rise to an attractive AC Stark potential (Fig. 3.1). External radiation at T_E, impinging at different angles, reflects from the substrate surface, giving rise to a field distribution whose intensity falls smoothly to a minimum at the substrate surface. The resulting Stark shift from the external radiation then pulls the atom *away* from the surface, contributing a repulsive term to the potential.[1]

Antezza *et al.* [11] recently predicted that the nonequilibrium contribution to the CP potential asymptotically scales as $U_{NEQ} \sim (T_S^2 - T_E^2)/x^2$ in the long-range limit. As

[1] Here we assume that the atom does not absorb radiation (T_E and T_S are small with respect to atomic resonances).

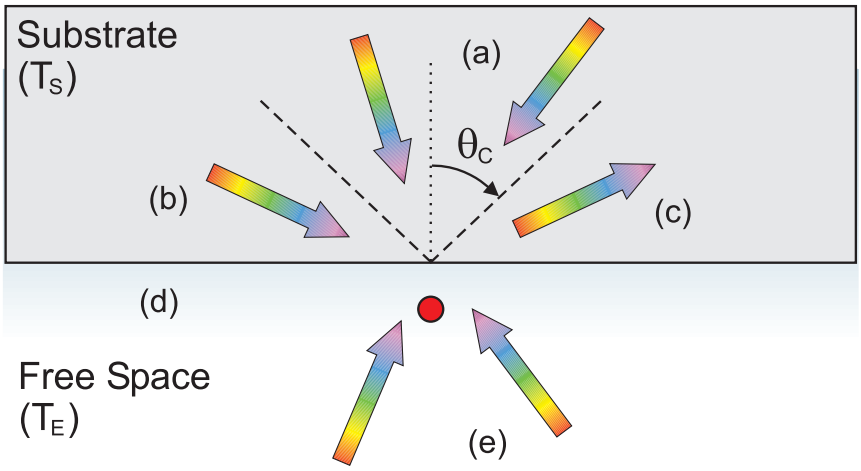

Figure 3.1: Radiation. Cartoon drawing of thermal fluctuations near the surface of a dielectric substrate (shaded region). (a) Internal radiation striking the surface at angles less than the critical angle θ_C does not contribute to the Casimir-Polder force. However, internal radiation impingent at larger angles (b) undergoes total internal reflection (c) and contributes to an overall AC Stark shift by creating evanescent waves in free space (d). Surrounding the atom (red circle) is radiation from the environment (e) which contributes to the CP force by creating standing waves at the surface. The force does not arise from radiation pressure but rather from gradients in intensity. The surface-atom force becomes more attractive for $T_S > T_E$ and more repulsive for $T_S < T_E$.

they describe in their paper, the total nonequilibrium thermal Casimir-Polder force can be written as a sum of contributions from vacuum fluctuations and thermal fluctuations of the electromagnetic field,

$$F_{tot}^{neq}(T_S, T_E, x) = F_{vac}(x) + F_{thl}^{neq}(T_S, T_E, x). \tag{3.1}$$

We can also write the nonequilibrium force above as a sum of the *equilibrium* thermal CP force, at temperature T, and an extra term that one obtains by allowing the substrate and environment to be at different temperatures. The above equation may then be written as,

$$F_{tot}^{neq}(T_S, T_E, x) = F_{thl}^{eq}(T, x) + F^{extra}(T_S, T_E, x). \tag{3.2}$$

The temperature T in the above equation is yet to be defined as T_S or T_E.

As pointed out by Henkel *et al.* [33] thermal fluctuations from the surface and fluctuations from the environment are incoherent with respect to one another. Therefore, we may write the contribution to the force from thermal fluctuations as an incoherent addition of the two effects,

$$F_{thl}^{neq}(T_S, T_E, x) = F_{thl}^{neq}(T_S, 0, x) + F_{thl}^{neq}(0, T_E, x). \tag{3.3}$$

The first term above describes the contribution to the force from thermal radiation from the surface with no radiation from the environment, while the second term describes only thermal radiation from the environment and no radiation from the surface.

*R*ewriting the thermal equilibrium contribution (from Eq. 3.2) as the sum of two nonequilibrium forces with temperature T gives us,

$$F_{thl}^{eq}(T, x) = F_{thl}^{neq}(T, 0, x) + F_{thl}^{neq}(0, T, x). \tag{3.4}$$

If we combine the above four equations and cancel terms we come to an important relationship,

$$F_{thl}^{neq}(T_S, 0, x) + F_{thl}^{neq}(0, T_E, x) = F_{thl}^{neq}(T, 0, x) + F_{thl}^{neq}(0, T, x) + F^{extra}(T_S, T_E, x). \tag{3.5}$$

If we define T to be equal to the surface temperature T_S, we may cancel similar terms in Eq. 3.5 to arrive at the equation for the extra force,

$$F^{extra}(T_S, T_E, x) = F^{neq}_{thl}(0, T_E, x) - F^{neq}_{thl}(0, T_S, x), \tag{3.6}$$

which describes the extra force as being a difference between the force from an environment temperature of T_E and the force from an environment temperature of T_S. This expression for the extra force is valid and may be used for calculational purposes, but turns out to be very difficult to express analytically and quite hard to compute numerically, according to Antezza *et al.* [11].

If instead we define the temperature T to be equal to the *environment* temperature, we may arrive at a similar form for the extra force which is much easier to work with. This expression for the extra force, first obtained by Antezza *et al.*, can be written as,

$$F^{extra}(T_S, T_E, x) = F^{neq}_{thl}(T_S, 0, x) - F^{neq}_{thl}(T_E, 0, x). \tag{3.7}$$

This expression describes the additional force seen by the atoms which comes about by maintaining a temperature difference between the environment and the surface. This representation requires only one expression $F^{neq}_{thl}(T, 0, x)$ to describe the extra force on the atoms,

$$F^{neq}_{thl}(T, 0, x) = -\frac{\hbar\alpha_o}{c^4}\int_0^\infty d\omega \frac{\omega^4}{e^{\hbar\omega/kT} - 1}\int_1^\infty f(q, x, \omega, \epsilon(\omega)). \tag{3.8}$$

Here k is the Boltzmann constant, α_o is the static polarizability of the atom and $f(q, x, \omega, \epsilon(\omega))$ is a complicated function which takes into account the interaction of light with a dielectric material, $\epsilon(\omega)$, for all radiation wavelengths (shown in Fig. 3.2). The potential energy of this extra force scales like $U_{NEQ} \sim (T_S^2 - T_E^2)/x^2$, which tends to zero when $T_S = T_E$.

This novel scaling dependence dominates at long range. One can thus temperature-tune the magnitude of this long-range force and, in principle, even change the sign of

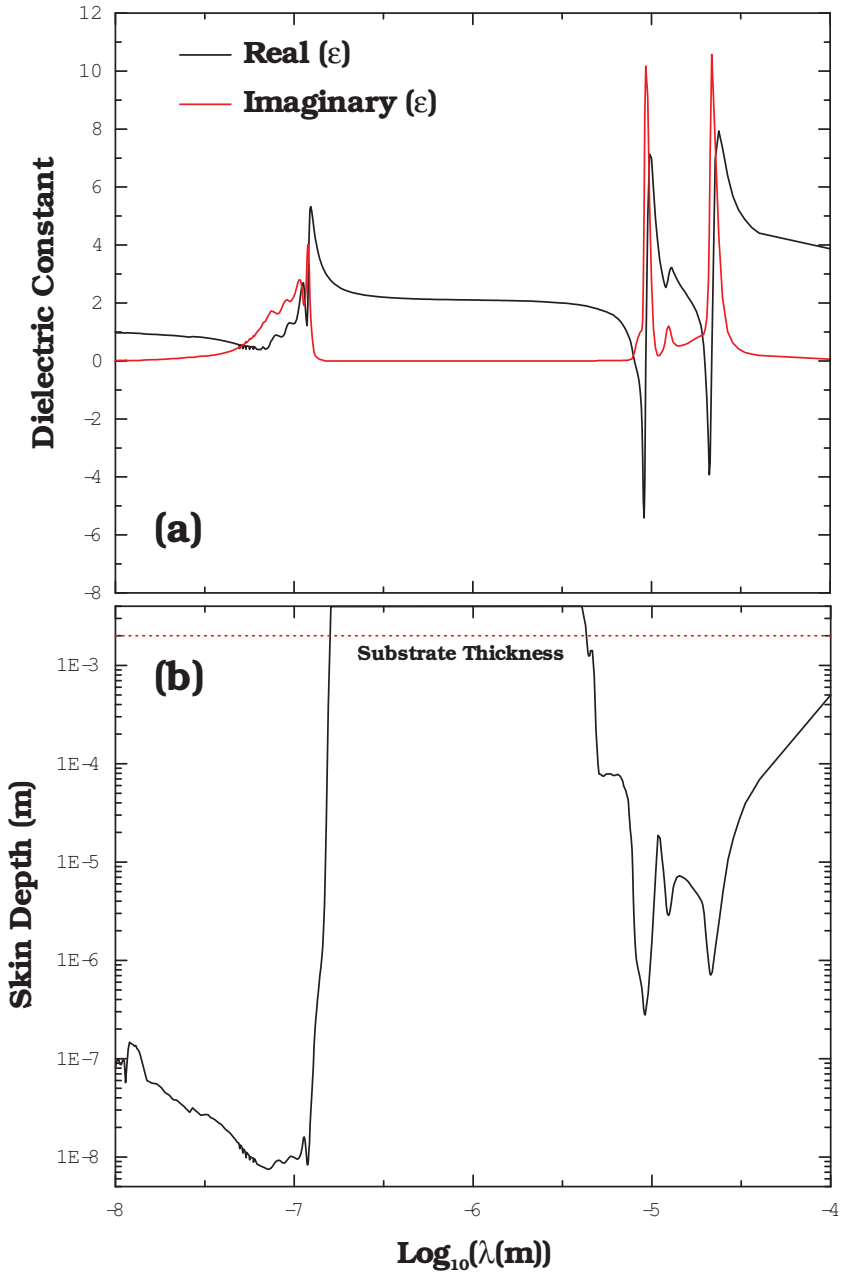

Figure 3.2: Optical properties of fused silica. This figure (a) shows the real and imaginary parts of the dielectric constant of fused silica for a range of radiation wavelengths. The skin depth of fused silica is plotted in (b), where the dashed red line indicates the thickness of the material. This shows that the skin depth of fused silica is much smaller than its size in the spectral range of thermal radiation ($\lambda > 4\mu$m). This data was obtained from H. R. Phillip [34].

the overall force. Fig. 3.3 shows the predicted fractional frequency shift γ_x (Eq. 3.9 below) for a cool surface - warm environment scenario in which the substrate is cooled to liquid nitrogen temperatures ($\sim$80 K), while the environment is heated to an experimentally achievable temperature of 600 K. Positive frequency shifts correspond to attractive forces, while negative shifts correspond to repulsive forces. The graph in (b) shows a repulsive force (inset) for $x > 4\mu$m, which results in a negative frequency shift for $x > 5.5\mu$m (see Antezza *et al.* for details [35]). This force, however, is not repulsive for all x, and indeed becomes attractive nearer to the surface, as seen in (a).

The interaction of the atom with a dielectric material becomes very complicated for atom-surface separations on the order of 0-2 μm. Fig. 3.4(a) and (b) show the spectral contribution to the nonequilibrium force for atom-surface separations of 1 μm and 15 μm and for radiation wavelengths λ which range from 1-500 μm. One can see that the force on atoms 1 μm from the surface (a) comes largely from the influence of material resonances (see the imaginary part of the dielectric constant in Fig. 3.2(a)), while the total force on atoms 15 μm from the surface (b) comes largely from the dc component of the dielectric constant. The spectral contribution to the force in (b) looks fairly smooth and only has a small contribution from material resonances. If we approximate the functional form of the dielectric constant $\epsilon(\omega)$ as the dc dielectric constant $\epsilon(0)$, we find a very good agreement between the actual total force and the force calculated from the approximation. Fig. 3.5(a) shows an agreement which becomes no worse than six percent for atom-surface distances larger than 0.5 μm. The temperature used in this calculation were T_E=300 K and T_S=600 K.

The agreement between the actual force and the force computed with the dc dielectric constant also allows us to look at the dependence of the nonequilibrium force on the dc dielectric constant $\epsilon(0)$. Antezza, *et al.* describe the dependence of the nonequilibrium force on the dielectric constant as $(\epsilon(0)+1)/\sqrt{\epsilon(0)-1}$ (Eq.(12) in Ref. [11]). This scaling of the force with dielectric constant does not accurately predict the behav-

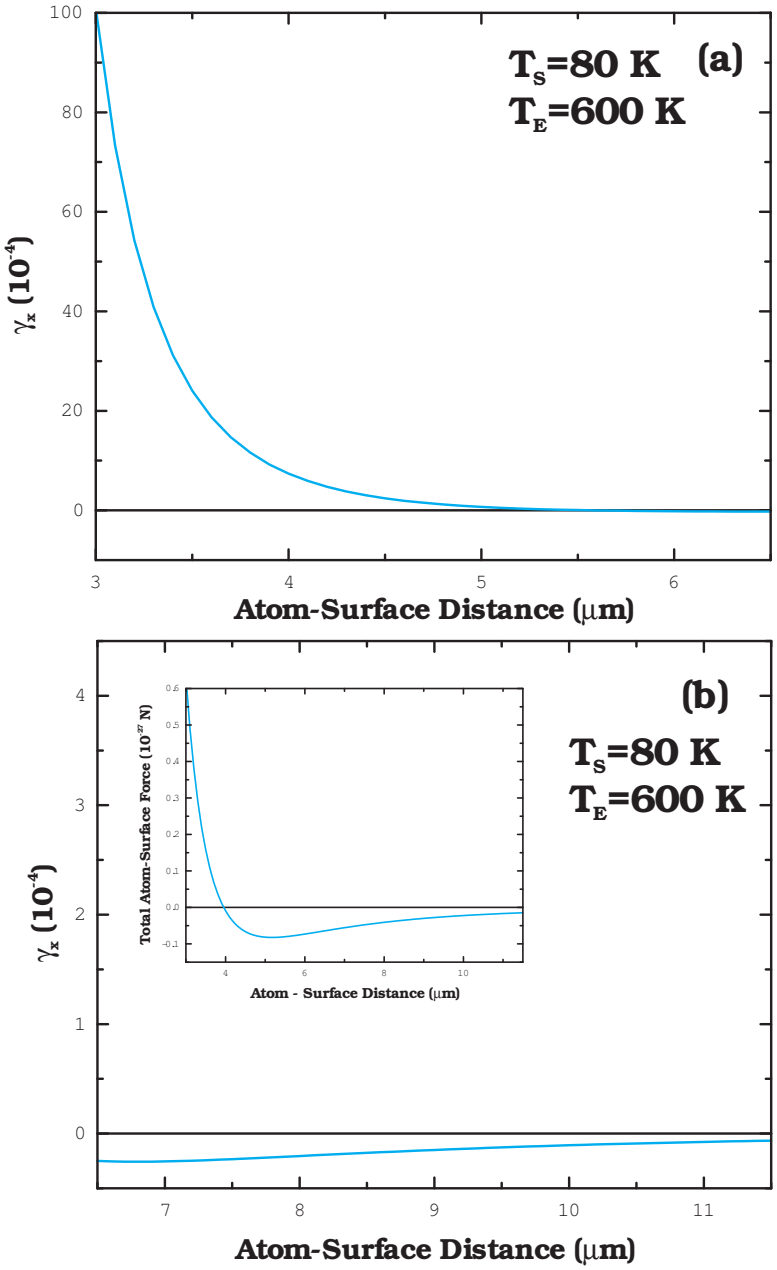

Figure 3.3: Creating a repulsive Casimir-Polder force. This figure shows the temperature tuning of the Casimir-Polder force predicted by Antezza *et al.* [35]. A repulsive force may be achieved for atoms which are further than 4 μm from the surface (see inset in (b)). This may be accomplished by cooling the substrate temperature to liquid nitrogen temperatures ($\sim$80 K), while keeping the environment temperature at an experimentally achievable value of 600 K. The graph in (a) shows the fractional frequency shift γ_x for small atom-surface distances, in which an attractive force is seen, while the graph in (b) shows a negative frequency shift (indicating a repulsive force). This frequency shift measurement is achievable with our experimental setup.

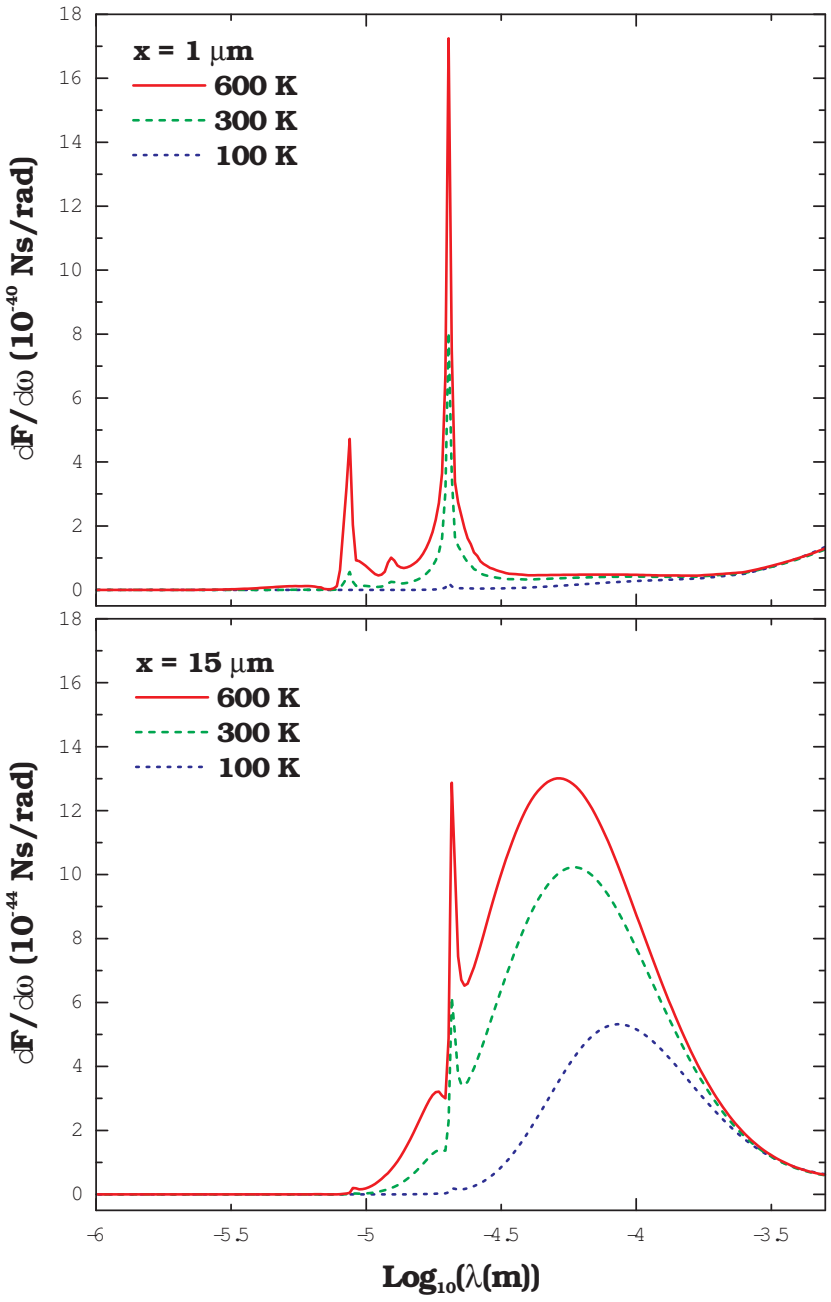

Figure 3.4: Spectral contribution to the Casimir-Polder force as seen by a rubidium atom in close proximity to a fused silica substrate. These figures show the contribution to the Casimir-Polder force from radiation of wavelength λ for (a) an atom 1 μm from the surface and (b) an atom 15 μm from the surface. Graph (a) indicates that the forces on the atoms are largely due to the thermal radiation's interaction with inherent material resonances (sharp peaks). However, far from the surface the forces on the atoms are primarily due to the interaction of the radiation with the dc component of the material's dielectric constant. This give the spectral contribution to the force a smoother shape.

ior of the force in the limit of a metal surface ($\epsilon(0) = \infty$, i.e. no evanescent waves) or in the limit of no surface ($\epsilon(0) = 1$, i.e. no surface). Fig. 3.5 shows the strength of the extra force on atoms 1 μm from a 300 K surface, when the environment radiation is kept at 0 K. One can see the correct limiting behavior of the force for the limits discussed above.

3.2.1 Experiment

We observe the temperature dependence of the Casimir-Polder force between a rubidium atom and a dielectric substrate by measuring the collective oscillation frequency of the mechanical dipole mode of a Bose-Einstein condensate (BEC) near enough to a dielectric substrate for the CP force to measurably distort the trapping potential. This distortion of the trap results in changes to the oscillation frequency proportional to the gradient of the force:

$$\gamma_x \equiv \frac{\omega_o - \omega_x}{\omega_o} \simeq \frac{1}{2m\omega_o^2} \langle \partial_x F_{CP} \rangle, \tag{3.9}$$

where m is the mass of the ^{87}Rb atom, and γ_x is defined as the fractional frequency difference between the unperturbed trap frequency ω_o and ω_x, the trap frequency perturbed by the CP force F_{CP}.

The use of a BEC in this work is not conceptually central. The force between the substrate and the condensate is the simple sum of the force on the individual atoms of the condensate. For our purpose, the condensate represents a spatially compact collection of a relatively large number of atoms whose well-characterized Thomas-Fermi density profile facilitates the spatial averaging and the inclusion of nonlinear effects in the oscillations, necessary for the quantitative comparison between theory and experiment [20, 35].

The data in Fig. 3.6(a) shows the method of controllably placing the BEC into a dipole oscillation (see Ref. [10] for more details). An external magnetic field is applied,

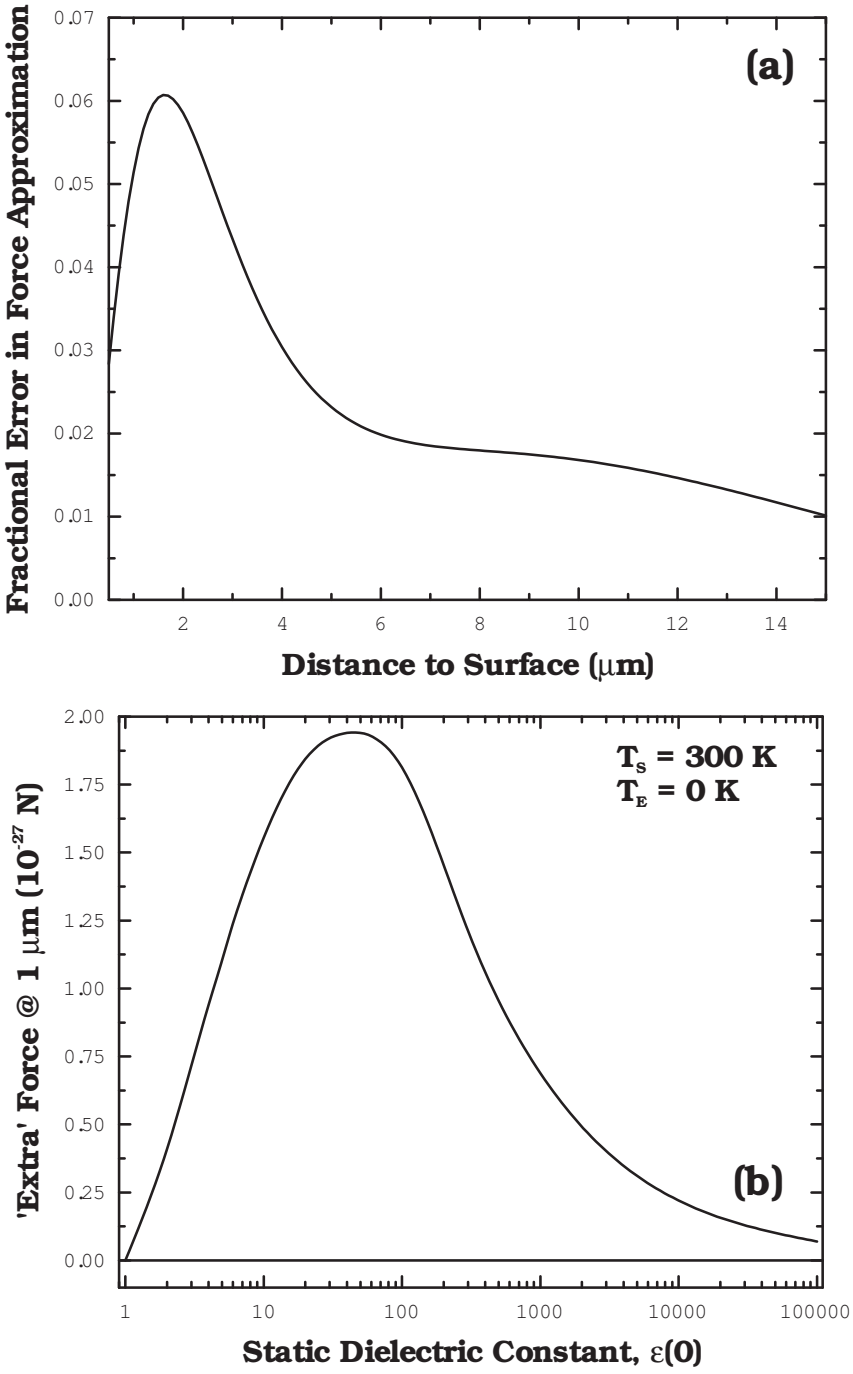

Figure 3.5: Effect of the dielectric constant. Graph (a) shows the fractional error in the nonequilibrium thermal Casimir-Polder force having approximated the functional form of the dielectric constant of the material $\epsilon(\omega)$ as a true constant $\epsilon(0)$. This approximation is no worse than six percent for distances greater than 0.5 μm. Graph (b) shows the effect of varying the dc dielectric constant. The contribution to the force on the atoms from the substrate tends to zero for a dielectric constant of 1 (i.e. no surface present) and also for a dielectric constant of ∞ (in which case there are no evanescent waves present).

which effectively shakes the equilibrium position of the BEC,

$$x_0(t) \propto e^{-(t-t_0)^2/\sigma^2} \cos(\omega_o t + \phi). \tag{3.10}$$

The resultant displacement of the atoms δx is described as,

$$\delta x(t) = \frac{A_x}{2}(Erf(\frac{t-t_0}{\sigma}) + 1)\cos(\omega_o t + \phi). \tag{3.11}$$

where A_x is the amplitude of the resulting oscillation. It is essential in this experiment that the amplitude of this oscillation be repeatable and very carefully calibrated in order to make precise measurements of atom-surface forces.

Fig. 3.6(b) shows a to-scale illustration of an oscillating BEC (dark-gray, inverted parabola) at its closest trap-center-to-surface position (typically $\sim$7 μm). The illustration shows that careful calibration, not only of the amplitude of the oscillation, but also of the BEC size (and therefore BEC number fraction) must be taken into accou$n$t for measurements of forces which are very dependent on atom-surface separations, like the Casimir-Polder force. The light-gray inverted parabolas show the oscillating BEC at its classical turning points. A BEC placed at 7 μm may have constituent atoms which reach as close as 1.8 μm to the surface.

Experimental details, surface-atom measurement and calibration techniques, along with a detailed discussion of measurements of stray electric and magnetic fields appear in [15, 19, 20]. In brief, the experiment consists of 2.5×10^5 ^{87}Rb atoms Bose-condensed (condensate purity > 0.8) in the $|F = 1, m_F = -1\rangle$ ground state. The condensate is produced $\sim$1.2 mm below a dielectric substrate in a Ioffe-Pritchard-style magnetic trap (trap frequencies of 229 Hz and 6.4 Hz in the radial and axial directions, respectively), resulting in respective Thomas-Fermi radii of 2.69 μm and 97.1 μm.

The dielectric substrate studied consists of uv-grade fused silica $\sim 2\times8\times5$ mm^3 in size (x, y, z directions, respectively) sitting atop a monolithic pyrex glass holder inside a pyrex glass cell which composes the vacuum chamber (Fig. 3.7). The top surface

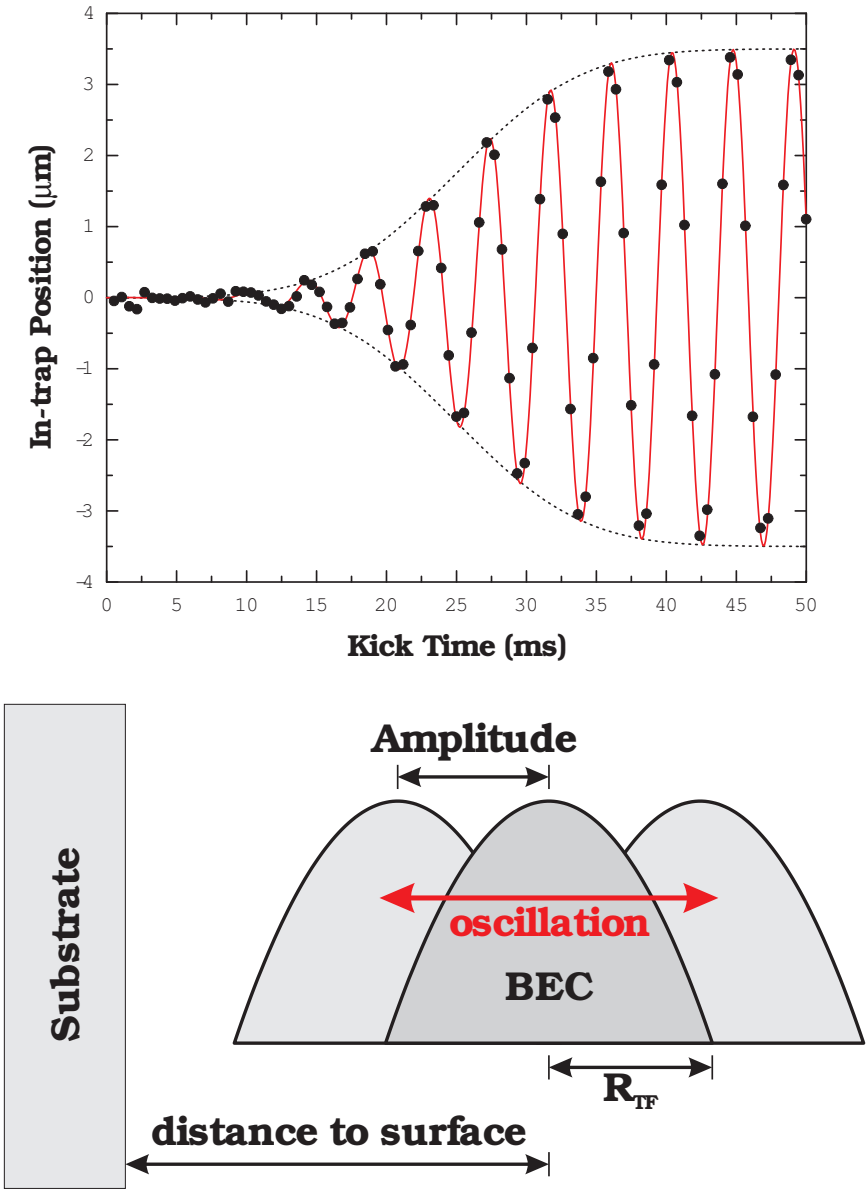

Figure 3.6: Finite cloud size and oscillation amplitude. The data in the graph show the atoms being carefully placed into a dipole oscillation by an external magnetic field which oscillates with a Gaussian time envelope (Eq. 3.11). The illustration below shows a to-scale drawing of the finite size (R_{TF}) of the BEC along with its oscillation amplitude. The dark gray cloud shows the position of the BEC at rest, while the light-gray clouds show the BEC at its classical turning points. A BEC placed 7 μm from the surface will have constituent atoms which get as close as 1.8 μm.

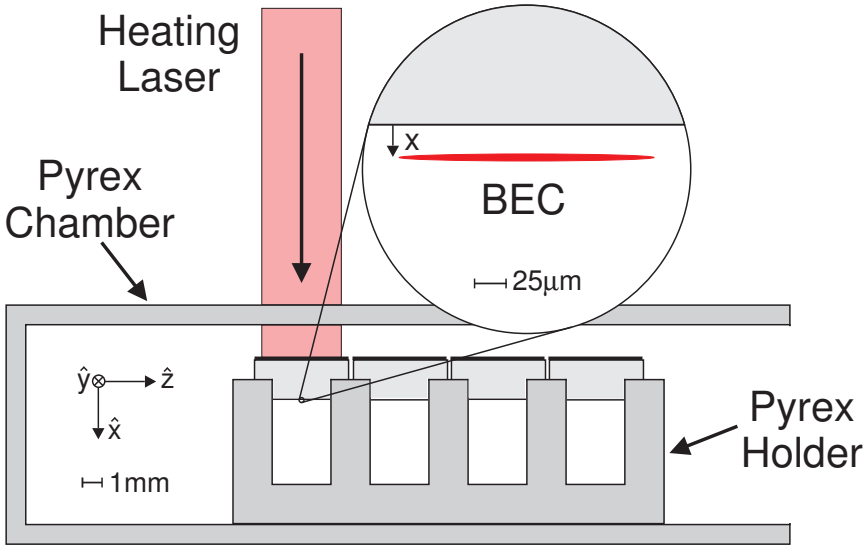

Figure 3.7: Apparatus. Side view of the apparatus. Shown is a scale drawing of the fused silica substrate (left-most of the four substrates) with a top layer of graphite. The graphite absorbs the light from the laser, heating the substrate. The pyrex holder is isolated enough from the substrate to allow a hot substrate – cool environment scenario. The enlargement in the inset shows the BEC at a distance x from the surface.

($-\hat{x}$ face) of the substrate is painted with a $\sim$100 μm thick opaque layer of graphite and treated in a high-temperature oven prior to placement in the vacuum chamber (see Sec. 2.4.1 for details). The observed lifetime of the BEC places a strong, robust, upper bound on the total pressure of residual gas just below the substrate surface of $\sim 3 \times 10^{-11}$ torr, even at $T_S = 605$ K. A more detailed calculation of surface adsorbate effects appears in Sec. 3.4.

The fused silica substrate was heated by shining $\sim$1 W of laser light (860 nm) on the graphite layer. The rough texture of the pyrex holder creates near point contacts with the substrate corners, providing good thermal isolation between the holder and the substrate. This technique allows us to vary the temperature of the substrate while maintaining near room temperature vacuum chamber walls and only slightly elevated holder temperatures.

The temperature of the fused-silica substrate as a function of the heating laser power was determined in an offline calibration apparatus, constructed to be a near-identical version of the main vacuum chamber, except with improved optical access for a temperature probe laser (see Sec. 2.4.2 and Sec. 2.4.3 for more details). The probe laser is coherently split between two arms of a Michelson interferometer (Fig. 2.19). The resulting fringe shifts are proportional to changes in substrate temperature. A finite-element numerical model of the thermal system agreed with our measurements and contributed to our confidence that the temperature of the substrate and the environment were understood. Residual systematic uncertainties in temperature are reflected in the error bars in Fig. 3.8(b).

The experiment, described in detail in [20], begins with an adiabatic displacement of the atom cloud to a distance x from the bottom surface ($+\hat{x}$ face) of the substrate via the addition of a vertical bias magnetic field. The cloud is then resonantly driven into a mechanical dipole oscillation by an oscillatory magnetic field,[2] shown in Fig. 3.6(a).

[2] The amplitude of the oscillation is carefully calibrated to be 2.50(2) μm in the $\hat{x}$ direction.

After a period of free oscillation the relative position of the cloud is determined by destructive imaging after ∼5 ms of anti-trapped expansion. This process is repeated for various times in the free oscillation. The center-of-mass position is recorded at short times to determine the initial phase of the oscillation and at later times (∼1s) to precisely determine the oscillation frequency. Data is taken consecutively alternating the trap center position between a distance x, close to the surface, and a normalizing distance $x_o = 15$ μm. The distance x_o is sufficiently far from the substrate to avoid surface perturbations, yet close enough to provide a local oscillator ω_o with which the data taken at x can be compared. Data sets are then taken at a number of surface-atom positions (between 7–11 μm) and for various substrate temperatures (310, 479 and 605 K, taken in random order, several times, and averaged in Fig. 3.8).

The results in Fig. 3.8(a) show the fractional change in the trap frequency γ_x plotted as a function of the trap center to surface position x. The blue squares show the measured effect of the room-temperature Casimir-Polder force (T_S=310(5) K) on the trap frequency. The increase in the strength of the CP force due to thermal corrections becomes obvious when the substrate is heated to 479(20) K (green circles) and ev*e*n more pronounced when it is at 605(28) K (red triangles). These measurements were all done maintaining a room temperature environment for which the pyrex vacuum chamber walls were measured to be $T_E = 310(5)$ K. The curves in Fig. 3.8(a) represent the theoretical predictions [11] for corresponding substrate-environment temperature scenarios, showing excellent agreement with the measurements.

For statistical clarity in data analysis, the average value of γ_x can be computed for each substrate temperature (using trap center to surface positions 7.0, 7.5, and 8.0 μm only). These values, plotted in Fig. 3.8(b), clearly show a significant increase in the strength of the Casimir-Polder force for hotter substrate temperatures; they also distinguish the nonequilibrium theory (solid) curve from the equilibrium (dash-dotted) curve, for which a much smaller force increase is predicted.

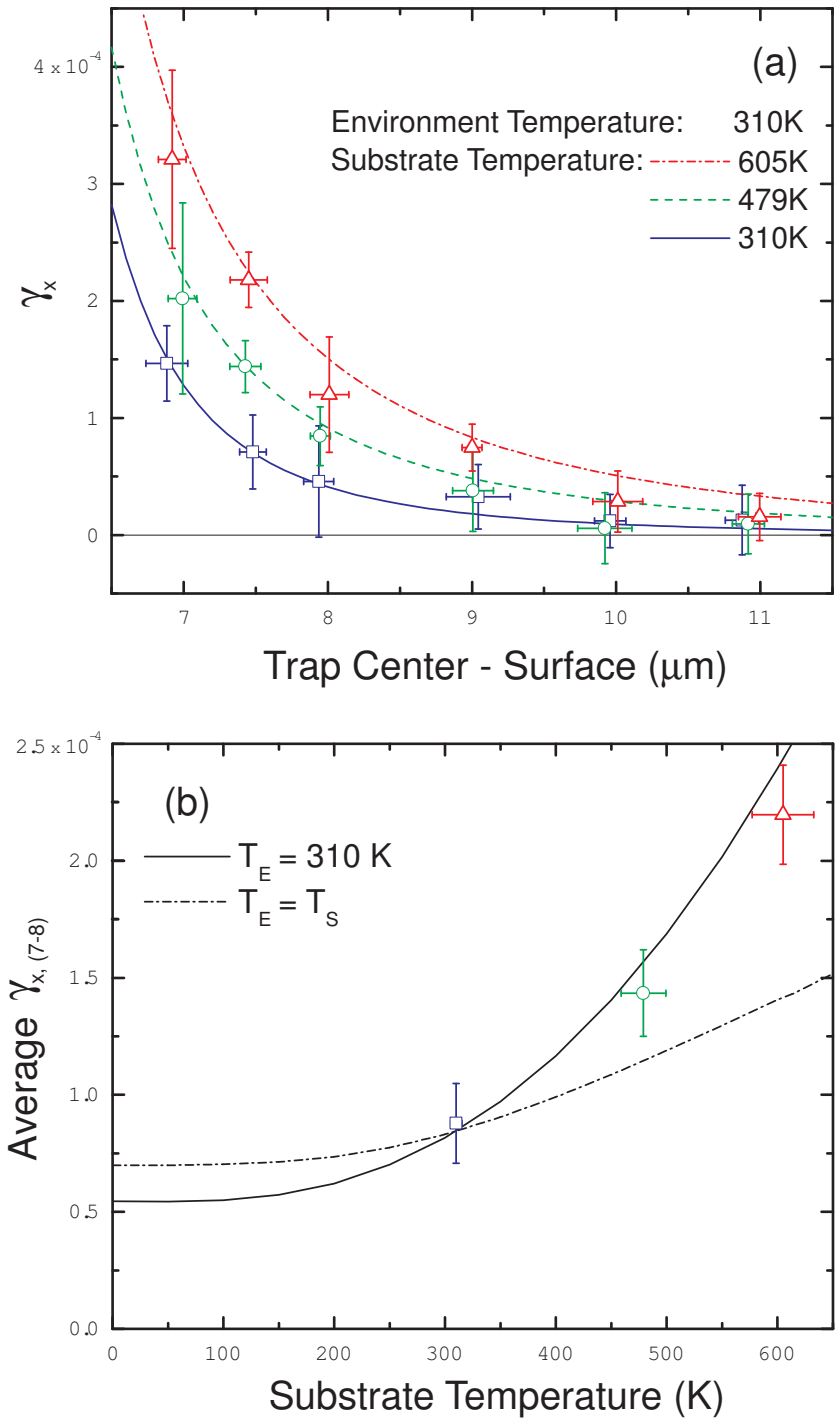

Figure 3.8: Data. (a) Fractional change in the trap frequency due to the Casimir-Polder force. Pictured are three sets of data and accompanying theoretical curves with no adjustable parameters for various substrate temperatures. The blue squares represent data taken with a 310 K substrate; green circles, a 479 K substrate; and red triangles, a 605 K substrate. The environment temperature is maintained at 310 K. The error bars represent the total uncertainty (statistical and systematic) of the measurement. (b) Average values of γ_x from (a) (for trap center to surface positions 7.0, 7.5, and 8.0 μm) plotted versus substrate temperature, demonstrating a clear increase in strength of the CP force for elevated temperatures. The solid theory curve represents the nonequilibrium effect (corresponding 7–8 μm average), while the dash-dot theory curve represents the case of equal temperatures.

3.3 Equilibrium Thermal Casimir-Polder Force

Following the measurements that were made of the nonequilibrium temperature dependence of the Casimir-Polder force, we set out to show that the overall strength of the Casimir-Polder force decreased by raising the temperature of the environment, such that the surface temperature T_S was equal to the environment temperature T_E. An attempt was made to achieve this equilibrium scenario with the addition of resistive heaters placed above and below the science cell (shown in Fig. 2.16). With this setup of the apparatus we were able to achieve an average cell temperature of $\sim 125^o$C over long periods of time. Data was taken in the hopes of discerning a difference between the strength of the CP force in a 'hot' scenario and that in a 'cool' room-temperature scenario. Sec. 2.3 details the issues that were encountered which limited the heating of our science cell to only 395 K.

Fig. 3.9(b) shows raw data of the Casimir-Polder force taken in the equilibrium scenario for an apparatus temperature of 310 K (light-blue circles) and 395 K (red triangles). The averaged data is shown in (a) in which the error bars represent both systematic and statistical errors. The theoretical predictions for both scenarios are shown as solid lines.

One can clearly see a larger force being measured in the 'hot' scenario than that measured in the 'cool' scenario. However, the agreement with theoretical predictions does not seem to match the expected measurement. Fig. 3.10 shows a comparison of this data to the non-equilibrium measurements made earlier (see Fig. 3.8 in Sec. 3.2.1 in which the data points at 7.0, 7.5 and 8.0 μm were averaged and placed in the graph). The data points from Fig. 3.9 are shown by their respective symbols (red triangles for the 395 K scenario and light-blue circles for the 310 K case). The data points clearly show a discrepancy between the measurement and the theoretical predictions. It is clear that one of the following systematic effects is present: either there exist forces which

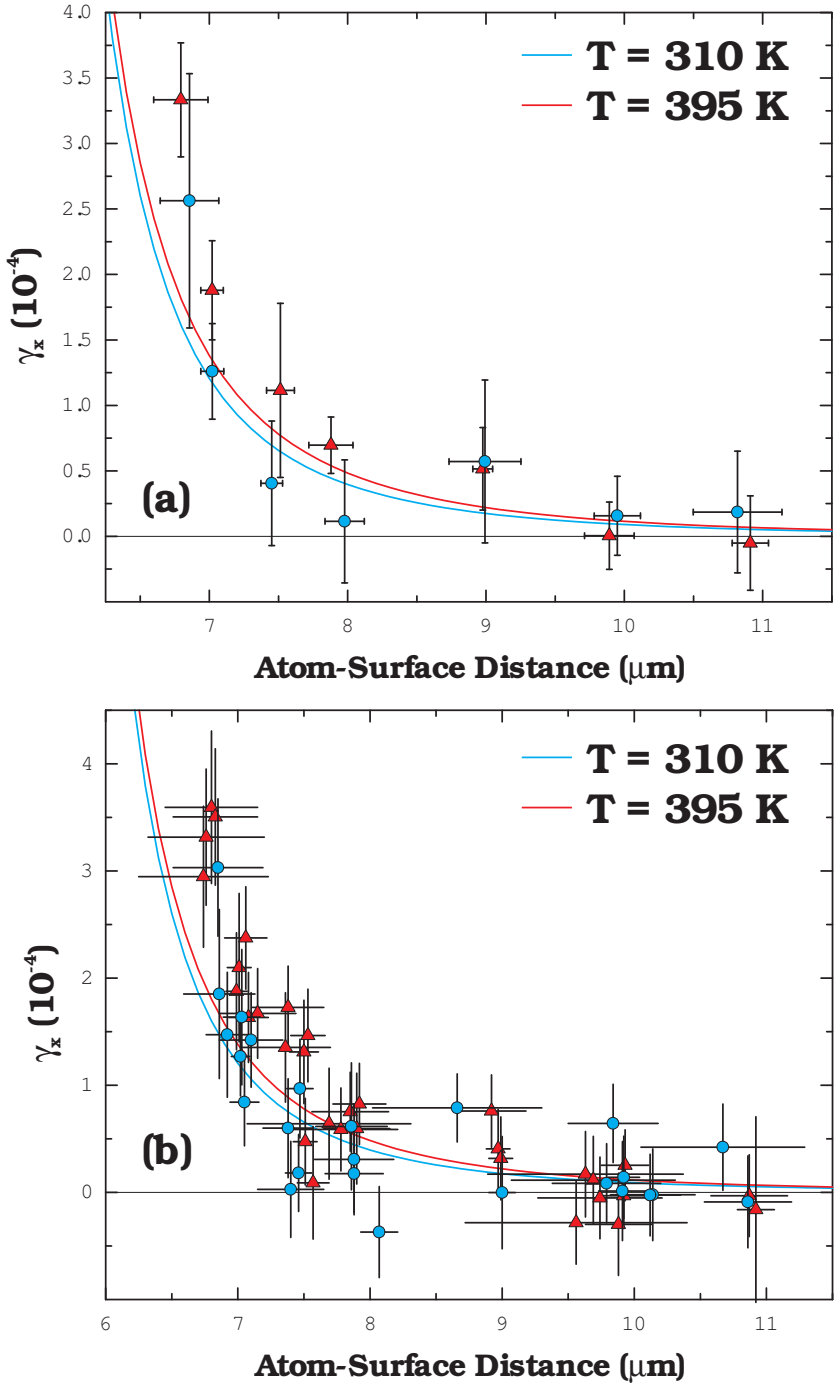

Figure 3.9: Equilibrium data. The data in (a) shows the average of the raw data taken in (b) of Casimir-Polder force measurements with a 310 K apparatus temperature (light-blue circles) and a warmer 395 K apparatus (red triangles). The data show a clear difference between the 'hot' and 'cool' scenarios.

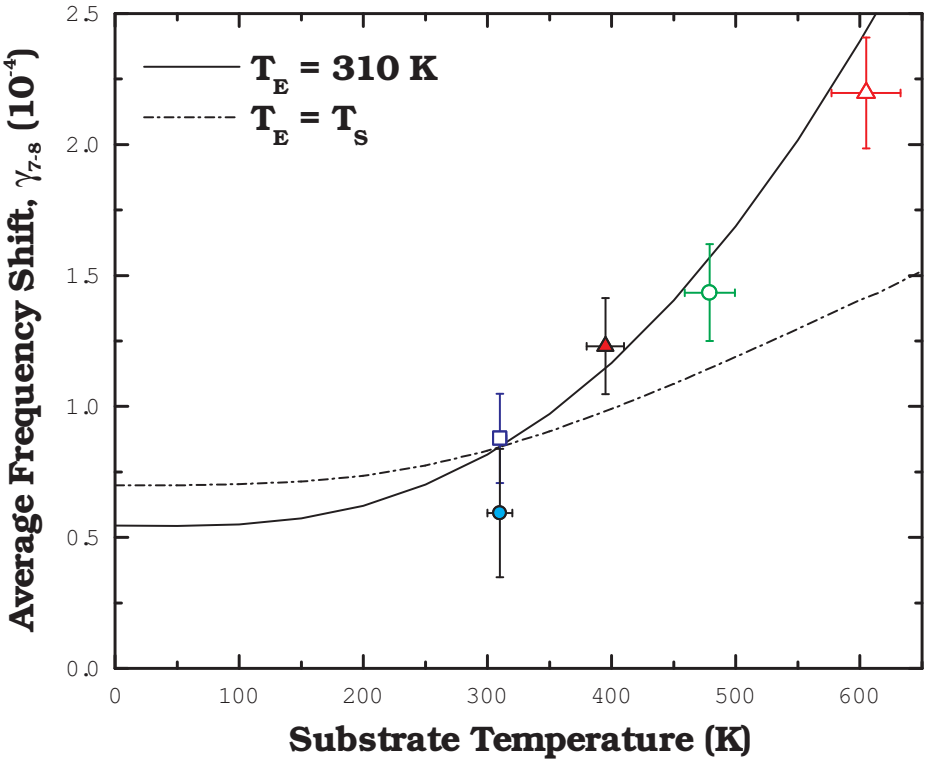

Figure 3.10: Equilibrium - nonequilibrium comparison. The average of the data points in Fig. 3.9 taken at 7.0, 7.5 and 8.0 μm are shown with their respective temperature icons (red triangles for 395 K and light-blue circles for 310 K). The data shows a clear discrepancy between the measured data and the theoretical predictions. The temperature variations of the pyrex chamber were significant enough to describe the discrepancy, but made interpretation of the data difficult.

are acting on the atoms which are unaccounted for (not likely), or we have misjudged the temperature of surface or the temperature of the surrounding environment.

Measurements of the cell temperature were made at several locations around the pyrex cell. Of particular interest was a measurement which indicated that the temperature of the top and bottom of the science cell were significantly hotter than the rest of the pyrex chamber. This measured temperature was roughly 470 K and indicated that the heating elements were not distributing heat evenly enough about our chamber to make an equilibrium measurement. We found that we could keep the pyrex chamber temperature uniform close to room temperature. However, efforts to increase the walls to other temperatures resulted in very patchy heating. We needed to have large areas exposed to room temperature air for optical access and the uneven cooling effect of the convection overwhelmed the limited heat conductivity of pyrex. We considered various chamber redesigns to permit uniform heating of the pyrex chamber, but in the end decided to abandon our efforts to take data with a non-room-temperature chamber and publish the heated-substrate/room-temperature chamber data only.

3.4 Ruling Out Systematic Effects

The killer systematic in Casimir force experiments is often stray electric fields caused by poorly characterized surface properties. We put great care into *in situ* characterizing, for the 605 K and 310 K temperature scenarios in Fig. 3.8, stray magnetic fields and gradients[3] of stray electric fields, using techniques we developed in Ref. [19, 20, 36]. From the magnitude of near-surface dc electric fields, we estimate the surface density of adsorbed alkali atoms to be much less than 1/1000 of a monolayer at all measured temperatures, far too low to change the optical properties of the substrate by the factors of nearly 3 that we see the Casimir-Polder force change by. In addition, the substrate is optically flat at visible wavelengths. Therefore, at the much longer relevant length

[3] A dilute gas' lack of electric monopoles means it feels no force from *uniform* fields.

scales of our experiment any residual surface roughness will be negligible. We can also rule out that the measured increase in strength of the CP force comes from a change in the dielectric constant with increasing temperature, or mechanical effects on the atoms from the heating laser.

One also must consider the quality of the blackbody radiation emitted by the environment. While the pyrex walls of the chamber are transparent at visible and near-infrared wavelengths, at 5–10 μm wavelengths the walls are opaque, with an emissivity > 0.8. Fig. 3.2 shows the dielectric constant of the material for various radiation wavelengths λ. The skin depth of the glass can be calculated from the dielectric constant and is plotted in (b), where the size of the glass substrate is shown as a dashed red line (2 mm). This shows that the material is larger than its skin depth for radiation wavelengths greater than $\sim$4 μm, making the sub*s*trate a good blackbody radiator.

We should also consider the radiation from the surface which is reflected by the pyrex chamber (shown in Fig. 3.11). The radiation from the fused silica substrate (large green arrows in the illustration) looks very much like the radiation from a perfect blackbody emitter (compare the dashed green line with the gray background). This radiation then strikes the bottom of our pyrex chamber and is reflected back towards the bottom face of the substrate (small purple arrows). The amount of radiation that reflects back is negligible compared with the radiation coming from the surface. Compare the area under the solid purple line in the graph with the area under the dashed green line. The solid purple line in this figure is actually an upper limit of the power reflected back towards the atoms. Ideally one would compute the reflected spectral irradiance from a pyrex surface instead of that from a fused silica surface, which is depicted by the solid purple line. The material properties of pyrex, however, are not well documented for a large range of wavelengths. The peak of the 10 μm radiation which is reflected from pyrex would be significantly less than that reflected from fused silica. Luckily this reflected power is also low, which makes systematic effects from these reflections

Item	Cold 310 K	Warm 479 K	Hot 605 K
Thomas-Fermi Radius: $\hat{x}$ (μm)	2.64(6)	2.71(3)	2.69(4)
Oscillation Amplitude (μm)	2.47(11)	2.50(4)	2.52(4)
BEC Number Fraction N_0/N	0.84(3)	0.82(2)	0.81(2)
Trap Frequency $\omega_o/2\pi$ (Hz)	229.24(4)	229.36(8)	229.36(9)
Minimum Damping Time (s)	3.9	3.8	3.3

Table 3.1: Systematics. This table lists various parameters in our experiment which may contribute to systematic shifts of the measured data. These parameters were measured for all three non-equilibrium scenarios in Sec. 3.2 and show no significant differences.

negligible.

Table 3.1 details the measured values of a number of parameters which might affect a measurement of the temperature dependence of the Casimir-Polder force for all three temperature scenarios reported in Sec. 3.2. None of these parameters showed any significant variation with temperature and can therefore be ruled out as candidates for potential systematic errors.

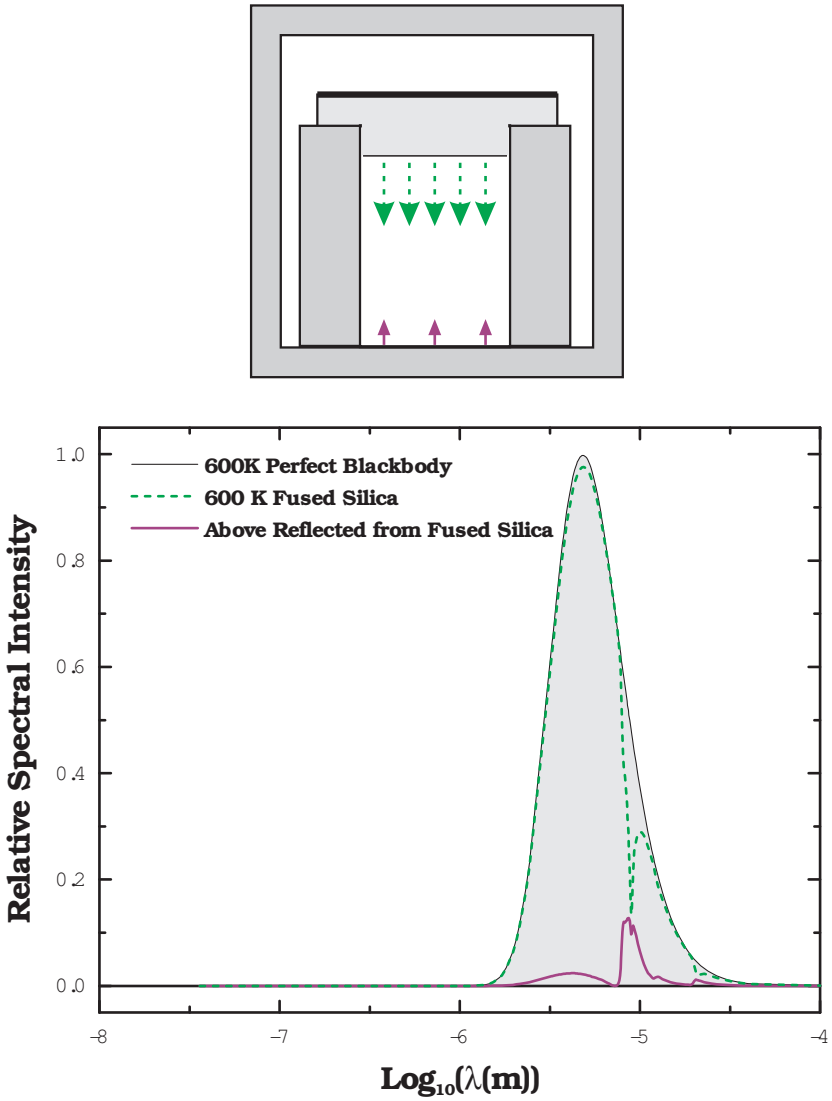

Figure 3.11: Reflected radiation issues. The illustration above addresses the concern that radiation initially emitted by the substrate (large green arrows) may reflect from the bottom surface of the pyrex chamber (small purple arrows) and interact with the atoms upon return. The graph in (b) shows that this effect is negligible and will not contribute significantly to the Casimir-Polder force. The shaded region shows the spectrum of a perfect blackbody radiator, while the green dashed line shows the spectrum radiated from the fused silica. The spectral intensity of the reflected radiation is shown by the solid purple line.

Chapter 4

Measurement of Electric Fields Using Neutral Atoms [37]

In this chapter of the thesis we demonstrate a technique of utilizing magnetically trapped neutral ^{87}Rb atoms to measure the magnitude and direction of electric fields emanating from surface contaminants. We apply an alternating external electric field that adds to (or subtracts from) the surface field in such a way as to resonantly drive the trapped atoms into a mechanical dipole oscillation. The growth rate of the oscillation's amplitude provides information about the magnitude and sign of the surface field gradient. Using this measurement technique, we are able to vectorially reconstruct the electric field produced by surface contaminants. In addition, we can accurately measure the electric fields generated from adsorbed atoms purposely placed onto the surface and account for their systematic effects, which can plague a precision surface-force measurement. We show that baking the substrate can reduce the electric fields emanating from adsorbate, and that the mechanism for reduction is likely surface diffusion, not desorption.

4.1 Introduction to Field Sensory with Neutral Atoms

The advent of cold-atom technology has brought to light a significant amount of knowledge of the physical world, and has also contributed significantly to technology such as time standards and global synchrony. Many precision measurements and experimental realizations have taken advantage of the extremely slow nature of ultracold

atoms, which has resulted in such phenomena as Bose-Einstein condensation (BEC), quantized vortices, ultracold molecules, and atomic parallels to laser optics, to name a few. Recently, the scalability and high level of precision of ultracold atomic systems have led to an increase in their use as precision tools to measure forces and fields at both large [38, 39, 40, 41, 42] and small [14, 15, 19, 20, 27, 43, 44, 45] length scales.

What makes ultracold atomic systems so attractive for precision use is the purity of the actual measurement device, the atoms. One may think of a collection of ultracold atoms as being a large sample of extremely small, yet sensitive, devices that connect to the outside world through trapping fields and narrow linewidth lasers only, with no physical contacts to transfer heat or mechanical and electrical noise. The sensitivity of the device can be tuned by selecting the correct atomic species and desired internal electronic state to meet one's specifications. An atomic ensemble therefore is a tunable system, whose sensitivity (or insensitivity) is well characterized and changeable at the microsecond time scale.

In this chapter of the thesis, we further develop a method of measuring small electric fields near bulk materials with a magnetically trapped BEC of ^{87}Rb atoms [19, 20]. As a test of our ability to measure these electric fields, several clouds of ultracold atoms were purposely adsorbed onto a surface to generate a sizeable field. By measuring the strength of the fields in all three spatial directions, we are able to fully account for the resulting systematic frequency shifts of mechanical dipole oscillations, such as those reported in other experiments [14, 19, 20], and estimate the dipole moment per atom adsorbed onto the surface. In addition, the ability of our magnetic trap to translate along the surface of a bulk substrate allows us to measure electric fields at various surface locations. From these measurements we can fully reconstruct a three-dimensional vector plot of the electric fields that emanate from the surface, with micron-scale resolution of the field. Lastly, we investigate the ability to reduce the strength of surface electric fields by diffusing adsorbates across the surface with heat and find reasonable agreement

with theoretical results.

4.2 Principle of the Surface Electric Field Detection

Since the surface ideally emits fairly weak electric fields, we create measurable fields by purposely depositing ultracold rubidium atoms onto the metal layer, as described in [19]. Briefly, a rubidium atom adsorbed onto the surface changes its atomic level structure in such a way that its valence electron partially resides inside the metal. The resulting charge separation ($\sim$ 1Å) effectively creates a dipole aligned normal to the surface; the dipole's strength is related to the electronegativities of the involved substances. To minimize this effect for our studies of atom-surface interactions, we chose a metal with a low work function for our surface (see Sec. 2.5.1).

Although the motion of neutral atoms is insensitive to uniform electric fields, field gradients will create forces that cause significant perturbations to the atoms' trapping potential. Even during ideal operations, it is unavoidable to deposit rubidium atoms onto the surface; these atoms produce small, uniform field gradients. Since this type of electric field is one of the major systematics in precision surface-force experiments [14, 19, 20], purposely depositing atoms gives us the best tool to account for such errors.

When depositing atoms, we magnetically push low-density noncondensed atom clouds with dimensions ($\sim$ 10μm radially) larger than our BEC dimensions into the surface. The larger spatial extent of the deposited atoms provides more uniform field gradients across the cloud. Immediate analysis of the resultant electric field shows that significant desorption or diffusion of adatoms at room temperature does not occur on timescales of minutes, but rather several days. Atom diffusion and desorption will be discussed further in Section 4.8.

Our method of measuring electric field gradients, partially described in [20], involves the application of an electric field via two conducting plates mounted above and below the science cell, as shown in Fig. 4.1. The plates consist of a thin layer of trans-

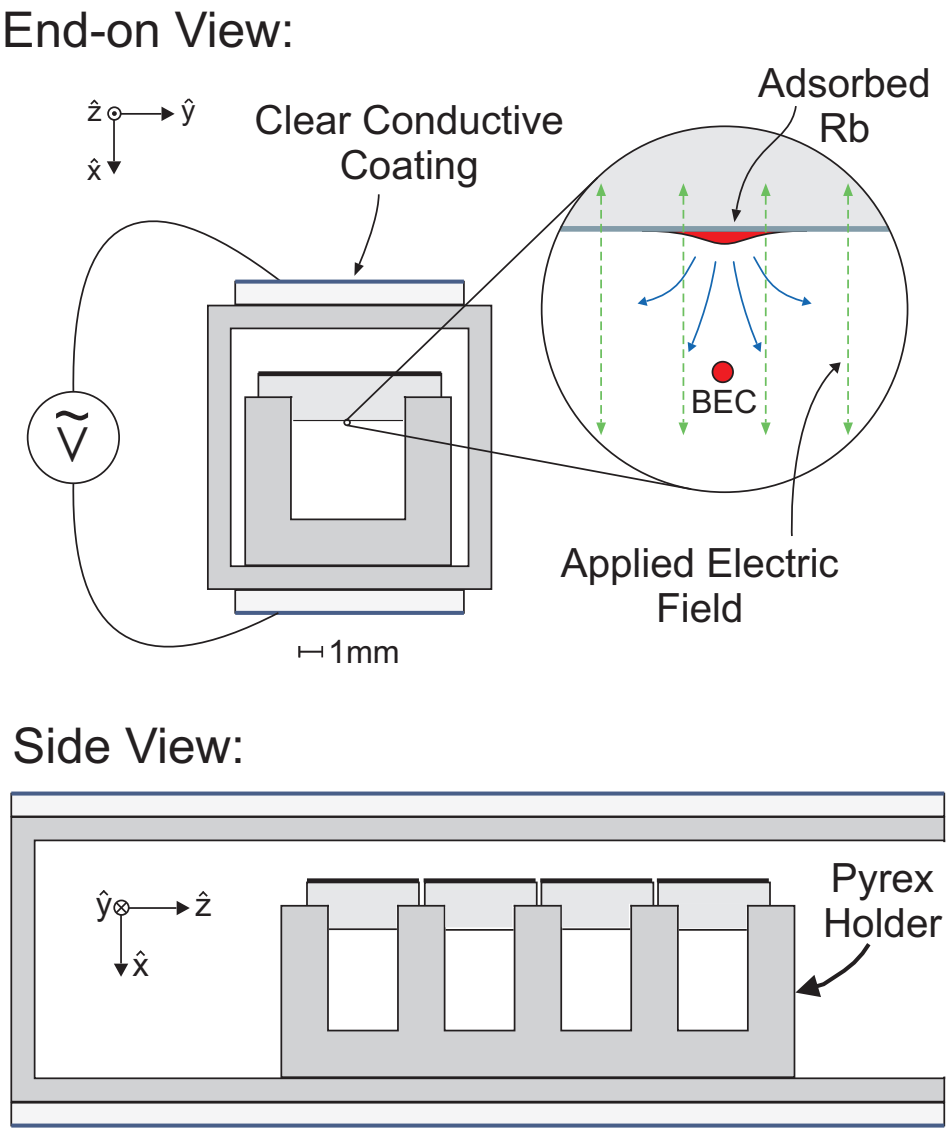

Figure 4.1: Cross section of the science cell. Shown in this figure is a cartoon illustration of an end-on view of our science cell (top) along with a side-view (bottom). The inset shows a magnified view of the relative position of the BEC to the substrate and surface adsorbates (pictured as a red mound with emanating electric fields). Two transparent conductors are placed on top and bottom of the science cell in order to provide an external electric field to the system (shown as dashed green arrows). The applied electric fields add to (or subtract from) the surface electric fields and perturb the trapping potential. By varying the electric field at the trap frequency ω_o the atoms are resonantly driven into a dipole oscillation.

parent indium-tin-oxide (ITO) on $1 \times 10 \times 35$ mm^3 glass plates electrically connected to leads with a conductive epoxy. The use of ITO allows optical access to the cell from the vertical direction, which is necessary for our laser heating method [14], and also leaves open the possibility of imaging through the plates.

Previous studies have shown that an oscillating external electric field will drive a dipole oscillation of trapped neutral atoms if an electric field gradient is present [14, 20]. An atom in an external electric field experiences an energy shift equal to $U_E = -(\alpha_o/2)|\vec{E}|^2$, where α_o is the ground state static polarizability, and a force $\vec{F}$ equal to $-\vec{\nabla}U_E$. Spurious forces that must be measured and accounted for to make claims of accuracy in precision surface-force measurements therefore stem from field gradients:

$$\vec{F}(t) = \frac{\alpha_o}{2}\vec{\nabla}|\vec{E}(t)|^2. \tag{4.1}$$

If an external ac electric field is applied at the trap frequency ω_o, then the system will act as a high-Q resonantly driven oscillator. The electric field from surface contaminants $\vec{E}^*$ and the applied external field $\vec{E}^{ext}(t) = E_x^{ext}\cos(\omega_o t)\hat{x}$ act in tandem to resonantly drive the trapped atoms' motion with a time-varying force,

$$\vec{F}(t) = \frac{\alpha_o}{2}\vec{\nabla}(\vec{E}^* + \vec{E}^{ext}(t))^2. \tag{4.2}$$

If one assumes that the applied electric field is much greater than the field to be measured ($E_x^{ext} >> E_i^*$) and invoking $\vec{\nabla} \times \vec{E}^* \simeq 0$, the total forces on the atoms can be written as

$$F_i(t) \simeq \alpha_o E_x^{ext}\cos(\omega_o t)\partial_x E_i^*, \tag{4.3}$$

for $i = x, y, z$. The center-of-mass oscillation will then resonantly grow, as seen in Fig. 4.2, as

$$q_i(t) = \dot{a}_i\ t\ \cos(\omega t), \tag{4.4}$$

where q_i is the spatial coordinate in the i-direction. The amplitude growth rate in the

i-direction can then be expressed as

$$\dot{a}_i = \frac{\alpha_o E_x^{ext} \partial_x E_i^*}{2m\omega_o}, \tag{4.5}$$

where m is the mass of the atom and the $\pm$ refers to the phase of the oscillation (see Fig. 4.4). Fig. 4.3 shows the amplitude growth rate $\dot{a}_x$ measured at a distance of $x = 10\mu$m from the surface for a number of different applied electric fields E^{ext}. This data demonstrates that Eq. 4.5 is valid for a large range of field strengths ($0 < E^{ext} <$ 180 V/cm).

We measure this growth rate by first transferring the atoms to an anti-trapped state and letting them expand for ~ 5 ms. Two horizontal-imaging beams along $\hat{y}$ and $\hat{z}$ simultaneously image the atom cloud, giving us information about the center-of-mass position of the atom cloud in all three dimensions. Thus, by measuring the resu*l*ting amplitude growth rate, we have a method to measure the gradients of small electric fields from a surface. Fig. 4.2 shows the resulting oscillation of the resonantly driven atom cloud (filled circles) in which the amplitude of the oscillation grows linearly with time. As seen in Eq. 4.5, this growth rate is proportional to the field gradient and becomes much smaller far from the surface or over a clean swath of surface, where field gradients are small.

4.3 Complex Behavior of Resonantly-Driven Oscillator

The underlying principle of the electric-field detection, described in Sec. 4.2, is that atoms starting from rest are resonantly driven into a dipole oscillation by the application of an external electric field. This experiment, however, is just a limiting case of a broad range of experiments which can be performed on such a high-Q system. As Eq. 4.5 suggests, there is more information in a resonantly driven oscillator than just the magnitude of the amplitude growth rate $\dot{a}$, there is also information about the phase of the oscillation, where changing the polarity of the electric field changes the

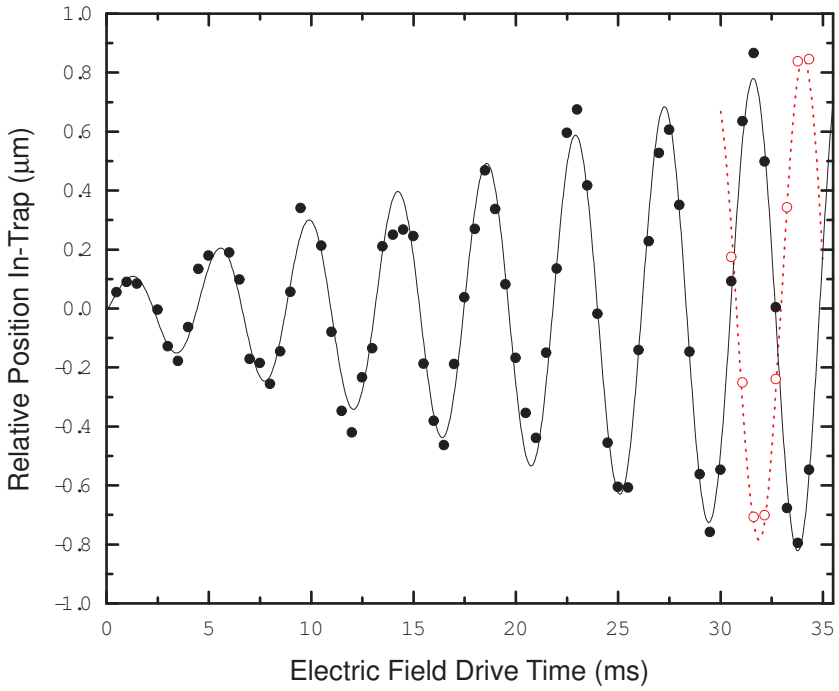

Figure 4.2: Resonantly-driven oscillator. Data showing the relative position of the atoms in a resonantly driven mechanical oscillation (closed black points) with a fit to the data. The rate of growth of the oscillation is directly proportional to the electric-field gradient from surface contaminants. The ability to determine the sign of the field gradient can be seen when the polarity of the electric field is switched (or if the electric field is driven out-of-phase by π). This corresponds to the open (red) circles, showing a clear π-phase change in the oscillation. As expected, no significant growth rate in the z-direction was observed (not shown).

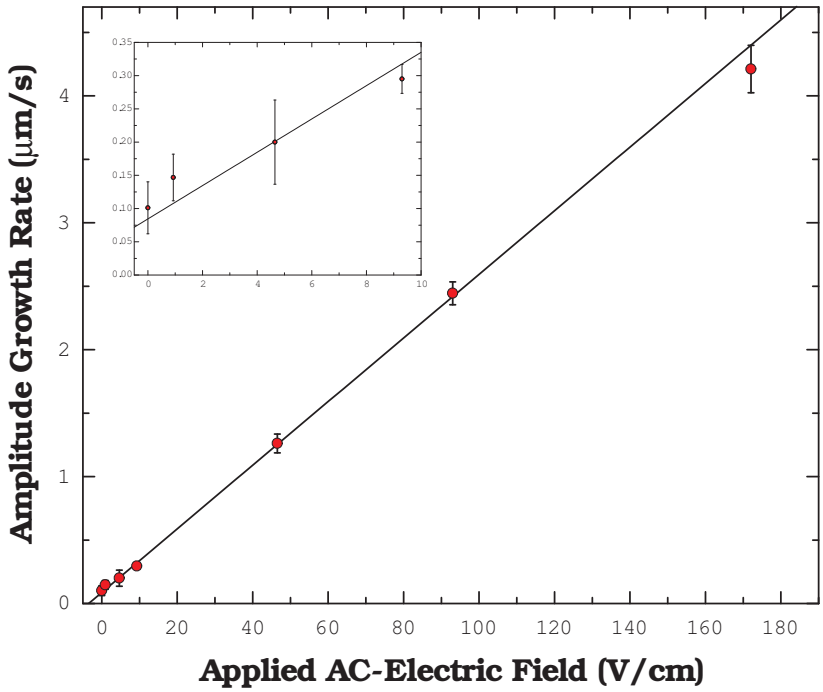

Figure 4.3: Amplitude growth rate vs. applied field. This figure illustrates the linearity of the amplitude growth rate $\dot{a}_x$ with the applied electric field E_x^{ext}. This data shows that the additional electric field does not significantly perturb the surface dipoles for field strengths up to ∼180 V/cm. At some point one would expect a breakdown in this assumption and the strength of the surface dipoles would tend to be very dependent upon the applied field. The black line in this figure is a linear fit of the data. The slight offset at zero applied field could be due to the presence of a pre-existing oscillation.

polarity of $\dot{a}$, shown in Fig. 4.2 as dashed red lines. Fig. 4.4(a) also demonstrates this principle, where atoms which have been purposely placed into a dipole oscillation with a 1 μm amplitude are shown to either grow or shrink in amplitude over time, depending on the polarity of the electric field, which is to say, its phase with respect to the initial oscillation.

A interesting bit of classical dynamics was uncovered in this system (shown in Fig. 4.4(b)) when the external electric field was left on long enough to nearly quench the initial oscillation. What we found was that the oscillation never fully came to a halt and, in fact, showed an interesting phase-change (c) when the oscillation's amplitude approached zero. Naïvely one would expect the amplitude of the oscillation to pass through zero and grow linearly from there in time (dashed red line in (b)). This, however, is not the case and required a great deal of thought about how to analyze these results. Further experiments were done investigating this change in phase of the oscillation (shown in Fig. 4.5).

In this set of experiments the ac-electric field $\vec{E}_{ext}(t)$ was left on while the initial phase ϕ_i of the dipole-oscillation was varied (see Eq. 3.11). The phase of the resultant oscillation was measured after several periods of oscillation ($\sim$30 ms). The results, shown in Fig. 4.5(b), show that the initial growth rate of the oscillation's amplitude $\dot{a}_x$ depends upon the initial phase of the dipole oscillation. This data corroborates the data shown in Fig. 4.4(a) in which the polarity of the applied electric field determined the growth or decay rate of the oscillation.

In essence, there are two phases that define the entire system: ϕ_i the initial phase between the applied electric field and the phase of the dipole oscillation and ϕ_f the phase of the oscillation at some future time relative to its initial phase. The illustration in Fig. 4.4 shows these two phases graphically in the complex plane of the BEC's position. The axis along which the red arrow lies corresponds to the axis of the applied electric field. For atoms starting from rest, the oscillation's amplitude grows linearly with time,

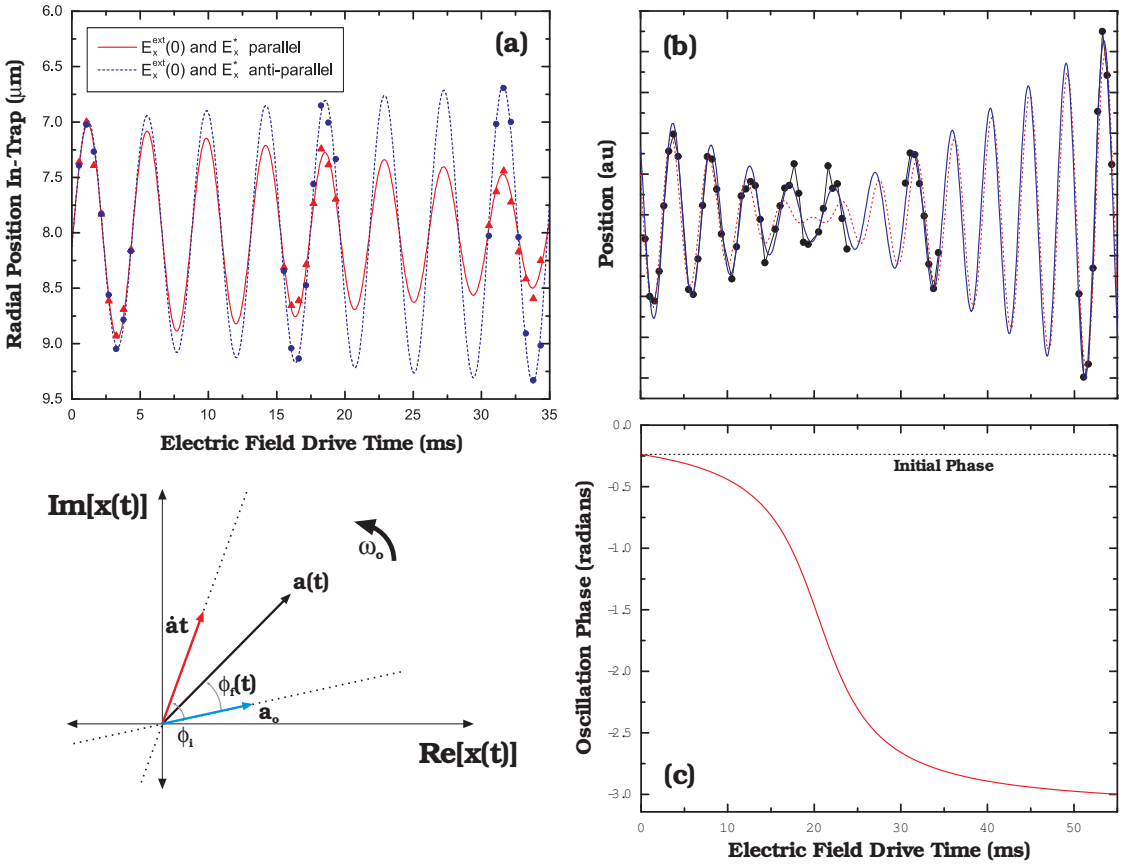

Figure 4.4: Phase evolution during resonant drive. The data in (a) shows the result of applying an electric field after the atoms are purposely placed into a controlled dipole oscillation, described in Sec. 3.2.1. By switching the polarity of the applied electric field, we are able to verify the polarity of the amplitude growth rate $\dot{a}_i$ and determine the sign of the adsorbate's electric field. The data in (b) shows an electric field drive that has been left on long enough to nearly kill the oscillation amplitude. One might expect the amplitude to tend to zero (dashed red line). However, the oscillation never fully comes to rest. Analysis described in the text details how the phase of the oscillation must be matched to the phase of the electric field drive in order to g*et* this fully resonant behavior. When the two phases are not matched, the phase of the oscillation changes over time (c), resulting in the solid line in (b), which better matches the data.

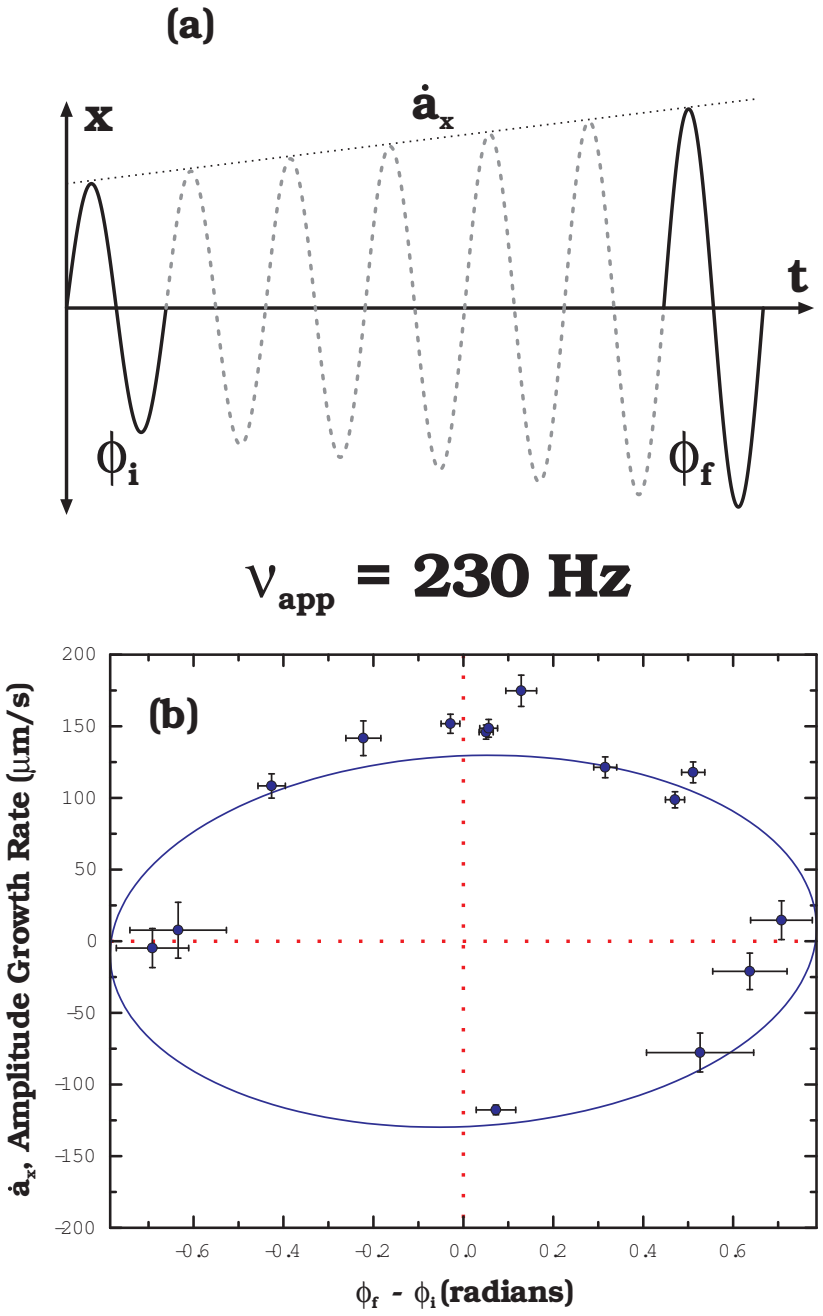

Figure 4.5: Oscillation amplitude vs. applied phase. Shown in (a) is an illustration of an initial BEC oscillation being resonantly driven by an externally applied electric field. The phase of the resonantly-driven oscillation ϕ_i will eventually synchronize with the phase ϕ_f of the applied electric field (driven at 230 Hz). If there exists an initial phase difference (ϕ_f-ϕ_i), the amplitude of the oscillation will not initially begin to grow until the phase of the oscillation matches the phase of the applied field. If the initial phases match, the oscillation will begin to grow in amplitude. This behavior is shown in (b), where the solid blue line shows the expected behavior of the driven-oscillator.

like $\dot{a}\ t$, along this axis, and traces out a spiral pattern. The axis along which the blue arrow lies corresponds to the axis of the initial dipole oscillation's phase. This blue arrow is denoted by the label a_o. For no applied electric field, this vector rotates about the origin with an angular frequency ω_o and traces out a circular pattern.

If the electric field is applied while the atoms are in oscillation, as in the cases of Fig. 4.4 and Fig. 4.5, vector analysis in the complex plane shows that the position of the atoms can be found by finding a functional form of the resultant vector $a(t)$. This analysis, detailed in Appendix B, can be written as follows. For a resonant driving force, of the form,

$$F(t) = F_o \sin(\omega_o t + \phi_i), \tag{4.6}$$

applied to atoms in oscillation, described by $x_o(t) = a_o \cos(\omega_o t)$, the resultant functional form of the position of the atoms will look like,

$$x(t) = a(t) \cos(\omega_o t + \phi_f(t)), \tag{4.7}$$

where ω_o is both the trap frequency *and* the frequency of the driving force. The amplitude $a(t)$ of the oscillation can be written as

$$a(t) = \sqrt{a_o^2 + (\dot{a}t)^2 + 2a_o\dot{a}t\ \cos(\phi_i)}, \tag{4.8}$$

where $\dot{a}$ is defined as the amplitude growth rate,

$$\dot{a} = \frac{-F_o}{2m\omega_o}, \tag{4.9}$$

and the phase of the oscillation can be written as

$$\phi_f(t) = \cos^{-1}\left(\frac{a_o + \dot{a}t\ \cos(\phi_i)}{a(t)}\right). \tag{4.10}$$

The solid blue line in Fig. 4.4(b) shows a fit of the data to the Eq. 4.7. The agreement between the fit and the data is quite remarkable and shows a thorough understanding of the resonantly driven oscillator. The solid red line in (c) shows the

phase $\phi_f(t)$ of the oscillation in (b). The fact that the phase becomes more negative in time implies that the oscillation's frequency appears to be *smaller* than the natural trap frequency over this time period.

Additionally, this analysis helps us describe the data shown in Fig. 4.5(d), in which the measured amplitude growth rate is plotted as a function of the measured phase difference. The magnitude of $\dot{a}$ is greatest when the phase difference is zero. This scenario would correspond to the two axes in Fig. 4.4 being parallel or anti-parallel. When the two axes are $\pi/2$ out of phase, the amplitude growth rate is very small at short times. The solid blue line in Fig. 4.5(d) corresponds to the initial amplitude growth rate as a function of the phase difference $\phi_f - \phi_i$.

4.4 Electric Field Modelling Program and Simulation

A single-particle simulation was created to help gain a deeper understanding of the BEC's interaction with surface electric fields. Data was first taken measuring the electric-field gradient at a number of atom-surface distances (as shown in Fig. 4.6(a)). The data was fit to a single or double power-law dependence to obtain a functional form of the electric-field gradient. This fit function was then integrated in order to fully describe the surface electric field. This functional form of the electric field was then added to the single-particle simulation in an attempt to describe the dynamics of the resonantly-driven BEC.

Incorporating the anti-trapped expansion (described in Sec. 2.2.3) into the simulation, we found excellent agreement between the measured dynamics of the BEC's position and the zero-parameter simulations shown in Fig. 4.6(a) as solid lines through the data points. The anti-trapped expansion adds a bit of complexity to the simulation, due to the fact that atoms ballistically expanding in an anti-trapping potential fall away from the surface very rapidly. In that respect, the expansion time was slightly adjusted and carefully calibrated to have the simulation match the dynamics of the expansion.

This calibration included carefully measuring the amplitude and phase of an atom's oscillation in-trap versus the amplitude and phase following expansion. The amplitude of the oscillation appears ∼20 times larger following ∼5 ms of anti-trapped expansion than it does in trap. Additionally, the relative position of the BEC during the oscillation is roughly $\pi/2$ out of phase with the BEC position following expansion. This is due to the fact that the atom's momentum, as opposed to its in-trap position, is mapped into its position following expansion.

By adding all of these features together, we are able to determine not only the magnitude of the electric field in space, but also the *sign* of the field. This technique allows us to accurately map out the full three-dimensional surface electric field in free space (detailed in Sec. 4.5) and adds to our confidence and understanding in our measurements of these fields.

4.5 Mapping Out Electric Field Vectors From Surface Adsorbates

While Stark shifts are only sensitive to the magnitude of an electric field, our method can also determine the field gradient's direction (as was discussed in Sec. 4.3). When we drive the oscillating electric field, the oscillation begins with the field initially pointing in a known direction. If the initial field polarity is switched, however, the amplitude growth rate changes sign. For atoms starting from rest, the absolute value of the growth rate remains unchanged, and the phase of the driven oscillation shifts by π, as shown by the open (red) circles in Fig. 4.2. This dependence on the phase of the applied electric field allows us to directly determine the direction of the field gradient in the x, y, and z directions at every measured point in space and thus to reconstruct the vector fields.

Fig. 4.6 shows the process of reconstructing the surface electric field created by $7{\times}10^7$ adsorbates. Data is taken directly below ($\Delta y = 0\mu$m, right column) and 40 μm from ($\Delta y = -40\mu$m, left column) the deposited atoms (red mound in (d)). The

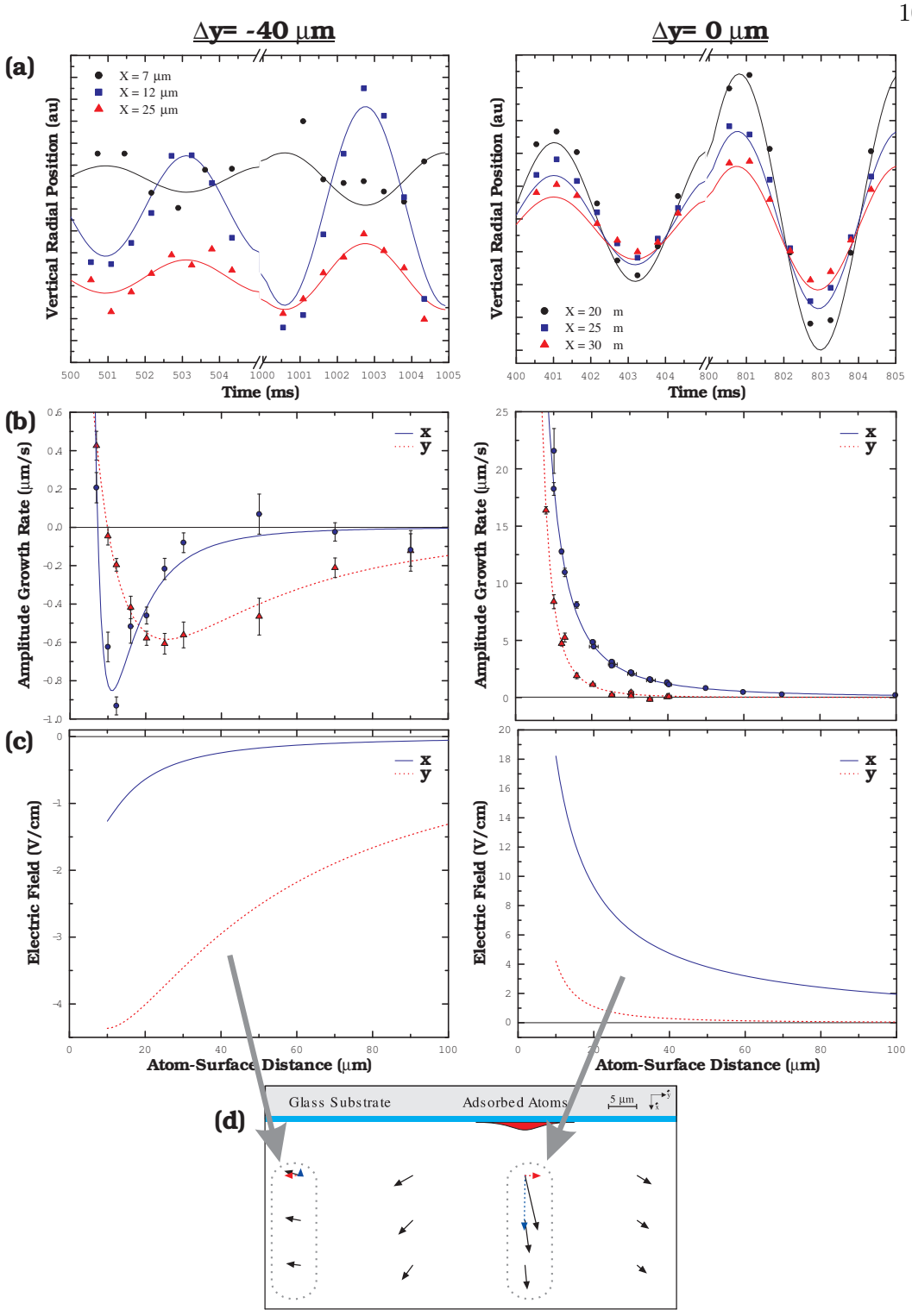

Figure 4.6: Recreating a vector field. The process of reconstructing the vectors from surface electric fields is described here. (a) First, data is taken measuring the amplitude growth rate $\dot{a}$ for the x and y-directions for a number of different locations along the surface (along $\hat{y}$). The amplitude growth rates (b), proportional to the electric field gradients, are then fit to a functional form, which is described in the text (blue solid line and circles and red dashed line and triangles, respectively) as a function of the distance to the surface. By integrating the functional form of the electric-field gradients, we are able to reconstruct the electric field below that spot on the surface, (c) and (d).

amplitude growth rate, described by Eq. 4.5, is measured at a number of distances from the surface (x = 20, 25, and 30 μm for $\Delta y = 0\mu$m and x = 7, 12, and 25 μm for $\Delta y = -40\mu$m) and recorded in (b), where the circles and triangles represent data taken in the $\hat{x}$ and $\hat{y}$ directions, respectively. The amplitude growth rate is directly proportional to the gradient of the surface electric field $\partial_x \vec{E}^*$. The electric field emanating from surface contaminants may be described in the vicinity of the atoms as

$$E_i^* = C_i x^{-p_i}, \tag{4.11}$$

where C_i and p_i are both adjustable parameters. The gradient of this field may then be written as

$$\partial_x E_i^* = -p_i C_i x^{-p_i - 1}, \tag{4.12}$$

By integrating a fit (solid lines in (b)) of this functional form of the field gradient, one obtains a functional form of the surface electric field $\vec{E}^*(x)$, shown in (c), which can be plotted vectorially in (d). This process can be repeated for a number of surface locations to obtain more detailed vector fields. *T*he solid lines in (a) correspond to simulations performed with our modelling program, described in Sec. 4.4.

The solid black arrows in Fig. 4.7(a) and (b) show the reconstruction of the vector field following the adsorption of $\sim 7\times 10^7$ atoms onto the yttrium surface (thick blue line). The dashed gray arrows in (a) indicate the calculated electric field from a thin line of dipoles oriented along $\hat{x}$, extending in and out of the page, whose surface-adsorbate density is represented by the pink layer-cake structure. For any localized dipole pattern, the expected field disagrees significantly with the measured field in both direction and magnitude.

However, if we allow for variability in the number, center position, and spatial width σ_y of the adsorbate pattern, we find qualitative and quantitative agreement with an electric field produced by a similar number of adsorbates to that in (a), but spread more diffusely across the surface (σ_y = 26 μm) than the pattern of adsorbates initially

placed onto the surface. The results of a fitting routine are shown in Fig. 4.7(b), where the more diffuse pattern of dipoles used to model the electric field is shown smeared across the surface.

4.6 Estimating the Dipole Moment per Adatom

The precise characterization of the electric field lets us determine certain properties of the surface. As mentioned earlier, the adsorption of a rubidium atom onto a metal surface creates a surface dipole adsorbate whose strength depends upon the work function of the metal and the ionization energy of the rubidium atom. Previous studies have shown that electric fields from these dipoles can be very large on metals, which prompted the use of glass for our Casimir-Polder force studies [19, 20]. To repeat Casimir-Polder experiments over metal surfaces, metals with work functions lower than the ionization energy of the probe atom would be beneficial to study. By carrying out our electric-field studies, we can determine the dipole moment of an individual rubidium atom adsorbed onto yttrium and compare it to those from other surfaces.

To determine the dipole moment of a single adsorbed atom, we use a modelling program to match the measured field gradient with a calculated field gradient. Our model creates a distribution of N surface dipoles oriented normal to the surface; the physical parameters of the distribution match those of the atom cloud. We then calculate the resulting fields and field gradients that emanate from the surface and compare them with the measured values. The only variable in this model is the dipole moment of one adsorbed atom, which is varied to match calculated and measured field gradients. We neglect to add any surface diffusion process into the modelling program because the measurements to which we compare were made rapidly with respect to surface diffusion times.

Fig. 4.8(a) shows the measured electric-field gradient versus the number of atom clouds adsorbed onto the surface. The linearity of the measured field gradient (0–10

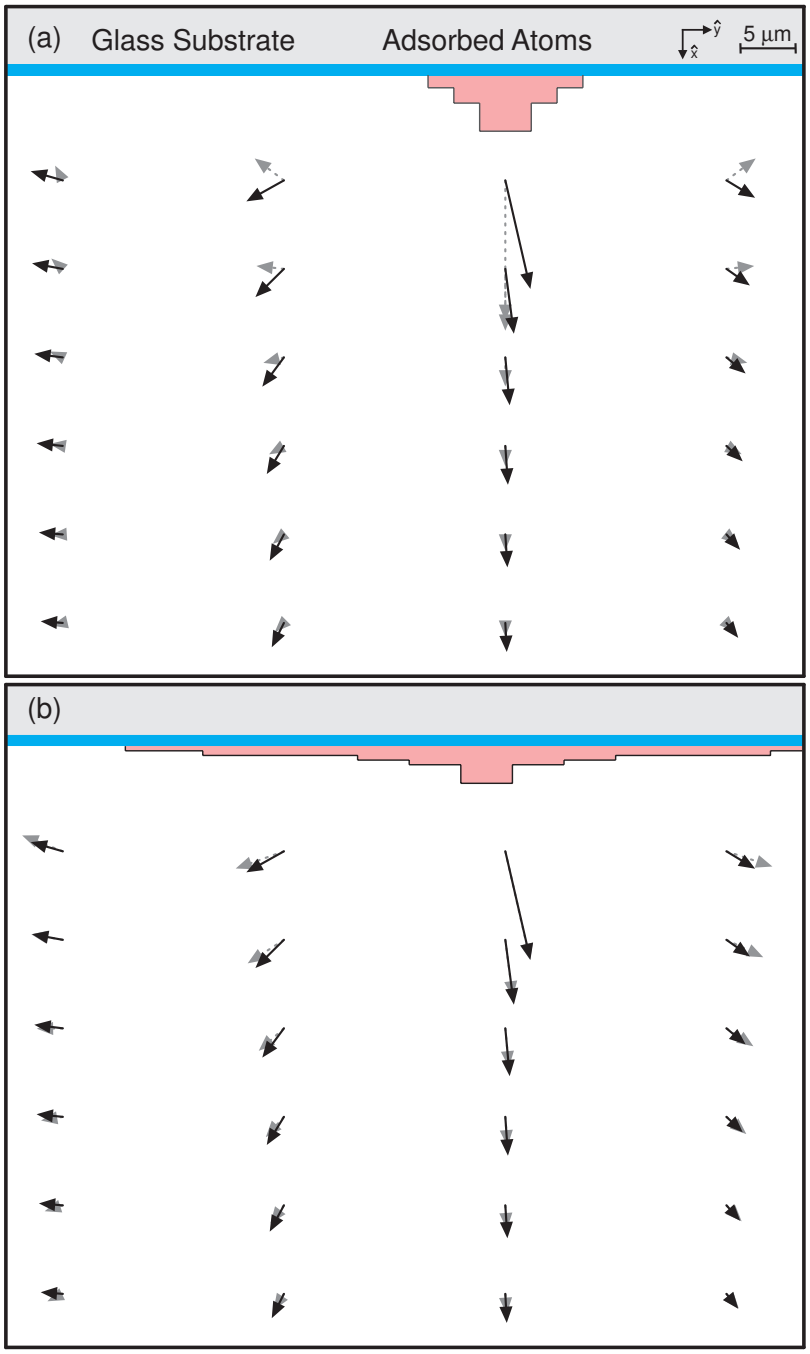

Figure 4.7: Electric-field vectors. Measurements of the electric-field gradients at various positions along the yttrium surface let us reconstruct this 2-D vector plot (solid black arrows) of the electric field generated by adsorbed rubidium atoms (pink layer-cake structure). Analysis was performed in which the measured field was fit to the field of (a) a relatively localized pattern of dipoles and (b) a spatially diffuse pattern of dipoles. The results of the fits are shown as dotted (gray) arrows. The layered structure in (a) indicates the approximate location, spatial extent and surface density of atoms adsorbed onto the surface. The peak surface density of adatoms is much less than one monolayer and would not form a structure extending from the surface. The height of the *cake* indicates the local surface density of dipoles. The axial ($\hat{z}$) size of the applied atoms is a few hundred microns. Fields measured along this axis were negligibly small and are not shown. In this figure, the longest vector represents a field of ∼19 V/cm.

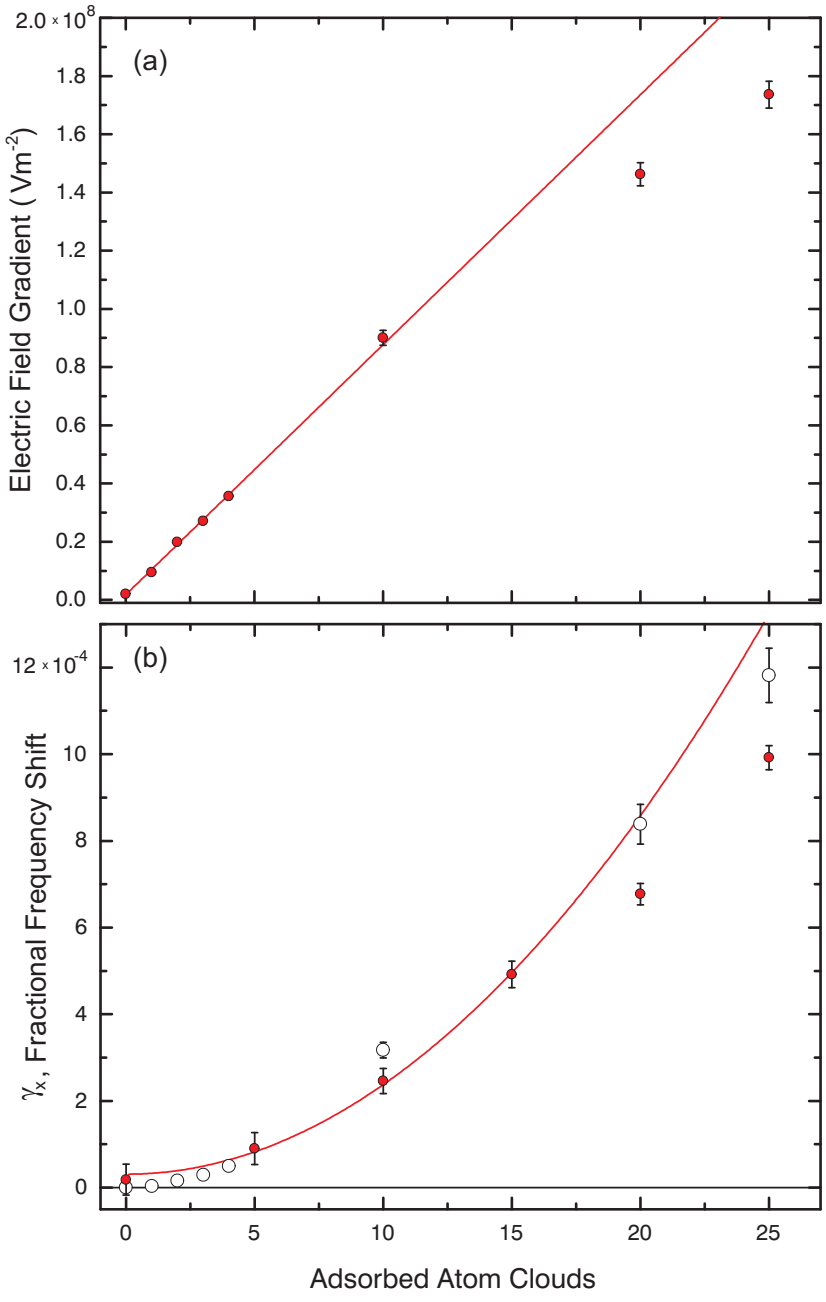

Figure 4.8: Electric fields vs. adsorbate number. (a) A plot of the measured electric-field gradient versus number of clouds adsorbed onto the yttrium surface. The linearity breaks down eventually, possibly due to surface effects such as adatom-adatom interactions. (b) Measured fractional frequency shift data (closed red circles) with the expected fractional frequency shift (open circles) obtained by processing the measured data in (a). The solid lines (red) in (a) and (b) correspond to linear and quadratic fits for data in the 0-15 cloud regime, respectively, illustrating the dependencies of each on the number of adsorbates [Eqs. 4.5 and 4.17, respectively]. The number of atoms in a single cloud is $\sim 1.7 \times 10^6$. This data was taken at $x = 10$ μm from the surface.

clouds) allows us to assume that the field generated from one adsorbed atom is identical to the field generated by one cloud of atoms divided by the number of atoms in that cloud. From this, we find a relation between the electric-field gradient and the number of atoms deposited. Using the procedure described above, we find that the dipole moment per Rb atom adsorbed onto our yttrium surface is ∼35 Debye[1] (corresponding to the valence electron residing ∼ 1 Åwithin the surface, roughly one metallic bond length). We also measure a dipole moment of ∼3.2 Debye for Rb on fused silica, ∼5.4 Debye for Rb on a metallic hafnium surface, and ∼19 Debye for Rb on a metallic lutetium surface. These results are reported in Table 4.1.

The fact that the work functions of the materials are smaller than the ionization energy of rubidium would imply that adsorption of atoms onto the surface would be due purely to van der Waals forces, and would not involve any atom-surface chemistry. This adsorption is referred to as 'physisorption' and would not result in a surface dipole moment from the adsorbate. The fact that a dipole moment is measured on these three surfaces implies that the surfaces are not pure, single-crystal metals, but heterogeneous metals with dissimilar properties. This analysis agrees with the analysis performed in Sec. 2.5.2 and also suggests that this technique of measuring the unit surface-dipole moment is a good indicator of surface quality and character.

4.7 Accounting for Systematic Shifts from Electric Fields

With our knowledge of electric fields from surface contamination, we can accurately account for frequency shifts of dipole oscillations, like those made in [14, 19, 20] that make precision measurements of surface forces. The additional forces from surface contaminants perturb the trapping potential near the surface in such a way that the perturbations result in an unwanted systematic shift of the data. To rule out this sys-

[1] The surface structure that results from our yttrium deposition techniques could cause adsorption dipoles to be different from dipoles on single crystal yttrium.

Surface	ΔE (eV)	p_o (D)	Preparation Method
Hf	-0.3	5.40	sputtering
Y	-1.1	34.5	e^- beam
Lu	-0.9	19.1	oven heating
Glass	?	3.24	N/A

Table 4.1: This chart shows the measured dipole moment per atom adsorbed onto each respective surface. The theoretical values for the desorption energies are shown in the second column. These values are negative due to the fact that each metal's work function (WF) is lower than the ionization energy (IE) of rubidium. These values may not be the true desorption energies of the materials, because one would expect no surface dipole moment from materials with negative desorption energies. The fact that one measures a dipole moment at all suggests the materials are not quite single-crystal, homogeneous materials. Their preparation methods are shown in the fourth column and are described in Sec. 2.5.2.

tematic shift, one may carefully measure field gradients from the surface and calculate the expected frequency shift as follows:

Atoms trapped in a quadratic potential will see perturbations to the trapping frequency that are proportional to the curvature of the perturbing potential,

$$\Delta\gamma_x \approx \frac{-\partial_x^2 U_E}{2m\omega_0^2}, \tag{4.13}$$

where γ_x is the change in trap frequency in the x-direction, normalized to the unperturbed trap frequency ω_o,

$$\gamma_x = 1 - \frac{\omega_x}{\omega_o}. \tag{4.14}$$

We can define $\Delta\gamma_x$ as the contribution to the fractional frequency shift due to the additional surface adsorbates, $U_E = -(\alpha_o/2)|\vec{E^*}|^2$. Eq. 4.13 then becomes

$$\Delta\gamma_x = \frac{\alpha_o}{2m\omega_o^2}\sum_i((\partial_x E_i^*)^2 + E_i^*\partial_x^2 E_i^*). \tag{4.15}$$

If we choose a convenient fitting form of the electric field that approximates the field generated by electrostatic patches, points, and lines for a restricted range of x,

$$E_i^* = C_i x^{-p_i}, \tag{4.16}$$

Eq. 4.15 then becomes,

$$\Delta\gamma_x = \frac{\alpha_o}{2m\omega_o^2}\sum_i(2p_i + 1)p_i C_i^2 x^{-2(p_i+1)}. \tag{4.17}$$

We can then extract C_i and p_i from measurements of the amplitude growth rate $\dot{a}_i$ at various displacements from the surface. The C_i coefficients can then be written as

$$C_i = \frac{2m\omega_i\dot{a}_i}{\alpha_o E_x^{ext} p_i}, \tag{4.18}$$

where ω_i, the frequency of the applied electric field, is chosen to be the trap frequency in the i-direction.

As shown in Fig. 4.8(a), the measured electric-field gradient increased linearly with the number of adsorbed atoms. If we assume that the power-law dependence of

the electric field does not change significantly with the number of applied atoms, we can then deduce that the coefficient C_i is proportional to number of applied atoms. This implies, from Eq. 4.17, that the trap frequency a fixed distance from the surface will vary quadratically with the number of adsorbates as well, since it is proportional to C_i^2. Fig.4.8(b) shows data verifying that indeed the fractional change in trap frequency from the adsorbates $\Delta\gamma_x$ varies quadratically with the number of adsorbed atoms. The open circles in (b) show the results of the above analysis on the data in (a) and agree well with measured values.

With these calculations in hand, we can accurately predict the systematic fractional frequency shift by directly measuring the electric field gradient. The results in Fig. 4.9 show the fractional frequency shift as a function of distance to the surface for two separate locations on the surface. The open triangles were taken over a clean area, where we measured a negligible electric field; the filled circles were taken over a surface location in which we purposely adsorbed $\sim 7 \times 10^7$ atoms. The solid black line represents the theoretical fractional frequency shift predicted by Eq. 4.17, corresponding to measurements made of the electric field emanating from that surface location. The agreement between data and theory illustrates that we can accurately account for frequency shifts from electric fields. For the purpose of characterizing systematic errors to surface-force measurements, our method of characterizing the surface quality of the patch of surface in which small force measurements are made is more directly relevant than canonical surface-science techniques that involve AFM and scanning electron-microscope surface imagery.

4.8 Reducing Electric Fields Strengths with Heat

Apart from characterizing the atoms on a surface and their resulting electric fields, one might also like to demonstrate a way to lessen the strength of the electric fields and their undesirable effects. We achieve this by applying heat to our substrate

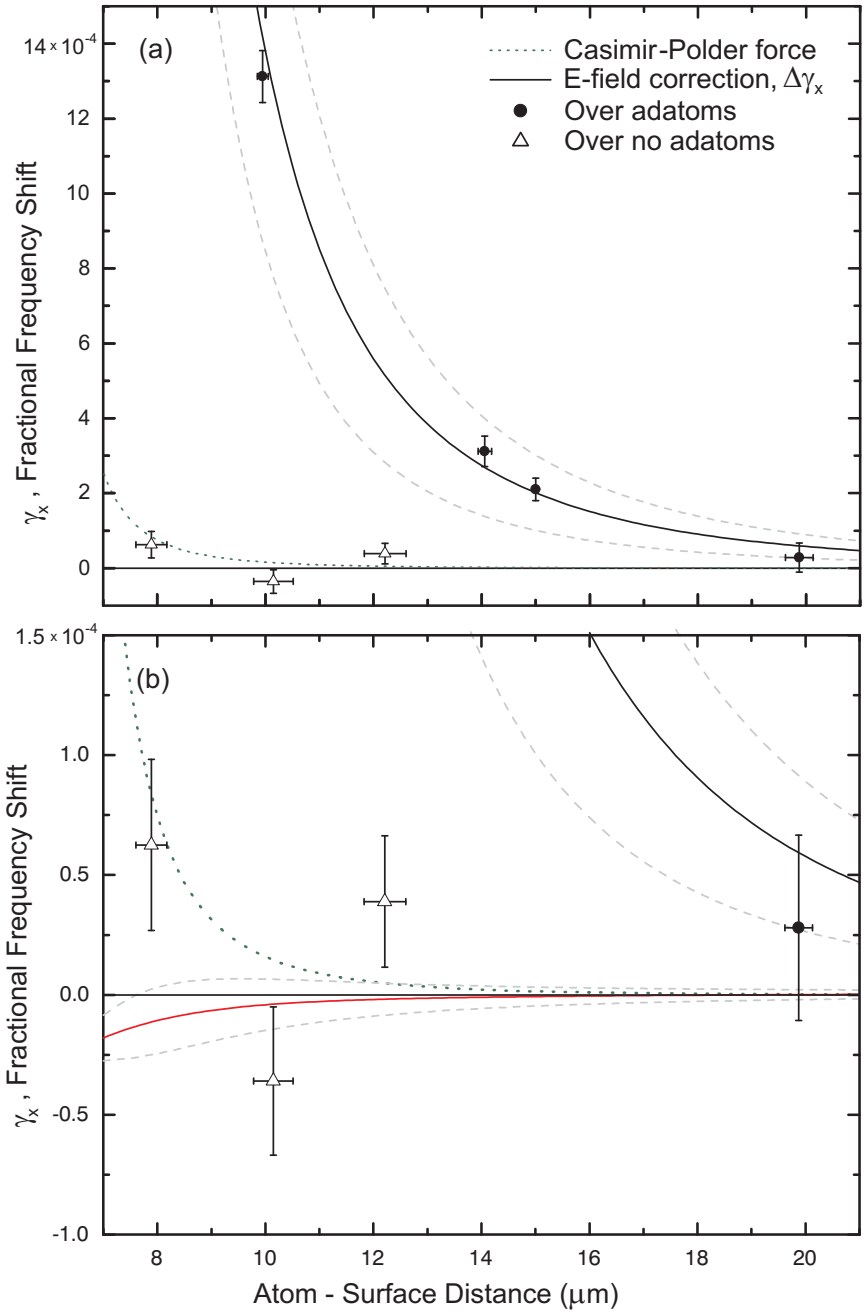

Figure 4.9: Accounting for systematic shifts from electric fields. (a) The measured fractional frequency shift for two separate surface locations. The filled circles are data taken directly below 7 $\times 10^7$ adsorbed atoms, and the solid black line is the shift predicted from electric-field measurements, with measured-error bounds (gray dashed). The open triangles are data taken over a 'clean' surface location (no adatoms) where the electric-field correction is consistent with zero (solid red line in (b)). The correction to data taken over a clean spot is frequently small enough to exhibit a two-component power law dependence for which the correction may, in fact, be slightly negative. The expected Casimir-Polder shift is shown with a green dotted line.

via a high-power laser. The back surface of the fused silica substrate is coated with a $\sim 100\mu$m thick layer of graphite, which is opaque to an infrared heating laser ($\lambda =$ 860 nm). Heating the surface provides enough thermal energy for surface contaminants to redistribute themselves across the surface or to desorb entirely. The temperature of the metallic surface is calibrated versus the power of the heating laser using the same methods as in [14]. This technique should not be confused with light-induced atomic desorption, in which adatoms absorb ultraviolet light and desorb from the surface; in our case, no laser light directly impinges on the adatoms.

The exponential decay time of an electric field emanating from the surface can come from either a desorption process, in which the adatoms escape from the surface-binding potential, or a diffusion process, in which the atoms overcome a smaller hopping energy and hop from site to site, redistributing themselves across the surface. The time scale τ for desorption and diffusion events to take place is characterized by the temperature of the surface T, the energy of activation E_A, and an attempt rate γ_o that depends upon the surface process,

$$\tau(T) = \gamma_o^{-1} e^{E_A/kT}. \tag{4.19}$$

The results of this and a similar study over a fused silica surface can be seen in Fig. 4.10. The similar fits to the data suggest that rubidium has similar activation energies on fused silica and yttrium ($E_A \approx 0.42$ eV on each) and also reveal γ_o to be approximately 15–25 s^{-1}. This measured attempt rate is $\sim$10 orders of magnitude smaller than what one would expect for a desorption process and seems more characteristic of a surface diffusion process that results from numerous random-walk hops. Fig. 4.10 also shows that it is indeed possible to lessen the undesired systematic effects of electric fields on surfaces by baking.

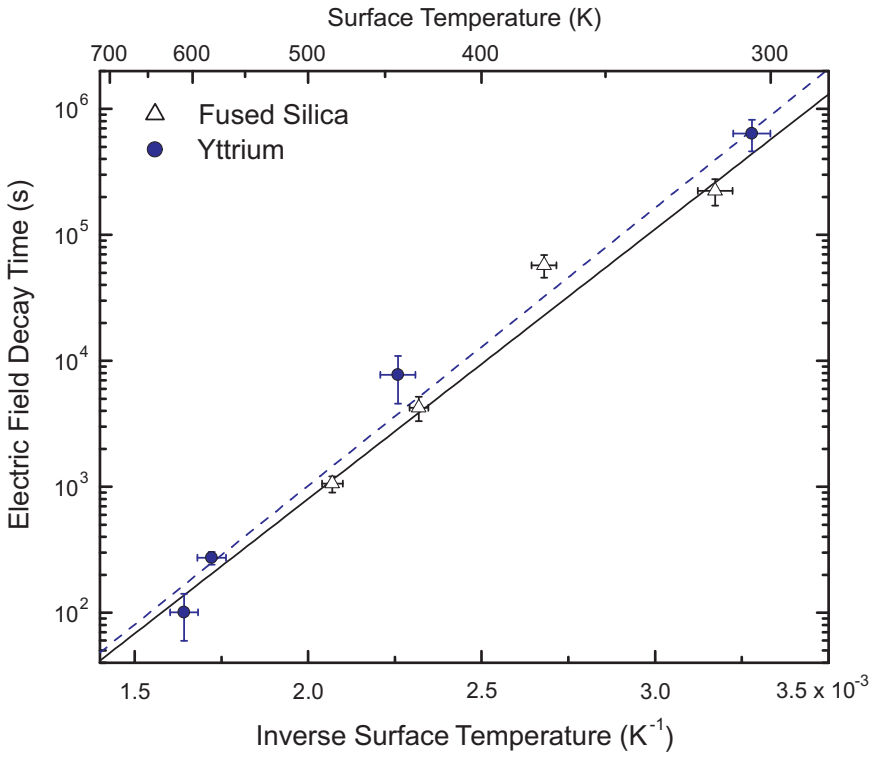

Figure 4.10: Lessening surface electric fields with heat. Decay time of the surface electric field as a function of temperature for a fused silica substrate (open triangles) and an yttrium surface (blue filled circles).

4.9 Possible Extension to Surface Magnetic Field Detection

An appealing feature of this technique is the electric neutrality of the electric-field probe (the ultracold atom cloud). While this specific experiment works with magnetically trapped atoms with non-zero magnetic moments, one could imagine using atoms in the electronic ground state with no inherent magnetic moment ($m_F = 0$). The spherical symmetry of the atom's electron cloud ensures no self-electric fields to disrupt the field being measured, while the lack of a magnetic moment (to first order) similarly ensures a lack of a self-magnetic field. This tandem could provide an extremely neutral electromagnetic probe to study surface fields. In this way one can, in fact, use the technique described in this thesis to measure small surface *magnetic* fields, as well as small electric fields, with a spatial resolution on the micron scale. In the case of magnetic fields, the forces on the atoms would analogously come from field gradients, due to the fact that the potential energy behaves quadratically with magnetic field:

$$U_M = \frac{\alpha_M}{2}|\vec{B}|^2, \tag{4.20}$$

where one can associate a magnetic polarizability arising from the second-order Zeeman shift. Here we define the magnetic polarizability to be

$$\alpha_M = \frac{(g_J - g_I)^2 \mu_B^2}{2E_{HF}}, \tag{4.21}$$

where μ_B is the Bohr magneton, E_{HF} is the ground-state hyperfine splitting, g_J is the electronic g-factor and g_I is the nuclear g-factor. By inserting the above magnetic polarizability into Eq. 4.5, and applying modest magnetic fields ($\sim$100 G), one may obtain measurements of magnetic-field gradients as small as $\sim$3 mG/cm.

Appendix A

Experiments with Ultracold Atoms

This chapter of the thesis describes two sets of experiments that, for one reason or another, were never fully carried out. As atom-surface interaction measurements were being made (reported in Ch. 3 and Ch. 4), future experiments were being thought-out and designed. Hence, the work presented in this chapter represents a great deal of thought and effort in the design of new experiments.

The first set of experiments described in this chapter deals with measurements of atom-surface interactions performed with atom interferometry. The first of these two experiments takes advantage of the coherence of BEC to create an atom-laser interferometer to study both atom-surface interactions and gravitational bound states. The latter experiment exploits the second-order Zeeman shift to create a double-well potential, in which one well is closer to a surface than the other, in order to make atom-interferometric measurements of atom-surface forces.

The second set of experiments outlined in this chapter revisits precision spectroscopy of the nuclear magnetic moment of alkali atoms. This section describes how measurements similar to those made with atomic-beam experiments can be done in ultracold magnetically-trapped atomic clouds achieving competitive precision and accuracy. This measurement would represent a parallel means of measuring nuclear properties of atoms, and may avoid the various systematic effects of previous experiments.

A.1 Atom-Surface Interactions with Atom Interferometry

Laser-light interferometry has proved to be a most useful tool in making precision measurements. However, because of light's insensitivity to electric and magnetic fields, laser-light interferometry not useful for studying electro-magnetic fields near surfaces. However, one may exploit the interactions of atoms with electro-magnetic fields in order to make such measurements. In this section of Appendix A the use of atom interferometry as a tool for making precise atom-surface interaction measurements is investigated.

A.1.1 Gravitational Bound States of an Atom Laser

Following years of atom-surface interaction measurements, an idea arose for an experiment that would not only study atom-surface interactions, but also study gravitational effects due to both the force of gravity and the boundary condition placed on a BEC wavefunction by a surface. In the absence of atom-surface interactions, a surface presents an impenetrable barrier through which atoms cannot tunnel and allows for experiments measuring gravitational bound states, which have only previously been seen in one other experiment [46].

If we were to reconfigure our experiment to place a BEC above, rather than below, a glass surface, we could study the bound states of a gravitational potential of the form, $V(x) = mgx$ for $x > 0$ and $V(x) = \infty$ for $x \leq 0$, where the Casimir-Polder potential is temporarily being ignored here.

The time-independent Schrödinger equation (TISE) can be written for this potential as,

$$\partial_x^2 \psi_n(x) = a^3(x - x_n)\psi_n(x), \tag{A.1}$$

for x > 0, where $\psi_n(x)$ is the wavefunction of the n^{th} bound state and $x_n = E_n/mg$ is

the classical turning point of the atom with energy E_n. The constant a can be written,

$$a^3 = \frac{2m^2 g}{\hbar^2}, \tag{A.2}$$

where m is the mass of a single atom, g is the local acceleration of gravity and $\hbar$ is Planck's constant divided by 2π.

The solutions to the TISE are Airy functions $A_i(x)$ and $B_i(x)$, and the general solution to Eq. A.1 can be written as

$$\psi_n(x) = c_1 A_i(a(x - x_n)) + c_2 B_i(a(x - x_n)). \tag{A.3}$$

The two boundary conditions for this experiment are that the wavefunction must terminate to zero at $x = 0$ and at $x = \infty$. The second boundary condition forces c_2 to be zero, due to the divergent nature of the B_i function. The first boundary condition then quantizes these solutions under the condition that $A_i(-ax_n) = 0$. The roots of the Airy function $A_i(y)$ are well studied and are very well approximated by the function

$$y_n = (\frac{3\pi}{2}(n - \frac{1}{4}))^{2/3}. \tag{A.4}$$

The approximate energy of the n^{th} state can then be written as

$$E_n = (\frac{9mg^2h^2}{32})^{1/3}(n - \frac{1}{4})^{2/3}. \tag{A.5}$$

for n > 0.[1]

Fig. A.1 shows the first 9 bound states $\psi_n^2(x)$ of a Rb BEC for a gravitational potential. The wavefunctions are offset by their respective energy E_n. The dashed red line indicates the addition of the Casimir-Polder force to the gravitational potential.

The idea of the experiment is to bring an ^{87}Rb BEC several micrometers from the surface of the glass substrate (shown in the illustration in Fig. A.1). The BEC would be magnetically trapped in the $|1, -1\rangle$ state and positioned a fixed distance from the surface. Microwave radiation ($\nu \sim 6.8$ GHz) would couple the $|1, -1\rangle$ state to the

[1] The characteristic energy of the system is $(mg^2h^2)^{1/3}$, which equals ~2.8 kHz for ^{87}Rb.

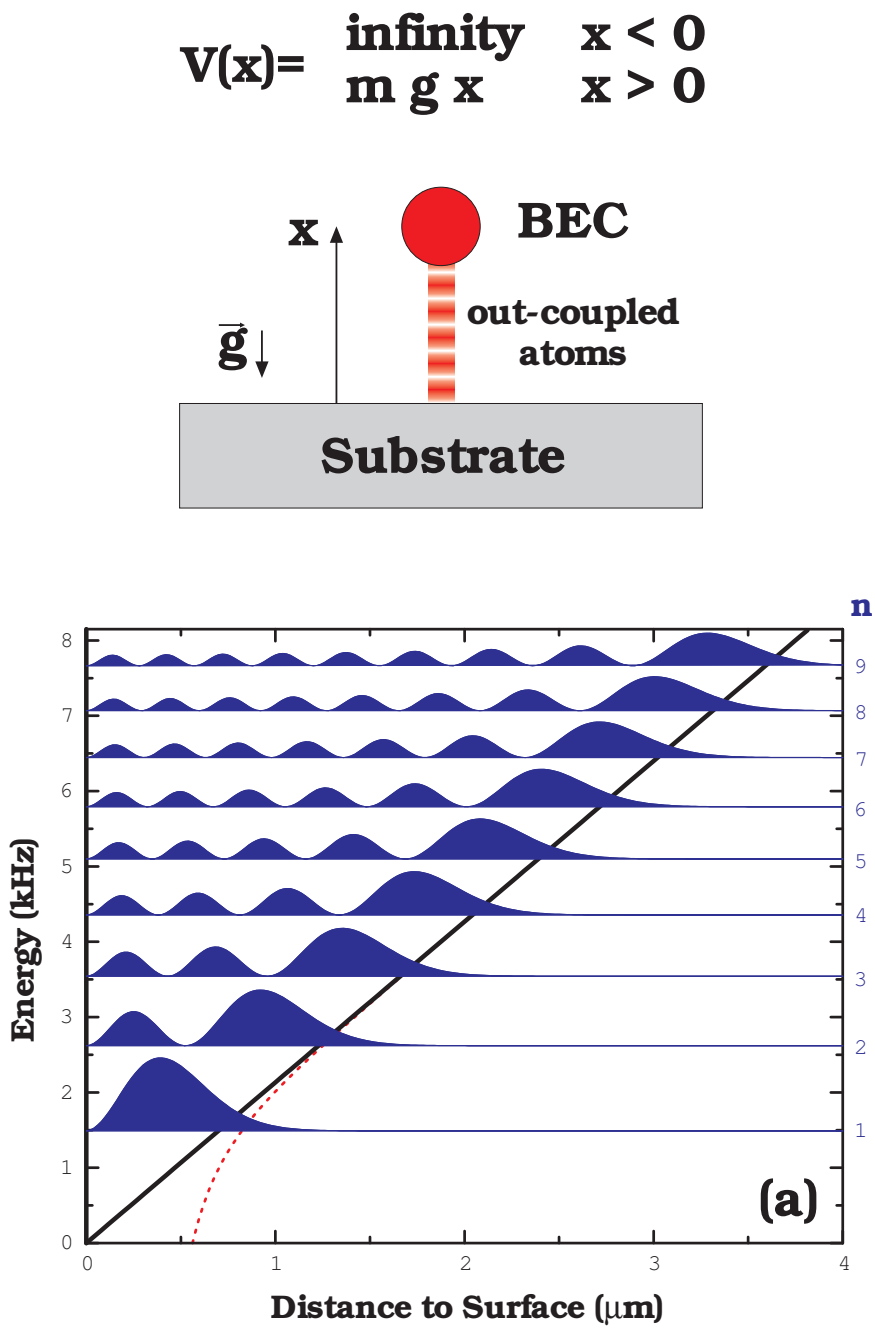

Figure A.1: Gravitational bounds states. This figure shows the idea of the proposed experiment. A BEC is placed several μm above a surface. Atoms are out-coupled from the BEC into the untrapped $|2,0\rangle$ and fall under the influence of gravity. The surface provides an impenetrable boundary, leading to the potential shown in the graph below. Several bound states (n = 1-9) are shown with their respective energies offsetting them from one another. When atoms are out-coupled from the BEC at distances not sufficient to create a bound-state, the BEC will remain intact. Only when quantum-mechanical conditions are met, will the atoms be allowed to out-couple. The red dotted line corresponds to the combined potential consisting of the gravitational force and Casimir-Polder force.

untrapped $|2,0\rangle$ state. This state is very insensitive to magnetic fields and atoms in this state would fall under the influence of gravity, essentially creating an 'atom laser'. Because the atoms sit in a slight magnetic-field gradient (due to gravitational sag), microwave radiation could then very selectively address atoms within the BEC which are a fixed distance from the surface. The out-coupling of these atoms to the untrapped state would only occur if the microwave radiation addresses atoms which sit at x_n from the surface (atoms with energy E_n). Atoms which are not specifically located at x_n would out-couple to states which destructively interfere and the BEC would remain unchanged. The spatial selectivity of the microwave radiation would depend upon the magnetic-field gradient in which the atoms sit, the Zeeman energy shift of the state, and the Rabi frequency of the radiation (assuming the Rabi frequency is larger than the linewidth of the radiation).

Fig. A.2(a) shows the out-coupling spectrum (solid black line) expected for a BEC positioned $\sim 5\mu$m from a glass substrate. Atoms positioned at x_n from the substrate satisfy the condition for a gravitational bound state and are out-coupled to the untrapped state with unit probability. The inverted-parabola shape of the out-coupling spectrum corresponds to the relative BEC atom density at that position. The out-coupled atoms would essentially be defined as an atom laser whose 'wavelength' would be given by the characteristic length scale $\lambda_a = \frac{1}{a}$ (~ 0.3 μm for ^{87}Rb). Here we use the term 'wavelength' loosely, due to the fact that the periodicity of the wavefunction changes with velocity (see Fig. A.1).

In addition to possibly being the second experiment to measure gravitational bound states, this experiment would also have the possibility of measuring atom-surface interactions using atom-laser spectroscopy. An atom-surface interaction potential $U_i(x)$ would act as a perturbation to the gravitational potential and would shift the energy of the bound states accordingly. To first order, this energy shift would be proportional to

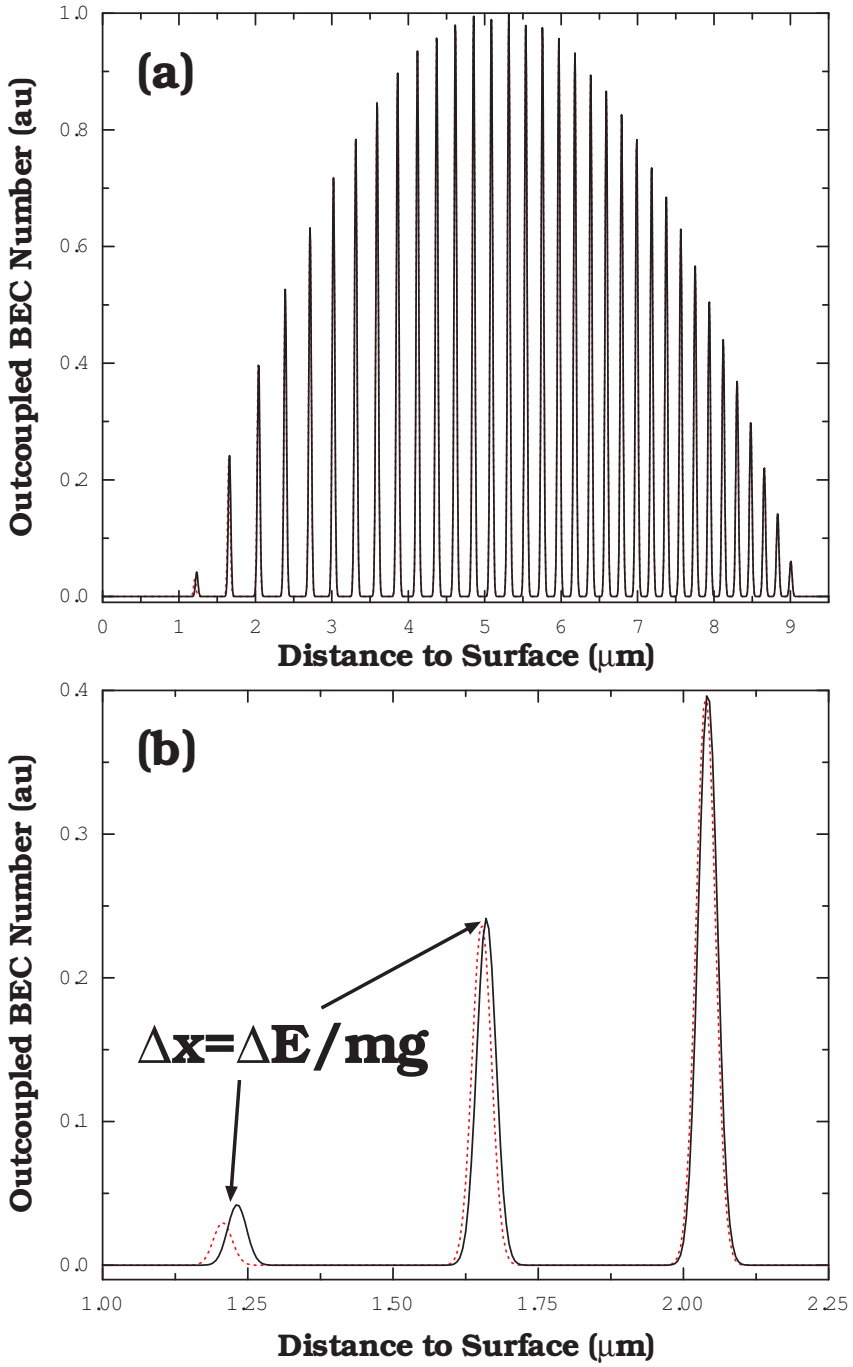

Figure A.2: Out-coupled BEC spectrum. The graph in (a) shows a BEC placed ∼5 μm from a surface. Only when boundary conditions are met, will the BEC be allowed to out-couple atoms to the untrapped $|2, 0\rangle$ to form gravitationally bound states. The spectrum has an inverted-parabolic shape due to the fact that the number of out-coupled atoms at a given distance will be proportional to the atomic-density within the BEC. The graph in (b) shows the first three identifiable bound states (corresponding to $n =$ 2, 3, and 4). The presence of an atom-surface interaction, like the Casimir-Polder force, would shift the spectra by a small, yet measurable amount ΔE. This method provides a means of using an atom-laser to perform atom-surface interaction studies.

the interaction energy,

$$\Delta E_n = \langle \psi_n^0 | U_i | \psi_n^0 \rangle. \tag{A.6}$$

where ψ_n^0 represents the unperturbed wavefunctions.

Problems with this analysis arise, however, when the atom-surface interaction energy scales like a power-law whose potential energy becomes much larger than the bound-state energy near to the surface. For instance, the potential energy of the Casimir-Polder force is roughly equal to the bound-state energies for atom-surface separations less than 0.5 μm. This size scale is roughly the same size scale as the atom-laser wavelength λ_a. When these size scales become comparable quantum reflectivity becomes a great concern.

A great amount of research has been done by other groups detailing the nature of quantum reflections [27, 47, 48, 49, 50]. Essentially, the quantum reflection process occurs only when the potential energy of an attractive surface force changes suddenly (on a length scale small compared to the size scale λ_a of the wavefunction). The length scale β, associated with the Casimir-Polder force, can be written as,

$$\beta = \sqrt{\frac{2mC_4}{\hbar^2}}, \tag{A.7}$$

where C_4 is related to the strength of the Casimir-Polder force by $U_{CP} \sim -C_4 x^{-4}$ [48].

If we look at the condition that $\beta \ll \lambda_a$ we find the condition that,

$$C_4 \ll C_{4,max} = (\frac{\hbar^{10}}{32m^7 g^2})^{1/3}, \tag{A.8}$$

in order to see an appreciable quantum reflection. For ^{87}Rb this requires $C_4 \ll C_{4,max} = 3.5 \times 10^{-57}$ Jm^4. However, C_4 for ^{87}Rb is about 25 times larger than $C_{4,max}$, making quantum reflection extremely unlikely.

Solutions exist, however, that would make this experiment feasible (even for ^{87}Rb). As Eq. A.8 implies, we may do one of the following to increase quantum reflection. We may reduce the mass of the quantum object that's being reflected from

the surface. In the case of alkali-atom BEC, this would mean working with hydrogen (H), meta-stable helium (He*), lithium (Li) or even sodium (Na) BEC. Because $C_{4,max}$ scales like $m^{-7/3}$, one would benefit a great deal by reducing the mass of the atom by factors of $\sim$4–87. Indeed for H, He* and Li, reflection probabilities approach unity.

Lighter-mass alkali atoms also tend to have much larger ionization energies (the smallest of the bunch is that of Na, 5.1 eV). Such low work functions are very desirable when working with atom-surface interactions for reasons described in Sec. 2.5.1. Essentially, atoms with higher work functions have lower propensities for sticking to surfaces and generating unwanted electric fields. This makes working with lighter atoms highly desirable.

In addition, we may increase the quantum reflectivity of the atom laser by *decreasing* the C_4 coefficient. This may be done by lowering the mass density of the material, as was done by Pasquini, *et al.* [50], or by adding an additional potential that would cancel the Casimir-Polder potential. The latter may be done by adding a blue-detuned evanescent wave via total internal reflection of an externally applied laser. One may vary the intensity of the laser to explore the interesting competition between the Casimir-Polder force and the force from the evanescent waves, as has been done in similar experiments by Landragin *et al.* [27]. It would be interesting to see how the bound-state energies would depend upon this intensity.

Fig. A.2(b) shows the would-be measured atom-laser spectra of the gravitational bound states ($n = 2, 3, 4$) for no atom-surface interaction (solid black line) and for an atom-surface interaction equal to the Casimir-Polder potential. If we (wrongly) assume that the perturbed bound-state energy $E_n + \Delta E_n$ is equal to the unperturbed bound-state energy plus $U_{CP}(x_n)$, then we would expect to see the atom-laser spectra shift due to the atom-surface interaction (red dashed line). Our wrong assumption becomes more correct for weaker atom-surface interactions where the length scale of the interaction β becomes much smaller than the atom-laser wavelength λ_a.

A.1.2 Two-State Surface Probe

Another experiment was investigated which also takes advantage of atom interferometry to study atom-surface interactions. In this experiment an atom is put into a superposition of two atomic ground states, one of which is closer to a surface than another. The phase of the state which is closer to the surface will evolve at a slightly faster rate than the state which is further, and may be measured with Ramsey spectroscopy. The additional rate of change in the quantum-mechanical phase evolution will appear as a change in the measured Ramsey frequency.

The key idea of the experiment is to find two nearly identical states whose spatial overlap may be controlled very precisely via an external variable. In the case of this proposed experiment the two states of interest are the $|1,-1\rangle$ and $|2,1\rangle$ states of ^{87}Rb and the external variable is an applied magnetic field. The magnetic moments of these two states are nearly identical, and only d*i*ffer to second order. The Breit-Rabi formula (Eq. A.16) describes how both energy levels behave with applied magnetic fields.

The externally-applied magnetic field in this experiment comes from the field of our permanent magnets as well as from a variable bias field B_o. The magnitude of the total field can be written as,

$$|\vec{B}(x)| = \sqrt{B_o^2 + \gamma^2 x^2}, \tag{A.9}$$

where γ is the magnetic-field gradient from the permanent magnets ($\sim$510 G/cm). This field is shown in the illustration in Fig. A.3.

The potential energy experienced by these two states can be written as a sum of the magnetic-field potential $U_M(x)$ and the gravitational potential $-mgx$, where m is the mass of the atom and g is the local acceleration of gravity,

$$U(x) = U_M(x) - mgx. \tag{A.10}$$

The magnetic potential energy is a combination of Eqs. A.16 and A.9.

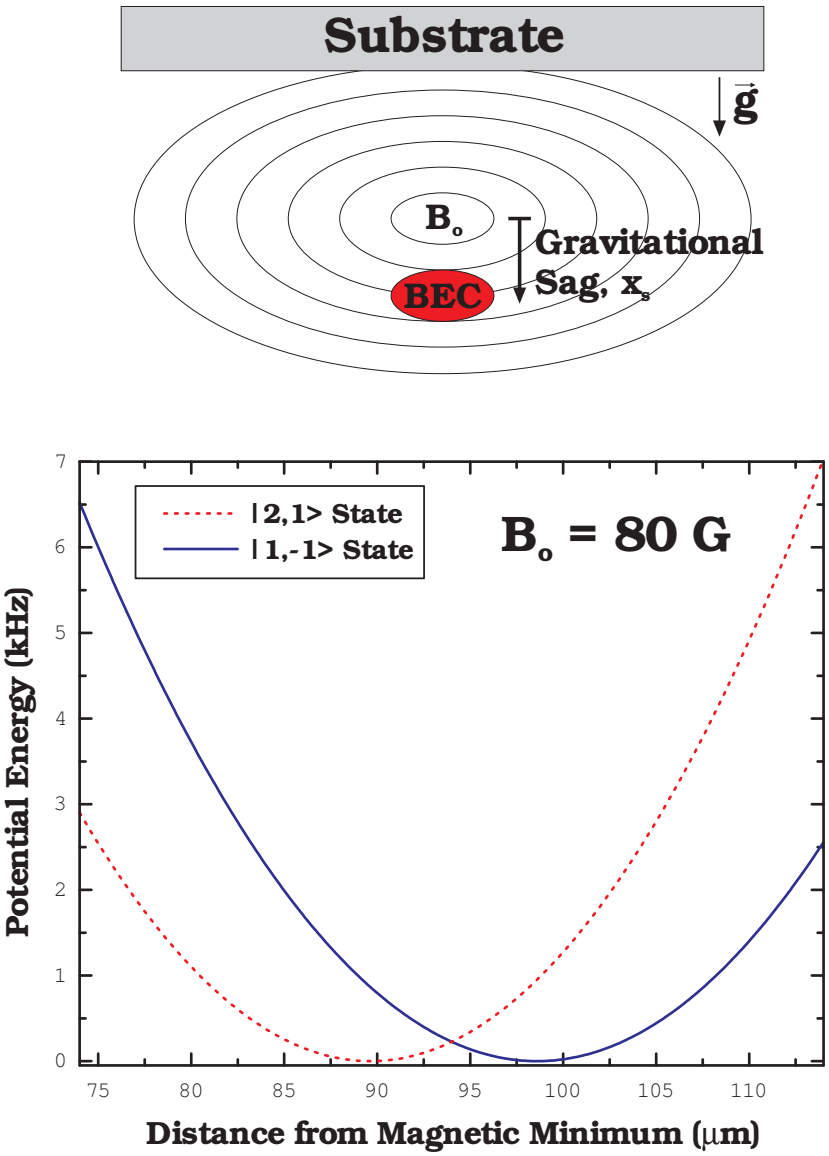

Figure A.3: $|1\rangle$ and $|2\rangle$ gravitational sag. The illustration in this figure shows the relative position of a BEC in the magnetic trapping field. The force of gravity pulls the BEC away from both the substrate and the minimum of the magnetic field (labelled B_o). The graph below shows the total potential energy $U(x)$ for both the $|1,-1\rangle$ and the $|2,1\rangle$ state of ^{87}Rb. When the bias magnetic field is 80 G, the gravitational sag is slightly different for these two states. The $|1,-1\rangle$ is trapped more weakly (solid blue line) and is pulled about 10 μm further from the surface than the $|2,1\rangle$.

The presence of gravity in this experiment is crucial to the interferometric scheme used to measure surface interactions. The illustration in Fig. A.3 shows the position of the BEC relative to the minimum of the magnetic field B_o. This displacement is referred to as the 'gravitational sag' and can be approximated very well by replacing the Breit-Rabi formula with the linear Zeeman effect $U_M = m_F g_F \mu_B B$. Here $m_F g_F = 1/2$ for both the $|1,-1\rangle$ and $|2,1\rangle$ states (hereafter referred to as $|1\rangle$ and $|2\rangle$, respectively), and μ_B is the Bohr magneton. The gravitational sag x_s for both states can then be approximated to first order as,

$$x_s(B_o) = \frac{B_o}{\gamma}(\psi^{-2} - 1)^{-1/2} \approx \frac{B_o \psi}{\gamma}, \tag{A.11}$$

which is equal to 1.17 μm/G for our magnetic trap. Here

$$\psi = \frac{mg}{m_F g_F \mu_B \gamma}. \tag{A.12}$$

Fig. A.4(a) shows data verifying the gravitational sag position as a function of the bias magnetic field. Because the magnetic moments of $|1\rangle$ and $|2\rangle$ are not quite equal, their sag positions are also not quite equal and differ slightly depending on the applied magnetic field. The graph in Fig. A.3 shows the potential energy experienced by the $|1\rangle$ and $|2\rangle$ with an applied magnetic field of 80 G. The gravitational force pulls the $|2\rangle$ $\sim$90 μm from the minimum magnetic field and pulls the $|1\rangle$ approximately 10 μm farther.

This difference in sag positions is the key focus of this experiment and provides a spatial separation of the two states which is dependent upon the applied magnetic field. This spatial separation Δx_s is difficult to determine analytically and was estimated by dimensional analysis of the Breit-Rabi formula,

$$\Delta x_s(B_o) \propto \frac{mg}{\gamma^2 E_{hfs}}(B_o - B_{ms})^2. \tag{A.13}$$

This suggests that Δx_s is proportional to x_s (from Eq. A.11). In fact numerical analysis

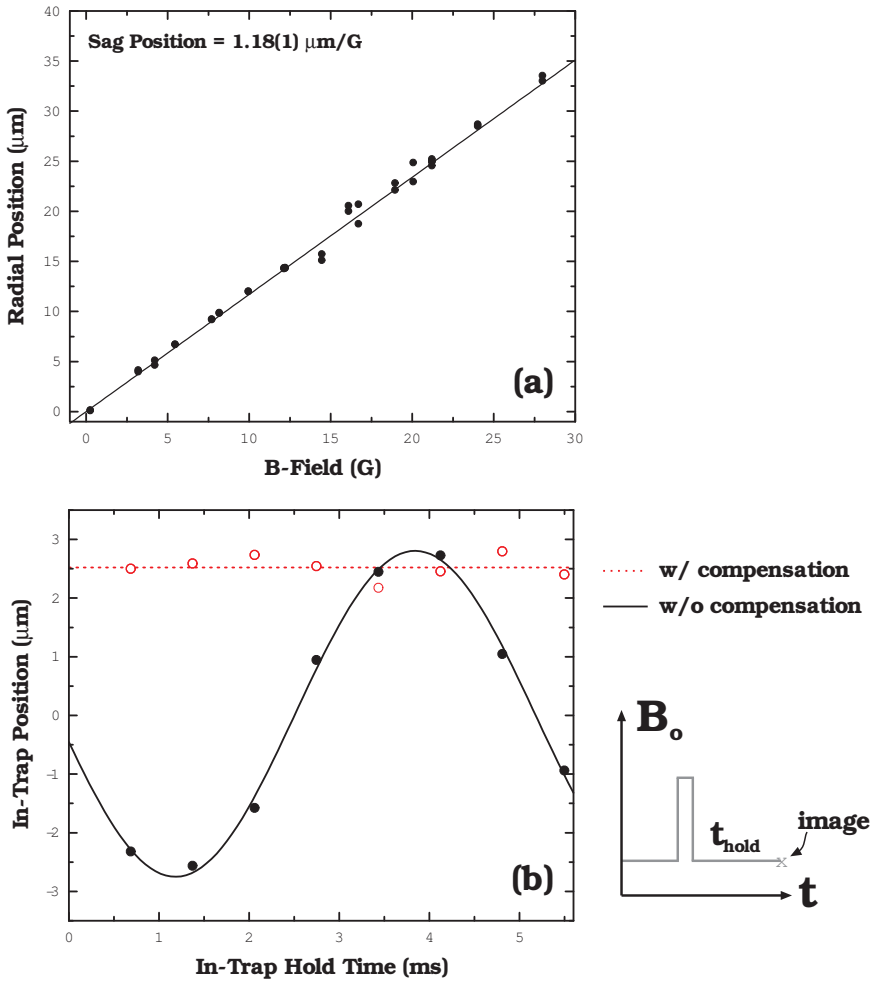

Figure A.4: Gravitational sag compensation. The data in (a) show the measured in-trap position of atoms in the $|1,-1\rangle$ as a function of the bias magnetic field. The slope of this data agrees well with the calculated value of 1.17 μm/G. The data in (b) show the results of an experiment testing the compensation field that was applied to the system. The experimental procedure is shown by the sequence to the right. The bias magnetic field is jumped very rapidly with (dotted red line) and without (solid black line) the compensation field. When the compensation field is not present the atoms undergo a large oscillation. When the compensation field is applied, the atoms remain at rest.

confirms the following equation to be nearly exact for Δx_s,

$$\Delta x_s(B_o) = \chi x_s^*(B_o)\frac{(B_o - B_{ms})}{\Xi} \tag{A.14}$$

where Ξ is the characteristic magnetic field for second-order energy shifts ($\Xi = 2438$ G for ^{87}Rb),

$$\Xi = \frac{E_{hfs}}{(g_J - g_I)\mu_B}, \tag{A.15}$$

here x_s^* is the mean gravitational sag position of the $|1\rangle$ and $|2\rangle$ (approximately given by Eq. A.11), and B_{ms} is the 'magic spot' magnetic field, described in Sec. A.2.1. The dimensionless parameter χ was found numerically to be $\sim$3. This gives a separation of $\sim$1.4 $\times 10^{-3} \mu$m/G^2 for our magnetic trap.

With this formalism in hand, we are able to fully account for the spatial separation of the $|1\rangle$ and $|2\rangle$ as a function of magnetic field. In order to get any reasonable separation ($\sim$0.1 μm) between the two states, we must work at a $\sim$10 G magnetic field. The gravitational sag of both states is roughly 12 μm at this field and would hinder atom-surface interaction measurements. However, this sag may be compensated for by the application of a bias magnetic field.

Fig. A.5(a) and (b) show the difference between applying and not applying a compensation field to the system. By compensating for the gravitational sag of the $|1\rangle$, the $|2\rangle$ is allowed to move slightly closer Δx_s to the surface. The experiment (b) would look at follows: atoms begin in either the $|1\rangle$ or $|2\rangle$ (filled red circle) and are placed into a superposition state (red and white filled circle) by the application of a $\pi/2$ pulse (time progresses rightward in the illustration). Once the atoms are placed into a superposition the bias magnetic field (dashed green line) is slowly ramped up (slow with respect to collective oscillations). The compensation field (dotted black line) is applied in tandem with the bias field in order to prevent the $|1\rangle$ from moving. The atoms are t*h*en recombined in space by ramping the fields back to their original values and a $\pi/2$ pulse is applied. The relative phase between the two states is measured by recording the

final state population as a function of time. The frequency of the population's oscillation (Ramsey frequency) should be equal to the relative energy difference between the two states. Changes in this frequency should be proportional to additional potential energies from atom-surface interactions.

By applying a compensation field, the bias field may be varied much more rapidly than collective oscillation time scales using this method. This allows for very short interaction times, which is useful when measuring rapid Ramsey frequencies. Fig. A.4(b) shows the results of applying a very rapid magnetic field pulse to atoms in the magnetic trap. The solid black line shows the results of the experiment without a compensation field being applied. The atoms see the field pulse as a 'kick' and oscillate in-trap. When the compensation field is applied, the atoms are prevented from oscillating, as seen with the open circles (dotted red line).

A number of challenges immediately confront this experiment. First, as the two states separate in space, the coherence time between them falls rapidly to zero (as shown with the data in Fig. A.6(b)). The coherence time is largest near the magic spot (3.23 G) and decreases to nearly 10 ms with a 10 G field [12, 51]. In essence, there exists a competition for the experiment: the larger the spatial separation between states, the smaller the coherence time. Additionally, the relative Ramsey frequency difference between the two states becomes larger for larger spatial separations (shown with the data in Fig. A.6(a)). This obstacle may be overcome by detuning the frequency of the applied $\pi/2$ pulses in order to observe several periods of a Ramsey oscillation within the coherence-time window.

As if these challenges weren't enough to overcome, there exists a density-dependent frequency shift of the Ramsey frequency. This suggests that low-density thermal clouds be used to measure the atomic interference. However, a thermal cloud may only get so close to the surface before its density changes (from mechanical surface evaporation) and an apparent frequency shift is recorded.

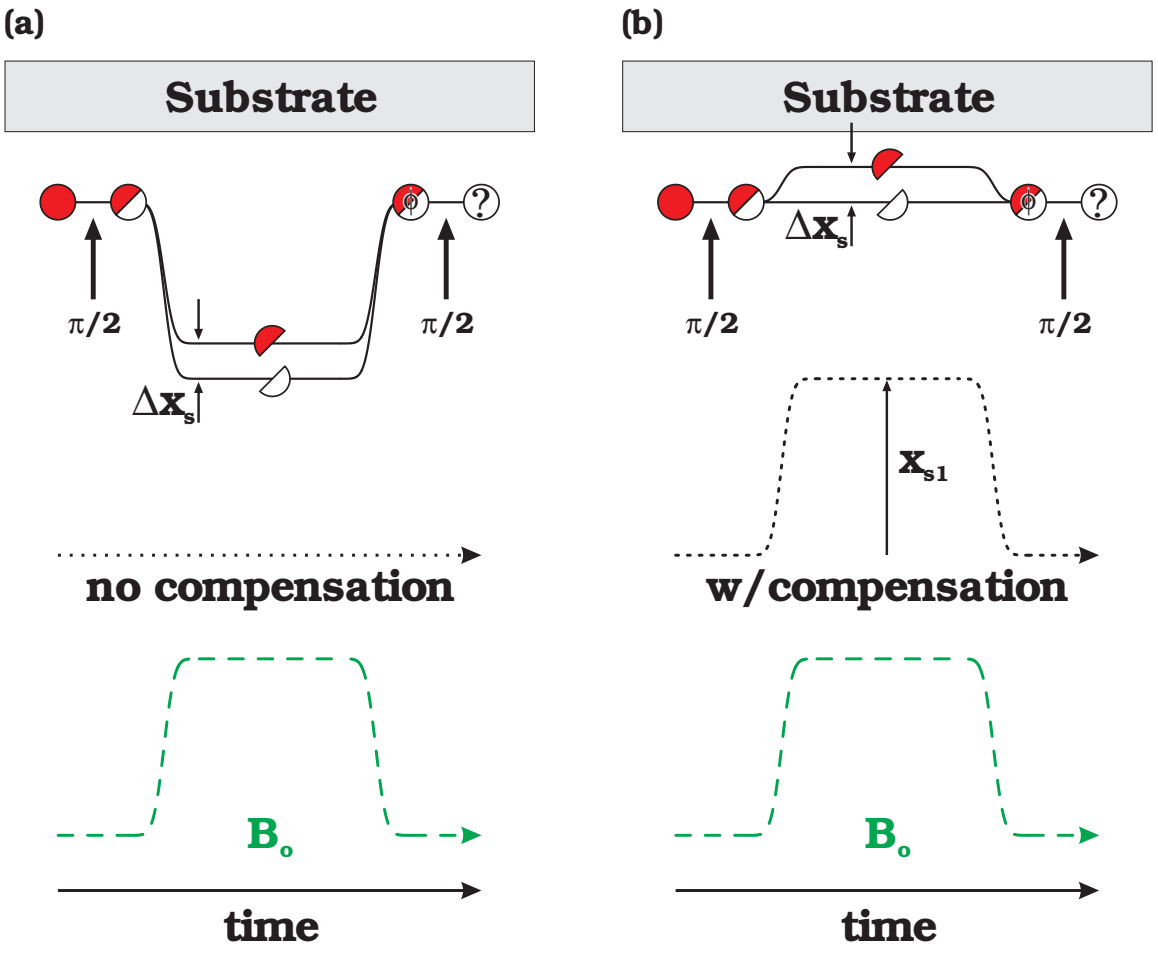

Figure A.5: Two-state surface probe. The time sequence in (a) shows the problem encountered when a compensation field (dotted black line) is not applied to the experiment. As the bias magnetic field B_o (dashed green line) is ramped up, the atoms are pulled away from the surface by gravity, making atom-surface measurements difficult. However, when a compensation field *is* applied, the atoms remain at the surface to perform measurements. The sequence shows the interferometric measurement. Atoms starting in one state (red) are placed into a superposition state (red and white) by a $\pi/2$ pulse. As both the bias field and compensation field are increased the two states separate spatially, allowing the $|2\rangle$ to probe the atom-surface interaction. The atoms are recombined spatially and a subsequent $\pi/2$ pulse reads out the relative population in each state. The acquired phase should be proportional to the atom-surface interaction potential.

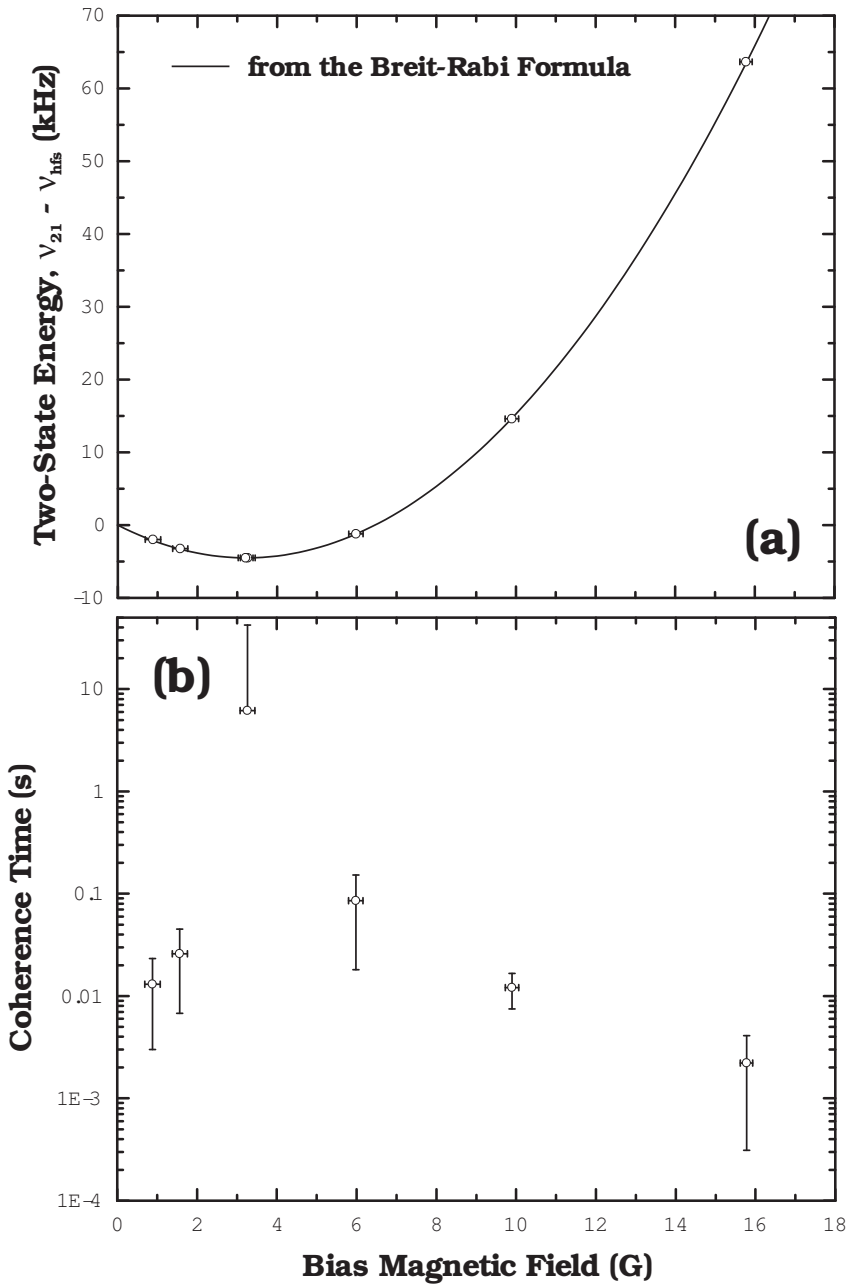

Figure A.6: Two-state coherence time and energy. Graph (a) shows the two-state energy difference given by the Breit-Rabi formula with data taken over a large range of magnetic fields (1-16 G). The energy difference ν_{21} is relative to the zero-field hyperfine splitting ($\nu_{hfs} \simeq 6.8$ GHz) and was measured with Ramsey spectroscopy. The solid black line is a zero-adjustable-parameter theory curve. The vertical error bars are much smaller than the data points. The coherence time between the $|1\rangle$ and $|2\rangle$ is shown in (b) and shows a very long coherence time near the magic spot ($B_{ms} = 3.23$ G) and very short coherence times at larger and smaller magnetic fields. Short coherence times limit measurement accuracies and prove to be a significant roadblock in making precise measurements.

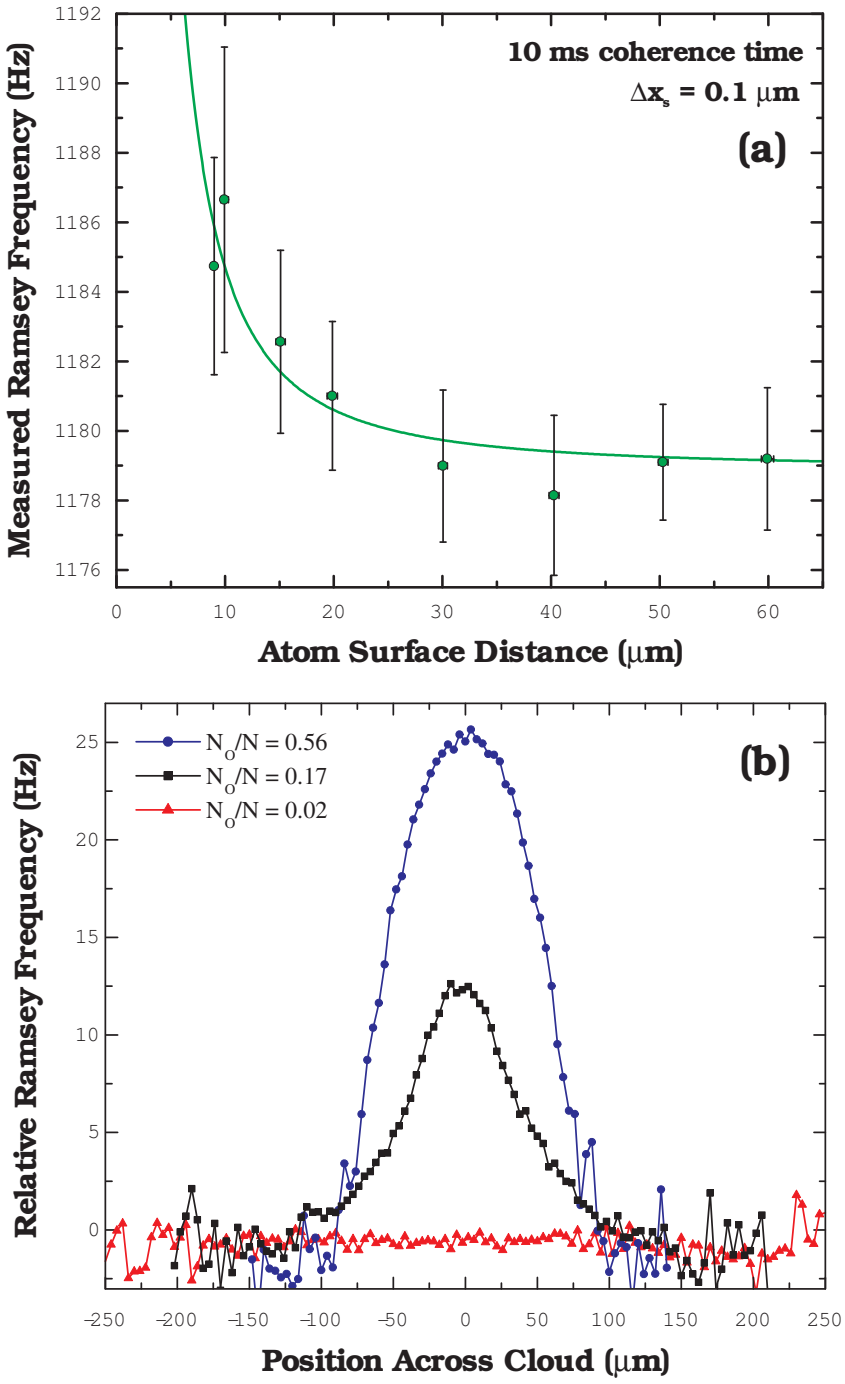

Figure A.7: Density shift and results. The data in (a) show the results of the experiment, in which the measured Ramsey frequency increases as the two-state probe (shown in Fig. A.5) approaches the surface. The results are a bit misleading. The increase in the Ramsey frequency is most likely due to the increase in the thermal cloud density and not due to an atom-surface interaction. The Casimir-Polder force, for instance, would give a signal orders of magnitude lower than the signal measured here. The data in (b) clearly show the density-dependent shift for two partially-condensed clouds (black square and blue circles). For a low-density thermal cloud (red triangles), the density-dependent shift appears to be nearly zero.

Fig. A.7(b) shows the density dependent frequency shift recorded for three different atomic ensembles. The red triangles correspond to the relative Ramsey frequency measured across a low-density thermal cloud ($N_o/N \sim 0.02$). For a higher-density cloud ($N_o/N \sim 0.17$) a frequency shift of a few tens of Hz can be seen with the black squares. For a very dense BEC ($N_o/N \sim 0.56$) the frequency shift becomes more apparent, as seen with the blue circles.

An interesting effect can be seen with the black-squares data: despite having partially condensed, the cloud does not appear to have a spatially bi-modal nature to its frequency profile. This is due to the fact that while the cloud may have a bi-modal nature in its density profile, it also has a bi-modal nature to its density-dependent shift [12, 51]. BEC atoms tend to possess exactly *half* the frequency shift that non-condensed atoms would have with similar densities. This results in a spatially-continuous energy shift across the cloud. A non-continuous shift would result in *infinite* forces within the ensemble ($\partial_x U < \infty$).

The misleading results of the experiment, shown in Fig. A.7(a), show an apparent shift in the measured Ramsey frequency as the atom-surface distance tends to zero. This apparent shift is most likely due to the explanation given earlier in which low-density thermal clouds undergo mechanical evaporation by slightly contacting the surface. The increased atom density gives rise to an apparent signal. This effect may, however, be avoided in other experiments by exploiting the lack of a density-dependent shift in certain fermionic atomic ensembles.

A.1.3 Versatile Double-Well Potential

The system discussed above in Sec. A.1.2 may also be of interest in creating a versatile double-well potential. Fig. A.3 shows the trapping-potentials for the $|1\rangle$ and $|2\rangle$ of ^{87}Rb with a bias magnetic field of 80 G. For a large bias field like this, the two potentials separate in space, described by Eq. A.14. By applying a very specific

microwave-coupling frequency, one may couple the two potentials together to create a double-well potential, like that shown in Fig. A.8(a). When the microwave radiation is tuned to specifically couple the two potentials at the mean position between the two minima, one finds the resulting double-well potential to be symmetric about the center (solid black line in (a)). By varying the power of the coupling, one may round the intersection of the two potentials and effectively vary the barrier height (shown as a faint gray line). By detuning this microwave coupling slightly, one may create a potential imbalance between the two wells: a positive detuning (b) would raise the rig*h*t well, while a negative detuning (c) would raise the left.

This system is also very robust, due to the fact that both the barrier height and the potential imbalance are controlled by the power and frequency (both very controllable variables) of the microwave coupling, respectively, and the separation between the wells is controlled by an externally applied magnetic field.

This double-well potential may also be used as an interferometric tool to study rotations and accelerations gyroscopically. The key ingredient in experiments such as these is to create an enclosed area with the two atomic states. If, instead of running *time* rightward in Fig. A.5, we run space rightward, we create an enclosed area. This may be accomplished by physically translating the atoms in space as they separate. The enclosed area would be equal to the product of the separation Δx_s and the translational distance.

A.2 Measuring the Nuclear Magnetic Moment of Trapped Atoms

Once, while working with the Breit-Rabi formula, I happened to stumble upon an interesting method of measuring the nuclear magnetic moment $\mu_I = g_I \mu_B$ of alkali atoms through the comparison of two separate hyperfine transitions in the ground state manifold, where μ_B is the Bohr magneton and g_I is the nuclear g-factor.

The Breit-Rabi formula describes the energy shift of a ground state atom for a

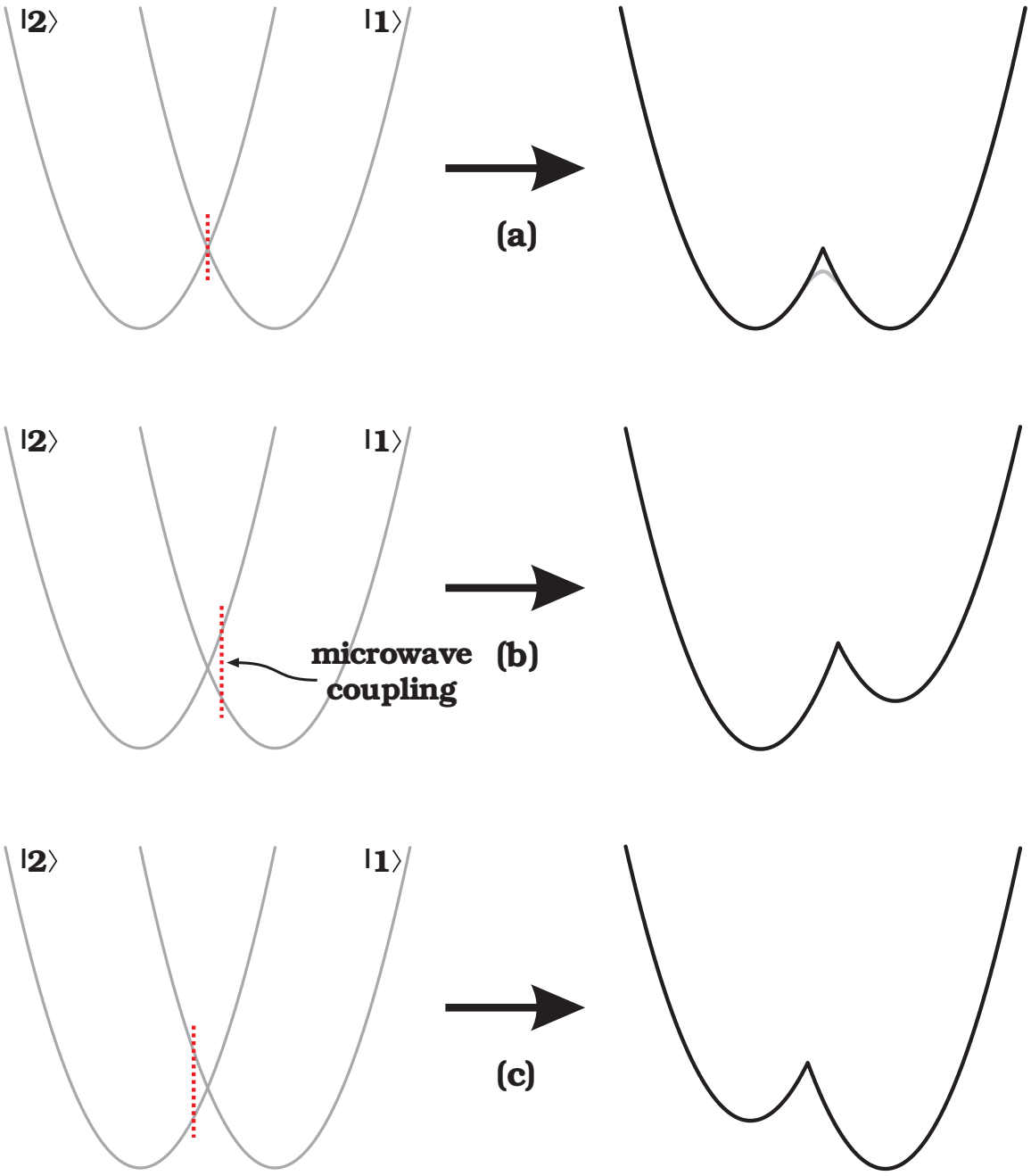

Figure A.8: Designer double-well potential. This figure shows the ability to create a unique double-well potential from the $|1,-1\rangle$ and $|2,1\rangle$ of ^{87}Rb. As shown in Fig. A.3(b), the force of gravity spatially separates the trapping potentials by several μm by applying a modest magnetic field ($\sim$ 80 G). By applying a specific microwave coupling, the combined potential would look like the solid black line potential to the right. The illustration in (a) shows a symmetric double well potential whose height may be adjusted by varying the power of the microwave radiation (the potential is rounded near the overlap, shown as a gray line). By detuning the microwave coupling the symmetry of the double-well is broken, leading to an imbalance in the double-well ((b) and (c)).

given magnetic field B and can be written as

$$U(m_F, B) = g_I \mu_B m_F B + \frac{E_{hfs}}{2}(\pm(1 + \frac{4m_F x}{2I+1} + x^2)^{1/2} - \frac{1}{2I+1}), \tag{A.16}$$

where the $\pm$ is used for the $F = I \pm J$ state, respectively, and

$$x \equiv \frac{(g_J - g_I)\mu_B B}{E_{hfs}}. \tag{A.17}$$

The zero-field hyperfine energy splitting is written as E_{hfs}, I is the total nuclear angular momentum, J is the total electronic angular momentum and g_J is the Landé g-factor.

We can write the equation for the field dependence of a rig*h*tward, $\sigma+$ transition, in which the atom receives a photon which drives it from an $|m_F\rangle$ to $|m_F + 1\rangle$ state as,

$$U_R(m_F, B) = U_+(m_F + 1, B) - U_-(m_F, B), \tag{A.18}$$

where the (+) or (–) convention indicates the higher or lower energy state, respectively.[2] We can then write the functional form of this transition's energy as

$$U_R(m_F, B) = \frac{E_{hfs}}{2}\left(\sqrt{1 + \frac{4(m_F+1)x}{2I+1} + x^2} + \sqrt{1 + \frac{4m_F x}{2I+1} + x^2}\right) + g_I \mu_B B. \tag{A.19}$$

Similarly, we can define a leftward transition arising from a $\sigma-$ transition,

$$U_L(m_F, B) = U_+(m_F, B) - U_-(m_F + 1, B) \tag{A.20}$$

and

$$U_L(m_F, B) = \frac{E_{hfs}}{2}\left(\sqrt{1 + \frac{4m_F x}{2I+1} + x^2} + \sqrt{1 + \frac{4(m_F+1)x}{2I+1} + x^2}\right) - g_I \mu_B B. \tag{A.21}$$

See Fig. A.9(a) and (b) for an illustration of the transitions.

The interesting physics lies in the energy difference Υ between these two transitions,

$$\Upsilon(B) = U_R(B) - U_L(B) = 2 g_I \mu_B B, \tag{A.22}$$

[2] One should use caution with this convention when dealing with ^{40}K, which has an inverted hyperfine structure ($A_J < 0$).

where here we assume similar m_F states are being used. This energy difference Υ is *exactly* equal to twice the product of μ_I and B and corresponds to the energy cost of flipping the nuclear magnetic moment in a magnetic field.[3] Since $\Upsilon(0) = 0$ and no higher-order terms exist, one may define the nuclear gyromagnetic ratio g_I to be exactly equal to

$$g_I = \frac{\Upsilon(B)}{2\mu_B B}. \tag{A.23}$$

Fig. A.9(a) illustrates the concept of measuring two very similar transitions (which cross to form an 'X'). In the absence of a nuclear magnetic moment these two transitions behave identically. However, the presence of the nuclear magnetic moment makes these transitions slightly different. The energy level diagrams of the ground state manifolds of ^{40}K and ^{87}Rb are shown in (b), with crossing arrows showing candidate states in which a nuclear magnetic moment measurement might be made.

Fig. A.9(c) illustrates the two transitions $U_L(B)$ and $U_R(B)$ for a quartet of states in ^{87}Rb ($|1,-1\rangle \rightarrow |2,0\rangle$ and $|1,0\rangle \rightarrow |2,-1\rangle$, shown in (b)). The graph in this figure shows the field dependencies of both transitions and demonstrates how they both come to minimum values very near to one another (marked by the dashed vertical lines). These minima have been dubbed 'magic spots' in the past due to the fact that there is exactly no magnetic field dependence of the transition at these field values [12]. If one were to accurately measure both curves in Fig. A.9, one would have a precise determination of the nuclear magnetic moment, determined by Eq. A.23.

We can look at the feasibility in making this measurement for all three naturally occurring potassium isotopes (^{39}K, ^{40}K, and ^{41}K), as well as both rubidium isotopes (^{85}Rb, and ^{87}Rb), for instance. If we look at the error in measuring g_I we find that

$$(\frac{\delta g_I}{g_I})^2 = (\frac{\delta \Upsilon}{\Upsilon})^2 + (\frac{\delta \mu_B}{\mu_B})^2 + (\frac{\delta B}{B})^2 \tag{A.24}$$

[3] Unfortunately for me, and unbeknownst for several weeks, this technique has actually been outlined decades ago [52]. This technique, however, was never applied to trapped, ultracold atoms and still remains an important experimental study.

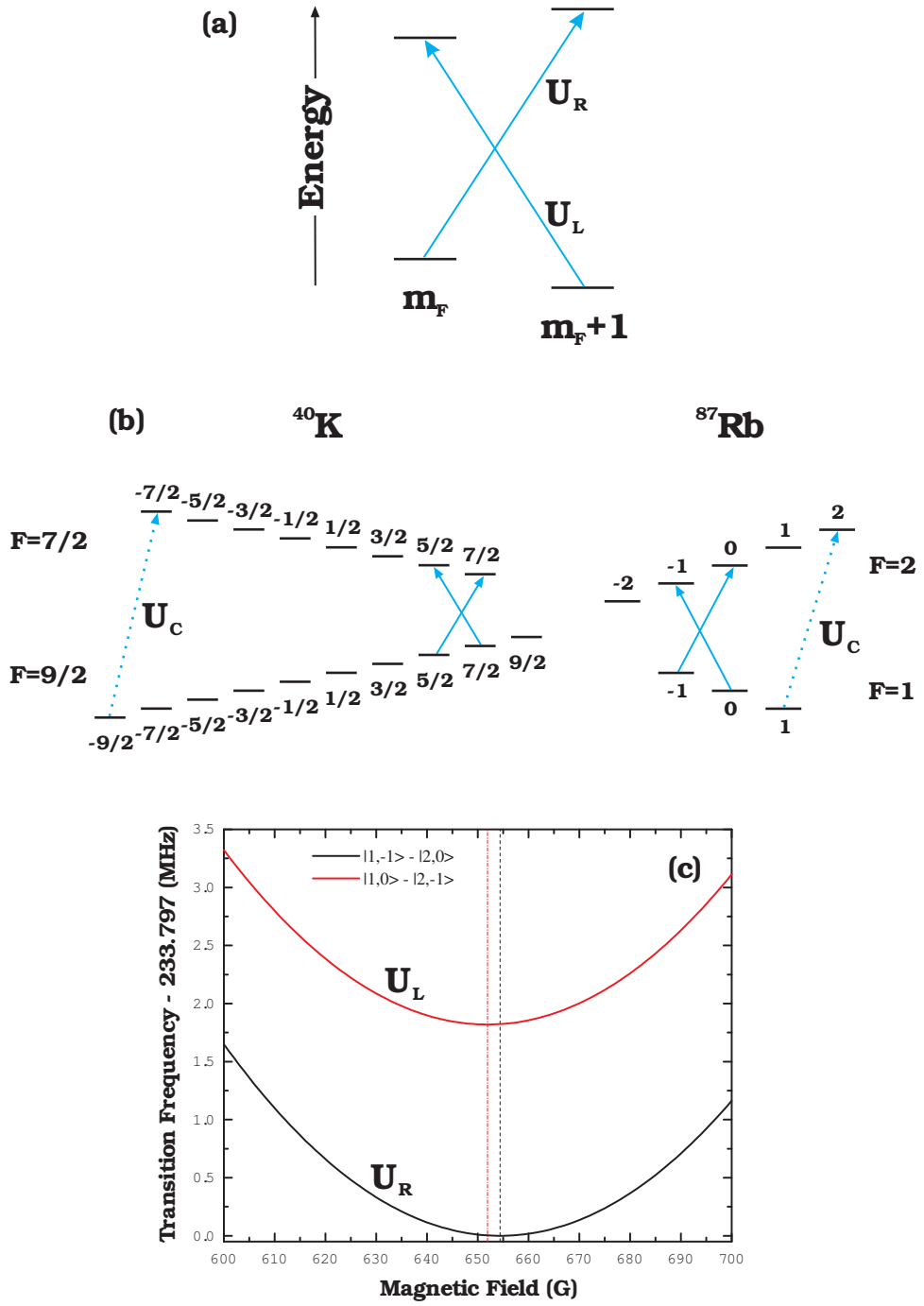

Figure A.9: Left vs. right transition. The illustration shows the rightward U_R and leftward U_L transitions described in the text with two sets of candidate transitions shown in blue. The energy difference between the left and right transitions is directly proportional to the energy cost in flipping the nuclear magnetic moment μ_I. The idea of the experiment is to measure the two transition frequencies as a function of magnetic field near a 'magic-spot' resonance in order to discern the nuclear magnetic moment. The dotted arrow indicates the transition with the largest magnetic-field sensitivity, a transition used to calibrate the magnetic field.

where the fractional uncertainty in the Bohr magneton is $\sim 4 \times 10^{-8}$. One may assume that with proper technique and apparatus one might achieve $<$ 1 Hz resolution of Υ, which may be on the order of a few hundred kHz (see the tables in Sec. A.2.1), giving a fractional uncertainty of $\sim 4 \times 10^{-6}$. It seems the leading source of uncertainty in making this measurement might be the calibration of the magnetic field.

Measurements in the past have measured nuclear magnetic moments very well with atomic beam experiments [53]. However, these experiments relied on spatial uniformity and calibration of magnetic fields over large distances (several tens of centimeters) and were sensitive to interactions with the vacuum chamber walls [54, 55]. The method presented here of measuring nuclear magnetic moments relies on the calibration of the magnetic field in a region of space orders of magnitude smaller and is completely insensitive to interactions with chamber walls. If it would become possible to calibrate a magnetic field of a few hundred gauss to $<$ 10 mG precision ($\delta B/B \sim 2 \times 10^{-5}$), it would be possible to improve measurements of the nuclear magnetic moment of ^{40}K, whose current uncertainty is 2×10^{-4}, by a factor of ten.

The possibility exists to calibrate the magnetic field using alkali atoms to such precise levels that the uncertainty in the field would be largely dominated by servo electronics. This method of calibrating the magnetic field relies on measurements of the transition within the ground-state manifold that is *maximally* sensitive to the magnetic field. This transition, depicted in Fig. A.9(b) as a dotted arrow, would have field sensitivities on the order of the Bohr magneton ($\mu_B \approx$1.4 MHz/G). If it would become possible to measure this calibration frequency ($\nu_c = U_c/h$) to the 1 Hz level as well, one would be able to ascertain the magnetic field to incredibly precise levels (1 Hz/$\mu_B \approx 10^{-6}$G)! At this level, the uncertainty in the field calibration would be dominated by such systematic errors as electronic noise, ambient field drifts, and temperature instabilities, to name a few. With such a precise calibration process in place, it would be possible to make measurements of nuclear magnetic moments that compete with or surpass

measurements that have been done in past atomic-beam experiments [53].

Additionally, these experiments relied on the natural abundance of the various isotopes of each element, which made the measurement with ^{40}K relatively poor due to its low, 0.01% natural abundance. The method presented here offers a way of measuring a pure sample of a specific isotope, free from possible systematics caused by isotopic contamination and interactions with the chamber walls.

In addition to making a more precise measurement of the nuclear magnetic moment of ^{40}K, one would also gain a great deal more insight into the nuclear structure of potassium. Despite the difference between 'bosonic' or 'fermionic' labels, every isotope of a given atomic species should share a common nuclear factor, A_J/g_I, where A_J is the hyperfine splitting constant $A_J = E_{hfs}/(2I+1)$. This nuclear factor is ideally equal between all isotopes with point-like nuclei. We may define a constant, called the hyperfine anomaly constant Δ_{hf}, to be the fractional difference from unity between the nuclear factors of differing isotopes and write it as,

$$\Delta_{hf} = \frac{A_{J,1}}{A_{J,2}} \frac{g_{I,2}}{g_{I,1}} - 1, \tag{A.25}$$

where the (1) and (2) labels are attached to two different isotopes. This hyperfine anomaly is usually <0.007. The nature of this anomaly was first elucidated by A. Bohr and V. Weisskopf [56]. Their theory explains how the anomaly can be attributed to interactions of the electron with a finite-size nucleus. In addition, the magnitude of the anomaly describes the distribution of neutrons within the nucleus [57]. In other words, this table-top experiment would allow one to probe the distribution of neutrons within the nucleus simply by probing an ultracold sample of atoms with microwave radiation! A similar measurement has been made with 5 isotopes of francium [58].

Neither the nuclear magnetic moment, nor the hyperfine splitting of ^{40}K have been measured in over 55 years. The poor measurement of the nuclear magnetic moment, in particular, leads to a large uncertainty of the hyperfine anomalies between ^{39}K -^{40}K, and

^{40}K-^{41}K (current fractional errors in the hyperfine anomaly are $< 5\%$). By increasing the accuracy of such measurements, a significant amount of knowledge of the potassium nucleus might be obtained.

One last selling point that should be mentioned is that the potassium atom is unique to alkali atoms, in that it has three readily available isotopes with which to work (^{39}K,^{40}K, and^{41}K), which give three measurements of hyperfine anomalies. Other alkali atoms, in which a significant amount of work has been done measuring hyperfine constants (like Rb, Cs, Li, Na, and H), have only one or two readily available isotopes with which to work in ultracold systems, which would give one or zero hyperfine anomalies per atom.[4] This makes potassium a very desirable atom with which to work. By increasing the accuracy of the nuclear magnetic moment in ^{40}K, one would have measurements of three hyperfine-anomaly constants with accuracies of $< 0.1\%$.

A.2.1 Determining 'Magic Spots'

The term 'magic spot' refers to the magnetic field at which a transition's magnetic-field sensitivity is exactly zero. In other words, the field at which the first derivative of the transition energy with respect to magnetic field is zero ($\partial_B U(B)|_{B_{ms}}$=0). The detuning of the transition frequency ν from the zero-field hyperfine splitting ν_{hfs} can be written as,

$$\Delta(B) = \nu(B) - \nu_{hfs}, \tag{A.26}$$

This detuning can be approximated as second-order polynomial near the magic spot (B_{ms}) as,

$$\Delta(B) = -\Delta_{ms} + B^{''}(B - B_{ms})^2. \tag{A.27}$$

A table of values of Δ_{ms}, $B^{''}$ and B_{ms} are given below for ^{87}Rb and ^{40}K. These 'magic-spot' magnetic-field values span several thousand Gauss and are extremely well known

[4] Hydrogen has three isotopes, but I'm not sure how readily available tritium is: Dr. Octopus killed people in order to obtain it in Spiderman 2!

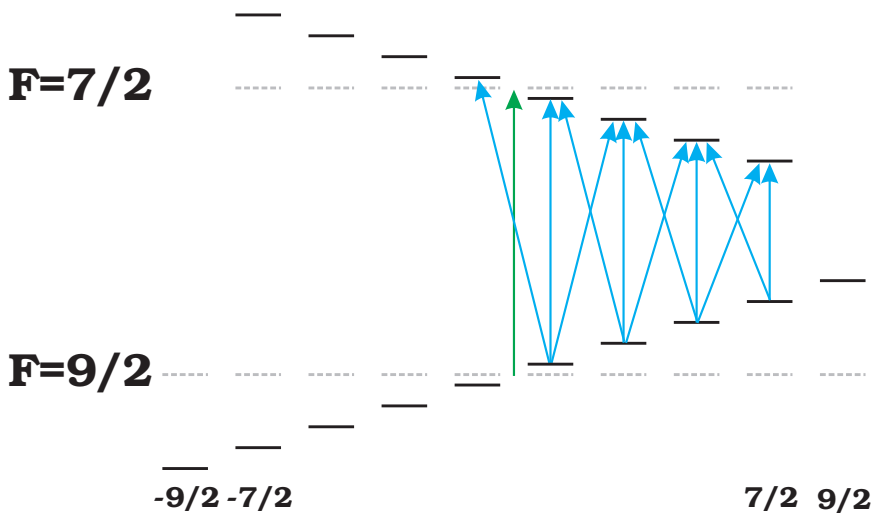

Figure A.10: Single-photon transitions in ^{40}K. The green line represents the zero-field transition E_{hfs}.

quantities.

A.2.2 Issues with the AC Stark Shift

For experiments which trap neutral atoms in optical dipole traps, the ac Stark shift of the energy levels must be taken into account in order to make accurate measurements of the nuclear magnetic moment. The fact that one of the two ground state hyperfine manifolds being studied is closer in energy ($\sim$ GHz) to the excited state transition ($\lambda \sim 800$nm) gives rise to a systematic shift between transition frequencies. This shift comes from the presence of the intense trapping lasers ($\lambda \sim 1000$ nm; maximum intensity $\sim$20 MW/m^2).[5] The intensity of the trapping lasers has the following form:

$$I(x,y,z) = \frac{2P}{\pi w^2(1+(z/z_R)^2)}\ Exp(\frac{-2(x^2+y^2)}{w^2(1+(z/z_R)^2)}), \tag{A.28}$$

where P is the total power in the beam ($\sim$300 mW), w is the $1/e^2$ waist of the beam and z_R is the Rayleigh length of the focused laser. This spatial variation in intensity leads to a slight systematic shift between energy levels. The potential energy experienced

[5] The trapping-laser parameters used for studying the ac Stark shift are taken from groups here at JILA which trap atoms in optical dipole traps.

Transition $\lvert\frac{9}{2}, m_F\rangle \rightarrow \lvert\frac{7}{2}, m_F\rangle$	B_{MS} (G)	$-\Delta_{MS}$ (kHz)	B'' (Hz/G^2)
$1/2 \rightarrow -1/2$	0.04095	0.00506	3015.83
$1/2 \rightarrow 1/2$	50.983	7961.62	3072.56
$1/2 \rightarrow 3/2$	103.269	32553.1	3094.34
$3/2 \rightarrow 1/2$	103.349	32604.2	3094.35
$3/2 \rightarrow 3/2$	152.949	73535.6	3238.76
$3/2 \rightarrow 5/2$	207.095	136146.	3375.83
$5/2 \rightarrow 3/2$	207.168	136248.	3375.85
$5/2 \rightarrow 5/2$	254.916	216682.	3672.41
$5/2 \rightarrow 7/2$	312.955	336264.	4121.19
$7/2 \rightarrow 5/2$	313.015	336418.	4121.28
$7/2 \rightarrow 7/2$	356.882	477620.	4858.14
$-1/2 \rightarrow 3/2$	53.584	8355.83	2921.80
$3/2 \rightarrow -1/2$	53.753	8408.86	2921.83
$1/2 \rightarrow 5/2$	161.938	77956.0	3093.27
$5/2 \rightarrow 1/2$	162.097	78116.0	3093.42
$3/2 \rightarrow 7/2$	275.240	235811.	3606.83
$7/2 \rightarrow 3/2$	275.377	236083.	3607.28

Table A.1: Table of relevant 'magic spots' in ^{40}K. The double line separates single-photon transitions from two-photon transitions.

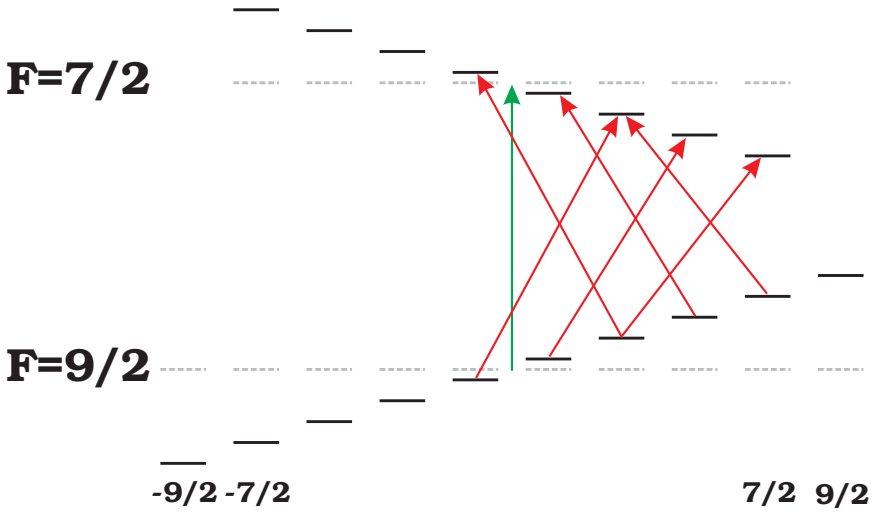

Figure A.11: Two-photon transitions in ^{40}K. The green line represents the zero-field transition E_{hfs}.

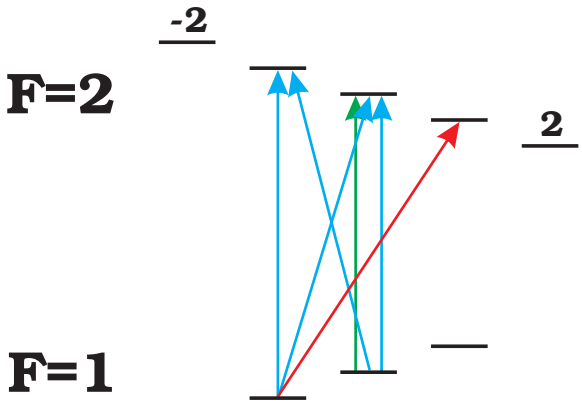

Figure A.12: Magic Spots in ^{87}Rb.

Transition $\lvert 1, m_F\rangle \rightarrow \lvert 2, m_F\rangle$	B_{MS} (G)	$-\Delta_{MS}$ (kHz)	B'' (Hz/G^2)
$0 \rightarrow 0$	0	0	575.146
$0 \rightarrow -1$	651.895	231977.	558.394
$-1 \rightarrow 0$	654.389	233797.	558.460
$-1 \rightarrow -1$	1218.78	915674.	664.122
$-1 \rightarrow 1$	3.22892	4.49731	431.360

Table A.2: Table of relevant 'magic spots' in ^{87}Rb. The double line separates single-photon transitions from two-photon transitions. The green line represents the zero-field transition E_{hfs}.

by a neutral atom in this intense field is proportional to the intensity field and can be written as follows:

$$U_{dip}(x,y,z) = \frac{-3\pi c^2 \Gamma}{2(\omega_o + \Delta)^3}\left(\frac{1}{\omega_o + \Delta - \omega} + \frac{1}{\omega_o + \Delta + \omega}\right) I(x,y,z), \tag{A.29}$$

where Γ is the natural linewidth of the optical transition ω_o, Δ is the hyperfine splitting $E_{hfs}/\hbar$, ω is the frequency of the trapping laser and c is the speed of light. While the total shift of a given hyperfine manifold is on the order of 100 kHz, the differential shift between manifolds is only on the order of 1 Hz. This shift is, however, common to both U_R and U_L and should not contribute greatly to systematic errors.

Appendix B

Detailed Calculations

This appendix shows the details of calculations which are beyond the scope of the above discussions and which require several pages of exciting algebra. In this sense, the following sections provide an archive of the behind-the-scenes work which accompanies the above discussions.

B.1 Resonantly Driven Oscillator Calculations

This section of Appendix B details the algebra and geometry needed to calculate the functional forms of the position of atoms in a resonantly-driven oscillator (Eqs. 4.6 - 4.10).

Fig. 4.4 shows the geometry of the driven oscillator. The red arrow indicates the amplitude of the oscillation $\dot{a}\ t$ due to the application of an external electric field, while the blue arrow indicates the amplitude a_o of the initial dipole oscillation. The resultant vector $a(t)$ can be found geometrically be decomposing $\dot{a}\ t$ into its projection along $\hat{a}_o$ and the ot*h*er axis which completes the basis of the plane (call it what you like).

Its projection along $\hat{a}_o$ is equal to $\dot{a}t\ \cos(\phi_i)$, while its other projection is equal to $\dot{a}t\ \sin(\phi_i)$. By the Pythagorean theorem,

$$a^2(t) = (a_o + \dot{a}t\ \cos(\phi_i))^2 + (\dot{a}t\ \sin(\phi_i))^2, \tag{B.1}$$

and,

$$a(t) = \sqrt{(a_o^2 + (\dot{a}t)^2 + 2a_o\dot{a}t\ \cos(\phi_i)}, \tag{B.2}$$

In order to find the phase $\phi_f(t)$ of the oscillation, we must use the Law of Cosines,

$$\cos(\phi_f(t)) = \frac{a_o^2 + a^2(t) - (\dot{a}t)^2}{2a_o a(t)}. \tag{B.3}$$

From this we recover Eq. 4.10,

$$\phi_f(t) = \cos^{-1}(\frac{a_o + \dot{a}t\ \cos(\phi_i)}{a(t)}). \tag{B.4}$$

The resulting equation for the position of the atoms as a function of time (Eq. 4.7) was verified to be a solution to the differential equation which describes the system,

$$\ddot{x} + \omega_o^2 x = \frac{F_o}{m}\sin(\omega_o t + \phi_i). \tag{B.5}$$

B.2 Frequency Shifts From Electric-Field Contaminants

A single-power law electric field was sometimes inadequate in describing the functional form of small fields near the surface. One can see that the measured field gradient (proportional to the amplitude growth rate in Fig. 4.6(b)) occasionally needed to be described by a double-power law in order to fully describe the nature of the electric field near the surface. A double-power law of the form

$$E_i = C_{i1}(q_i - q_o)^{-p_{i1}} + C_{i2}(q_i - q_{io})^{-p_{i2}} \tag{B.6}$$

was found to best describe the electric field in the i-direction for a small range of atom-surface distances. Here q_i is the spatial coordinate in the i-direction for $i = x, y$, and z.

The contribution of the fractional frequency shift $\Delta\gamma$ arising from this specific electric field can be written as,

$$\Delta\gamma = \Delta\gamma_{11} + \Delta\gamma_{22} + \Delta\gamma_{12} \tag{B.7}$$

where the above has been split into three terms to fit the document.

$$\Delta\gamma_{11} = C_{i1}^2 p_{i1}(2p_{i1} + 1)(q_i - q_{io})^{-2(p_{i1}+1)} \tag{B.8}$$

$$\Delta\gamma_{22} = C_{i2}^2 p_{i2}(2p_{i2}+1)(q_i - q_{io})^{-2(p_{i2}+1)} \tag{B.9}$$

$$\Delta\gamma_{12} = C_{i1}C_{i2}(2p_{i1}p_{i2} + p_{i1}(p_{i1}+1) + p_{i2}(p_{i2}+1))(q_i - q_{io})^{-(p_{i1}+p_{i2}+2)} \tag{B.10}$$

Eq. B.7 is similar to, but more complicated than Eq. 4.17. The key difference between Eq. 4.17 and Eq. B.7 is that the latter may, in fact, become negative (as seen in Fig. 4.9(b)). This is due to the cross term upon the expansion of Eq. B.6 in Eq. 4.1*5*.

Bibliography

[1] H. B. G. Casimir and D. Polder, Phys. Rev. **73**, 360 (1948).

[2] E. M. Lifshitz, Sov. Phys. JETP **3**, 977 (1957).

[3] I. E. Dzyaloshinskii, E. M. Lifshitz, and L. P. Pitaevshii, Adv. Phys. **38**, 165 (1961).

[4] E. M. Lifshitz, Doklady Akademii Nauk SSSR **100**, 879 (1955).

[5] S. K. Lamoreaux, Rep. Prog. Phys. **68**, 201 (2005).

[6] S. K. Lamoreaux, Phys. Rev. Lett. **78**, 5 (1997).

[7] T. Ederth, Phys. Rev. A **62**, 062104 (2000).

[8] J. Chiaverini, S. J. Smullin, A. A. Geraci, D. M. Weld and A. Kapitulnik, Phys. Rev. Lett. **90**, 151101 (2003).

[9] R. S. Decca, D. Lopez, E. Fischbach, G. L. Klimchitskaya, D. E. Krause, V. M. Mostepanenko, Ann. Phys. (N.Y.) **318**, 37 (2005).

[10] D. M. Harber, Ph.D. Thesis

[11] M. Antezza, L. P. Pitaevskii, and S. Stringari, Phys. Rev. Lett. **95**, 113202 (2005).

[12] H. J. Lewandowski, Ph.D. Thesis

[13] H. J. Lewandowski, D. M. Harber, D. L. Whitaker, and E. A. Cornell, Jour. Low Temp. Phys. **132**, 309 (2003).

[14] J. M. Obrecht, R. J. Wild, M. Antezza, L. P. Pitaevskii, S. Stringari and E. A. Cornell, Phys. Rev. Lett. **98**, 063201 (2007).

[15] D. M. Harber, J. M. McGuirk, J. M. Obrecht, and E. A. Cornell, J. Low Temp. Phys. **133**, 229 (2003).

[16] This chapter is adapted from [14].

[17] H. B. G. Casimir, Proc. K. Ned. Akad. Wet. **51**, 793 (1948).

[18] M. Antezza, L. P. Pitaevskii, S. Stringari, and V. B. Svetovoy, Phys. Rev. Lett. **97**, 223203 (2006).

[19] J. M. McGuirk, D. M. Harber, J. M. Obrecht, and E. A. Cornell, Phys. Rev. A **69**, 062905 (2004).

[20] D. M. Harber, J. M. Obrecht, J. M. McGuirk, and E. A. Cornell, Phys. Rev. A **72**, 033610 (2005).

[21] P. H. G. M. van Blokland and J. T. G. Overbeek, J. Chem. Soc. Faraday Trans. I **74**, 2637 (1978).

[22] U. Mohideen and A. Roy, Phys. Rev. Lett. **81**, 4549 (1998).

[23] H. B. Chan, V. A. Aksyuk, R. N. Kleiman, D. J. Bishop, and F. Capasso, Science **291**, 1941 (2001).

[24] G. Bressi, G. Carugno, R. Onofrio, and G. Ruoso, Phys. Rev. Lett. **88**, 041804 (2002).

[25] R. S. Decca, D. Lopez, E. Fischbach, and D. E. Krause, Phys. Rev. Lett. **91**, 050402 (2003).

[26] C. I. Sukenik, M. G. Boshier, D. Cho, V. Sandoghdar, and E. A. Hinds, Phys. Rev. Lett. **70**, 560 (1993).

[27] A. Landragin, J. Y. Courtois, G. Labeyrie, N. Vansteenkiste, C. I. Westbrook, and A. Aspect, Phys. Rev. Lett. **77**, 1464 (1996).

[28] F. Shimizu, Phys. Rev. Lett. **86**, 987 (2001).

[29] V. Druzhinina and M. DeKieviet, Phys. Rev. Lett. **91**, 193202 (2003).

[30] Y. J. Lin, I. Teper, C. Chin, and V. Vuletic, Phys. Rev. Lett. **92**, 050404 (2004).

[31] T. A. Pasquini, Y. Shin, C. Sanner, M. Saba, A. Schirotzek, D. E. Pritchard, and W. Ketterle, Phys. Rev. Lett. **93**, 223201 (2004).

[32] H. Oberst, Y. Tashiro, K. Shimizu, and F. Shimizu, Phys. Rev. A **71**, 052901 (2005).

[33] C. Henkel, K. Joulain, J.-P. Mulet, and J.-J. Greffet, J. Opt. A: Pure Appl. Opt. **4**, S109 (2002).

[34] H. R. Phillip, *Handbook of Optical Constants of Solids*, 749 (1985).

[35] M. Antezza, L. P. Pitaevskii, and S. Stringari, Phys. Rev. A **70**, 053619 (2004).

[36] J. M. Obrecht, R. J. Wild, and E. A. Cornell, to be published.

[37] This chapter is adapted from [36].

[38] M. J. Snadden, J. M. McGuirk, P. Bouyer, K. G. Haritos, and M. A. Kasevich, Phys. Rev. Lett. **81**, 971 (1998).

[39] G. Roati, E. de Mirandes, F. Ferlaino, H. Ott, G. Modugno, and M. Inguscio, Phys. Rev. Lett. **92**, 230402 (2004).

[40] G. Ferrari, N. Poli, F. Sorrentino, and G. M. Tino, Phys. Rev. Lett. **97**, 060402 (2006).

[41] A. Bertoldi, G. Lamporesi, L. Cacciapuoti, M. de Angelis, M. Fattori, T. Petelski, A. Peters, M. Prevedelli, J. Stuhler, and G. M. Tino, Eur. Phys. Jour. D **40**, 271 (2006).

[42] J. B. Fixler, G. T. Foster, J. M. McGuirk and M. A. Kasevich, Science **315**, 74 (2007).

[43] M. P. A. Jones, C. J. Vale, D. Sahagun, B. V. Hall, and E. A. Hinds, Phys. Rev. Lett. **91**, 080401 (2003).

[44] J. D. Perreault, and A. D. Cronin, Phys. Rev. Lett. **95**, 133201 (2005).

[45] S. Wildermuth, S. Hofferberth, I. Lesanovsky, S. Groth, P. Kruger, J. Schmiedmayer, and I. Bar-Joseph, Appl. Phys. Lett. **88**, 264103 (2006).

[46] V. V. Nesvizhevsky, H. G. Börner, A. K. Petukhov, H. Abele, S. Baeßler, F. J. Rueß, T. Stöferle, A. Westphal, A. M. Gagarski, G. A. Petrov, and A. V. Strelkov, Nature **415**, 297 (2002).

[47] F. Shimizu, Phys. Rev. Lett. **86**, 987 (2001).

[48] T. A. Pasquini, Y. Shin, C. Sanner, M. Saba, A. Schirotzek, D. E. Pritchard, and W. Ketterle, Phys. Rev. Lett. **93**, 223201 (2004).

[49] H. Oberst, Y. Tashiro, K. Shimizu, and F. Shimizu, Phys. Rev. A **71**, 052901 (2005).

[50] T. A. Pasquini, M. Saba, G.-B. Jo, Y. Shin, W. Ketterle, D. E. Pritchard, T. A. Savas, and N. Mulders, Phys. Rev. Lett. **97**, 093201 (2006).

[51] D. M. Harber, H. J. Lewandowski, J. M. McGuirk, and E. A. Cornell, Phys. Rev. A **66**, 053616 (2002).

[52] J. T. Eisinger, B. Bederson and B. T. Feld, Phys. Rev. **86**, 73 (1952).

[53] See E. Arimondo, M. Inguscio and P. Violino, Rev. Mod. Phys. **49**, 31 (1977) and references therein.

[54] H. M. Goldenberg, D. Kleppner, and N. F. Ramsey, Phys. Rev. **123**, 530 (1961).

[55] P. W. Zitzewitz, and N. F. Ramsey, Phys. Rev. A **3**, 51 (1971).

[56] A. Bohr, and V. F. Weisskopf, Phys. Rev. **77**, 94 (1950).

[57] A. Bohr, Phys. Rev. **81**, 134 (1951) and A. Bohr, Phys. Rev. **81**, 331 (1951).

[58] J. S. Grossman, L. A. Orozco, M. R. Pearson, J. E. Simsarian, G. D. Sprouse, and W. Z. Zhao, Phys. Rev. Lett. **83**, 935 (1999).

[59] *The End.*